

# Lie Methods for Nonlinear Dynamics with Applications to Accelerator Physics

---

Alex J. Dragt

*University of Maryland, College Park*

<http://www.physics.umd.edu/dsat/>



1 November 2024

Alex J. Dragt  
Dynamical Systems and Accelerator Theory Group  
Department of Physics  
University of Maryland  
College Park, Maryland 20742

<http://www.physics.umd.edu/dsat>

Work supported in part by U.S. Department of Energy Grant DE-FG02-96ER40949.

---

---

© 1991, 2014, 2018, and 2022 by Alex J. Dragt.

All rights reserved.

# Contents

<i>Preface</i>	lxvii
<b>1 Introductory Concepts</b>	<b>1</b>
1.1 Transfer Maps . . . . .	1
1.1.1 Maps and Dynamics . . . . .	2
1.1.2 Maps and Accelerator Physics . . . . .	8
1.1.3 Maps and Geometry . . . . .	10
1.2 Map Iteration and Other Background Material . . . . .	12
1.2.1 Logistic Map . . . . .	12
1.2.2 Complex Logistic Map and the Mandelbrot Set . . . . .	20
1.2.3 Simplest Nonlinear Symplectic Map . . . . .	26
1.2.4 Goal for Use of Maps in Accelerator Physics . . . . .	29
1.2.5 Some Highlights of the $N$ -Body Gravitational Problem . . . . .	32
1.2.6 Maps from Hamiltonian Differential Equations . . . . .	39
1.3 Essential Theorems for Differential Equations . . . . .	54
1.4 Transfer Maps Produced by Differential Equations . . . . .	60
1.4.1 Map for Simple Harmonic Oscillator . . . . .	61
1.4.2 Maps for Monomial Hamiltonians . . . . .	62
1.4.3 Stroboscopic Maps and Duffing Equation Example . . . . .	63
1.5 Lagrangian and Hamiltonian Equations . . . . .	70
1.5.1 The Nonsingular Case . . . . .	71
1.5.2 A Common Singular Case . . . . .	73
1.6 Hamilton's Equations with a Coordinate as an Independent Variable . . . . .	88
1.7 Manifestly Lorentz Invariant Formulation of Equations of Motion . . . . .	95
1.7.1 Relativistic Preliminaries . . . . .	96
1.7.2 A Relativistic Lagrangian $L_R$ and Associated Relativistic Hamiltonian $H_R$ . . . . .	101
1.7.3 Relation between $L_R$ and $H_R$ and $L$ and $H$ . . . . .	108
1.7.4 An Alternate Relativistic Lagrangian $L_A$ ? . . . . .	110
1.8 Something About Riemannian Manifolds . . . . .	117
1.8.1 Geodesics and Affine Geodesics . . . . .	117
1.8.2 Affine Geodesics in Minkowski Space . . . . .	123
1.8.3 Relation Between Infinitesimal Interval $ds^2$ and Net Interval $I$ . . . . .	125
1.8.4 Proof that Lorentz Transformations Must Be Linear . . . . .	133
1.8.5 Vector and Tensor Transformation Properties . . . . .	135

1.9	Definition of Poisson Bracket . . . . .	140
<b>2</b>	<b>Numerical Integration</b>	<b>167</b>
2.1	The General Problem . . . . .	168
2.1.1	Integrating Forward in Time . . . . .	168
2.1.2	Integrating Backwards in Time . . . . .	168
2.2	A Crude Solution Due to Euler . . . . .	169
2.2.1	Procedure . . . . .	169
2.2.2	Numerical Example . . . . .	169
2.3	Runge-Kutta Methods . . . . .	176
2.3.1	Introduction . . . . .	176
2.3.2	Procedure . . . . .	177
2.3.3	Numerical Example . . . . .	178
2.3.4	Nomenclature . . . . .	183
2.4	Finite-Difference/Multistep/Multivalued Methods . . . . .	197
2.4.1	Background . . . . .	197
2.4.2	Adams' Method . . . . .	203
2.4.3	Numerical Example . . . . .	205
2.4.4	Derivation and Error Analysis . . . . .	210
2.5	(Automatic) Choice and Change of Step Size and Order . . . . .	226
2.5.1	Adaptive Change of Step Size in Runge-Kutta . . . . .	226
2.5.2	Adaptive Finite-Difference Methods . . . . .	227
2.5.3	Jet Formulation . . . . .	228
2.5.4	Virtues of Jet Formulation . . . . .	234
2.5.5	Advice to the Novice . . . . .	236
2.6	Extrapolation Methods . . . . .	239
2.6.1	Overview . . . . .	239
2.6.2	Making a Meso Step . . . . .	239
2.6.3	Summary . . . . .	243
2.6.4	Again, Advice to the Novice . . . . .	243
2.7	Things Not Covered . . . . .	246
2.7.1	Størmer-Cowell and Nyström Methods . . . . .	247
2.7.2	Other Starting Procedures . . . . .	247
2.7.3	Stability . . . . .	247
2.7.4	Regularization, Etc. . . . .	247
2.7.5	Solutions with Few Derivatives . . . . .	248
2.7.6	Symplectic and Geometric/Structure-Preserving Integrators . . . . .	248
2.7.7	Error Analysis . . . . .	249
2.7.8	Backward Error Analysis . . . . .	250
2.7.9	Comparison of Methods . . . . .	251
<b>3</b>	<b>Symplectic Matrices and Lie Algebras/Groups</b>	<b>259</b>
3.1	Definitions . . . . .	260
3.2	Variants . . . . .	263
3.3	Simple Symplectic Restrictions and Symplectic Factorization . . . . .	266

3.3.1	Large-Block Formulation . . . . .	266
3.3.2	Symplectic Block Factorization . . . . .	267
3.3.3	Symplectic Matrices Have Determinant +1 . . . . .	270
3.3.4	Small-Block Formulation . . . . .	270
3.4	Eigenvalue Spectrum . . . . .	277
3.4.1	Background . . . . .	278
3.4.2	The $2 \times 2$ Case . . . . .	279
3.4.3	The $4 \times 4$ and Remaining $2n \times 2n$ Cases . . . . .	280
3.4.4	Further Symplectic Restrictions . . . . .	284
3.4.5	In Praise of and Gratitude for the Symplectic Condition . . . . .	286
3.5	Eigenvector Structure, Normal Forms, and Stability . . . . .	291
3.5.1	Eigenvector Basis . . . . .	291
3.5.2	$J$ -Based Angular Inner Product . . . . .	291
3.5.3	Use of Angular Inner Product . . . . .	291
3.5.4	Definition and Use of Signature . . . . .	293
3.5.5	Definition of Phase Advances and Tunes . . . . .	295
3.5.6	The Krein-Moser Theorem and Krein Collisions . . . . .	295
3.5.7	Normal Forms . . . . .	297
3.5.8	Stability . . . . .	299
3.6	Group Properties, Dyadic and Gram Matrices, and Bases . . . . .	304
3.6.1	Group Properties . . . . .	305
3.6.2	Dyadic and Gram Matrices, Bases and Reciprocal Bases . . . . .	307
3.6.3	Orthonormal and Symplectic Bases . . . . .	310
3.6.4	Construction of Orthonormal Bases . . . . .	313
3.6.5	Construction of Symplectic Bases . . . . .	319
3.7	Lie Algebraic Properties . . . . .	333
3.7.1	Matrix Exponential and Logarithm . . . . .	333
3.7.2	Application to Symplectic Matrices . . . . .	336
3.7.3	Matrix Lie Algebra and Lie Group: The Baker-Campbell-Hausdorff (BCH) Multiplication Theorem . . . . .	338
3.7.4	Abstract Definition of a Lie Algebra . . . . .	341
3.7.5	Abstract Definition of a Lie Group . . . . .	342
3.7.6	Classification of Lie Algebras . . . . .	343
3.7.7	Adjoint Representation of a Lie Algebra . . . . .	348
3.8	Exponential Representations of Group Elements . . . . .	379
3.8.1	Exponential Representation of Orthogonal and Unitary Matrices . . . . .	380
3.8.2	Exponential Representation of Symplectic Matrices . . . . .	380
3.9	Unitary Subgroup Structure . . . . .	392
3.10	Other Subgroup Structure . . . . .	403
3.11	Other Factorizations/Decompositions . . . . .	406
3.12	Cayley Representation of Symplectic Matrices . . . . .	407
3.13	General Symplectic Forms, Darboux Transformations, <i>Etc.</i> . . . .	415
3.13.1	General Symplectic Forms . . . . .	415
3.13.2	Darboux Transformations . . . . .	419
3.13.3	Symplectic Forms and Pfaffians . . . . .	422

3.13.4	Variant Symplectic Groups?	423
<b>4</b>	<b>Matrix Exponentiation, Polar Decompositions, and Symplectifications</b>	<b>437</b>
4.1	Exponentiation by Scaling and Squaring	439
4.1.1	The Ordinary Exponential Function	439
4.1.2	The Matrix Exponential Function	444
4.2	(Orthogonal and Unitary) Polar Decompositions	447
4.2.1	Real Matrix Case	447
4.2.2	Application to the Symplectic Group	448
4.2.3	Complex Matrix Case	449
4.3	Matrix Symplectification	454
4.3.1	Properties of $J$ -Symmetric Matrices	456
4.3.2	Initial Result on Symplectic Polar Decomposition	460
4.3.3	Extended Result on Symplectic Polar Decomposition	464
4.3.4	Symplectic Polar Decomposition Not Globally Possible	467
4.3.5	Uniqueness of Symplectic Polar Decomposition	470
4.3.6	Concluding Summary	472
4.4	Finding the Closest Symplectic Matrix	486
4.4.1	Background	486
4.4.2	Use of Euclidean Norm	488
4.4.3	Geometric Interpretation of Symplectic Polar Decomposition	490
4.5	Symplectification Using Symplectic Polar Decomposition	497
4.5.1	Properties of Symplectification Using Symplectic Polar Decomposition	498
4.5.2	Iteration	499
4.6	Modified Darboux Symplectification	517
4.7	Exponential and Cayley Symplectifications	520
4.7.1	Exponential Symplectification	520
4.7.2	Cayley Symplectification	520
4.7.3	Cayley Symplectification Near the Identity	522
4.8	Generating Function Symplectification	523
<b>5</b>	<b>Preliminary Lie Concepts for Classical Mechanics and Related Delights</b>	<b>529</b>
5.1	Properties of the Poisson Bracket	529
5.2	Equations, Constants, and Integrals of Motion	531
5.3	Lie Operators	533
5.4	Lie Transformations	538
5.4.1	Definition and Some Properties	538
5.4.2	Applications	541
5.5	Realization of the $sp(2n, \mathbb{R})$ Lie Algebra	543
5.6	Basis for $sp(2, \mathbb{R})$	546
5.7	Basis for $sp(4, \mathbb{R})$	551
5.8	Basis for $sp(6, \mathbb{R})$	558
5.8.1	$U(3)$ Preliminaries	558
5.8.2	Polynomials for $u(3)$	559

5.8.3	Plan for the Remaining Polynomials . . . . .	560
5.8.4	Cartan Basis for $su(3)$ . . . . .	560
5.8.5	Representations of $su(3)$ : Cartan's Approach . . . . .	563
5.8.6	Weight Diagrams for the First Few $su(3)$ Representations . . . . .	565
5.8.7	Weight Diagram for the General $su(3)$ Representation . . . . .	569
5.8.8	The Clebsch-Gordan Series for $su(3)$ . . . . .	571
5.8.9	Representations of $su(3)$ : the Approach of Schur and Weyl . . . . .	572
5.8.10	Remaining Polynomials . . . . .	573
5.9	Some Topological Questions . . . . .	587
5.9.1	Nature and Connectivity of $Sp(2n, \mathbb{R})$ . . . . .	587
5.9.2	Where Are the Stable Elements? . . . . .	591
5.9.3	Covering/Circumnavigating $U(n)$ . . . . .	593
5.10	Notational Pitfalls and Quaternions . . . . .	596
5.10.1	The Lie Algebras $sp(2n, \mathbb{R})$ and $usp(2n)$ . . . . .	596
5.10.2	$USp(2n)$ and the Quaternion Field . . . . .	597
5.10.3	Quaternion Matrices . . . . .	598
5.10.4	Properties of Quaternion Matrices . . . . .	599
5.10.5	Quaternion Matrices and $USp(2n)$ . . . . .	601
5.10.6	Quaternion Inner Product and Its Preservation . . . . .	602
5.10.7	Discussion . . . . .	603
5.11	Möbius Transformations . . . . .	608
5.11.1	Definition in the Context of Complex Variables . . . . .	608
5.11.2	Matrix Extension . . . . .	609
5.11.3	Invertibility Conditions . . . . .	610
5.11.4	Transitivity . . . . .	613
5.12	Symplectic Transformations and Siegel Space . . . . .	615
5.12.1	Action of $Sp(2n, \mathbb{C})$ on the Space of Complex Symmetric Matrices . . . . .	615
5.12.2	Siegel Space and $Sp(2n, \mathbb{R})$ . . . . .	616
5.12.3	Group Actions on Homogeneous Spaces . . . . .	616
5.12.4	Homogeneous Spaces and Cosets . . . . .	618
5.12.5	Group Action on Cosets Equals Group Action on a Homogeneous Space . . . . .	619
5.12.6	Application of Results to Action of $Sp(2n, \mathbb{R})$ on Siegel Space . . . . .	620
5.12.7	Action of $Sp(2n, \mathbb{R})$ on the Generalized Real Axis . . . . .	622
5.12.8	Symplectic Modular Groups . . . . .	623
5.13	Möbius Transformations Relating Symplectic and Symmetric Matrices . . . . .	628
5.13.1	Overview . . . . .	628
5.13.2	The Cayley Möbius Transformation . . . . .	628
5.13.3	Two Symplectic Forms and Their Relation by a Darboux Transformation . . . . .	630
5.13.4	The Infinite Family of Darboux Transformations . . . . .	630
5.13.5	Isotropic Vectors and Lagrangian Planes . . . . .	632
5.13.6	Connection between Symplectic Matrices and Lagrangian Planes for the Symplectic Form $\tilde{J}^{4n}$ . . . . .	634

5.13.7	Connection between Symmetric Matrices and Lagrangian Planes for the Symplectic Form $J^{4n}$ . . . . .	635
5.13.8	Relation between Symplectic and Symmetric Matrices and the Role of Darboux Möbius Transformations . . . . .	637
5.13.9	Completion of Tasks . . . . .	640
5.14	Uniqueness of Cayley Möbius Transformation . . . . .	648
5.15	Matrix Symplectification Revisited . . . . .	653
<b>6</b>	<b>Symplectic Maps</b>	<b>663</b>
6.1	Preliminaries and Definitions . . . . .	663
6.1.1	Gradient Maps . . . . .	664
6.1.2	Symplectic Maps . . . . .	665
6.2	Group Properties . . . . .	670
6.2.1	The General Case . . . . .	670
6.2.2	Various Subgroups and Their Names . . . . .	671
6.3	Preservation of General Poisson Brackets . . . . .	684
6.4	Relation to Hamiltonian Flows . . . . .	687
6.4.1	Hamiltonian Flows Generate Symplectic Maps . . . . .	687
6.4.2	Any Family of Symplectic Maps Is Hamiltonian Generated . . . . .	690
6.4.3	Almost All Symplectic Maps Are Hamiltonian Generated . . . . .	694
6.4.4	Transformation of a Hamiltonian Under the Action of a Symplectic Map . . . . .	694
6.5	Mixed-Variable Generating Functions . . . . .	703
6.5.1	Generating Functions Produce Symplectic Maps . . . . .	704
6.5.2	Finding a Generating Function from a Map or a Generating Hamiltonian . . . . .	712
6.5.3	Finding the Generating Hamiltonian from a Generating Function; Hamilton-Jacobi Theory/Equations . . . . .	717
6.6	Generating Functions Come from an Exact Differential . . . . .	731
6.6.1	Overview . . . . .	731
6.6.2	A Democratic Differential Form . . . . .	732
6.6.3	Information about $\mathcal{M}$ Carried by the Democratic Form . . . . .	734
6.6.4	Breaking the Degeneracy . . . . .	736
6.7	Plethora of Generating Functions . . . . .	741
6.7.1	Derivation . . . . .	741
6.7.2	Discussion . . . . .	748
6.7.3	Relating Source Functions and Generating Hamiltonians, Transformation of Hamiltonians, and Hamilton-Jacobi Theory/Equations . . . . .	753
6.7.4	What Kind of Generating Function/Darboux Matrix Should We Choose? . . . . .	761
6.8	Symplectic Invariants . . . . .	788
6.8.1	Liouville's Theorem . . . . .	788
6.8.2	Gromov's Nonsqueezing Theorem and the Symplectic Camel . . . . .	790
6.8.3	Poincaré Integral Invariants . . . . .	795
6.8.4	Connection between Surface and Line Integrals . . . . .	797



6.8.5	Poincaré-Cartan Integral Invariant . . . . .	801
6.9	Poincaré Surface of Section and Poincaré Return Maps . . . . .	807
6.9.1	Poincaré Surface of Section Maps . . . . .	808
6.9.2	Poincaré Return Maps . . . . .	810
6.10	Overview and Preview . . . . .	811
<b>7</b>	<b>Lie Transformations and Symplectic Maps</b>	<b>819</b>
7.1	Production of Symplectic Maps . . . . .	819
7.2	Realization of the Group $Sp(2n)$ and Its Subgroups . . . . .	823
7.2.1	Realization of General Group Element . . . . .	823
7.2.2	Realization of Various Subgroups . . . . .	824
7.2.3	Another Proof of Transitive Action of $Sp(2n)$ on Phase Space . . . . .	827
7.3	Invariant Scalar Product . . . . .	832
7.3.1	Definition of Scalar Product . . . . .	832
7.3.2	Definition of Hermitian Conjugate . . . . .	833
7.3.3	Matrices Associated with Quadratic Lie Generators . . . . .	836
7.4	Symplectic Map for Flow of Time-Independent Hamiltonian . . . . .	844
7.5	Taylor Maps and Jets . . . . .	847
7.6	Factorization Theorem . . . . .	849
7.7	Inclusion of Translations . . . . .	858
7.8	Other Factorizations . . . . .	863
7.9	Coordinates and Connectivity . . . . .	864
7.10	Storage Requirements . . . . .	866
<b>8</b>	<b>A Calculus for Lie Transformations and Noncommuting Operators</b>	<b>873</b>
8.1	Adjoint Lie Operators and the Adjoint Lie Algebra . . . . .	873
8.2	Formulas Involving Adjoint Lie Operators . . . . .	875
8.3	Questions of Order and other Miscellaneous Mysteries . . . . .	879
8.3.1	Questions of Order and Map Multiplication . . . . .	879
8.3.2	Questions of Order in the Linear Case . . . . .	883
8.3.3	Application to General Operators and General Monomials to Construct Matrix Representations . . . . .	884
8.3.4	Application to Linear Transformations of Phase Space . . . . .	886
8.3.5	Dual role of the Phase-Space Coordinates $z_a$ . . . . .	886
8.3.6	Extensions . . . . .	887
8.3.7	Sign Differences . . . . .	888
8.4	Lie Concatenation Formulas . . . . .	891
8.5	Map Inversion and Reverse Factorization . . . . .	899
8.6	Taylor and Hybrid Taylor-Lie Concatenation and Inversion . . . . .	900
8.7	Working with Exponents . . . . .	909
8.7.1	Formulas for Combining Exponents . . . . .	909
8.7.2	Nature of Single Exponential Form . . . . .	912
8.8	Zassenhaus or Factorization Formulas . . . . .	916
8.9	Ideals, Quotients, and Gradings . . . . .	918

<b>9</b>	<b>Inclusion of Translations in the Calculus</b>	<b>943</b>
9.1	Introduction . . . . .	943
9.2	The Inhomogeneous Symplectic Group $ISp(2n, \mathbb{R})$ . . . . .	944
9.2.1	Rearrangement Formula . . . . .	944
9.2.2	Factorization Formula . . . . .	945
9.2.3	Concatenation Formulas . . . . .	948
9.3	Lie Concatenation in the General Nonlinear Case . . . . .	953
9.4	Canonical Treatment of Translations . . . . .	962
9.4.1	Preliminaries . . . . .	962
9.4.2	Case of Maps with No Nonlinear Part . . . . .	967
9.4.3	Case of General Maps . . . . .	971
9.5	Map Inversion and Reverse and Mixed Factorizations . . . . .	982
9.6	Taylor and Hybrid Taylor-Lie Concatenation and Inversion . . . . .	985
9.7	The Lie Algebra of the Group of all Symplectic Maps Is Simple . . . . .	990
<b>10</b>	<b>Computation of Transfer Maps</b>	<b>993</b>
10.1	Equation of Motion . . . . .	993
10.1.1	Background and Derivation . . . . .	993
10.1.2	Perturbation/Splitting Theory and Reverse Factorization . . . . .	994
10.1.3	Perturbation/Splitting Theory and Forward Factorization . . . . .	995
10.2	Series (Dyson) Solution . . . . .	995
10.3	Exponential (Magnus) Solution . . . . .	998
10.4	Factored Product Solution: Powers of $H$ Expansion . . . . .	1001
10.5	Factored Product Solution: Taylor Expansion about Design Orbit . . . . .	1005
10.5.1	Background . . . . .	1005
10.5.2	Term by Term Procedure . . . . .	1008
10.5.3	Summary and GENMAP Nomenclature . . . . .	1014
10.6	Forward Factorization and Lie Concatenation Revisited . . . . .	1015
10.6.1	Preliminary Discussion . . . . .	1015
10.6.2	Forward Factorization . . . . .	1015
10.6.3	Alternate Derivation of Lie Concatenation Formulas . . . . .	1017
10.7	Direct Taylor Summation . . . . .	1019
10.8	Scaling, Splitting, and Squaring . . . . .	1025
10.9	Canonical Treatment of Errors . . . . .	1034
10.10	Wei-Norman and Fer Methods . . . . .	1039
10.10.1	Wei-Norman Equations . . . . .	1039
10.10.2	Accelerated Procedure: The Fer Expansion . . . . .	1039
10.11	Symplectic Integration . . . . .	1039
10.12	Taylor Methods and the Complete Variational Equations . . . . .	1039
10.12.1	Case of No or Ignored Parameter Dependence . . . . .	1041
10.12.2	Inclusion of Parameter Dependence . . . . .	1042
10.12.3	Solution of Complete Variational Equations Using Forward Integration . . . . .	1044
10.12.4	Application of Forward Integration to the Two-Variable Case . . . . .	1045

10.12.5	Solution of Complete Variational Equations Using Backward Integration . . . . .	1049
10.12.6	The Two-Variable Case Revisited . . . . .	1051
10.12.7	Application to Duffing's Equation . . . . .	1051
10.12.8	Application to Duffing's Equation Including some Parameter Dependence . . . . .	1054
10.12.9	Taylor Methods for the Hamiltonian Case . . . . .	1060
<b>11</b>	<b>Geometric/Structure-Preserving Integration: Integration on Manifolds</b>	<b>1067</b>
11.1	Numerical Integration on Manifolds: Rigid-Body Motion . . . . .	1068
11.1.1	Angular Velocity and Rigid-Body Kinematics . . . . .	1068
11.1.2	Angular Velocity and Rigid-Body Dynamics . . . . .	1070
11.1.3	Problem of Integrating the Combined Kinematic and Dynamic Equations . . . . .	1070
11.1.4	Solution by Projection . . . . .	1071
11.1.5	Solution by Parameterization: Euler Angles . . . . .	1071
11.1.6	Problem of Kinematic Singularities . . . . .	1072
11.1.7	Quaternions to the Rescue . . . . .	1073
11.1.8	Modification of the Quaternion Kinematic Equations of Motion . . . . .	1074
11.1.9	Local Coordinate Patches . . . . .	1075
11.1.10	Canonical Coordinates of the Second Kind: Tait-Bryan Angles . . . . .	1076
11.1.11	Canonical Coordinates of the First Kind: Angle-Axis Parameters . . . . .	1076
11.1.12	Cayley Parameters . . . . .	1077
11.1.13	Summary of Integration Using Local Coordinates . . . . .	1078
11.1.14	Integration in the Lie Algebra: Exponential Representation . . . . .	1079
11.1.15	Integration in the Lie Algebra: Cayley Representation . . . . .	1081
11.1.16	Parameterization of $G$ and $\mathcal{L}(G)$ . . . . .	1083
11.1.17	Quaternions Revisited . . . . .	1083
11.2	Numerical Integration on Manifolds: Spin and Qubits . . . . .	1113
11.2.1	Constrained Cartesian Coordinates Are Not Global . . . . .	1114
11.2.2	Polar-Angle Coordinates Are Not Global . . . . .	1114
11.2.3	Local Tangent-Space Coordinates . . . . .	1115
11.2.4	Exploiting Connection with Rigid-Body Kinematics . . . . .	1117
11.2.5	What Just Happened? Generalizations . . . . .	1118
11.2.6	Exploiting an Important Simplification: Lie Taylor Factorization and Lie Taylor Runge Kutta . . . . .	1119
11.2.7	Factored Lie Runge Kutta . . . . .	1125
11.2.8	Magnus Lie Runge Kutta . . . . .	1132
11.2.9	Integration in the Lie Algebra Revisited . . . . .	1138
11.3	Numerical Integration on Manifolds: Charged Particle Motion in a Static Magnetic Field . . . . .	1162
11.3.1	Exploitation of Previous Results . . . . .	1162
11.3.2	Splitting: Exploitation of Future Results . . . . .	1164

<b>12 Geometric/Structure-Preserving Integration: Symplectic Integration</b>	<b>1169</b>
12.1 Splitting, $T + V$ Splitting, and Zassenhaus Formulas . . . . .	1170
12.2 Explicit Symplectic Integrator for Polynomial Hamiltonians . . . . .	1177
12.3 Symplectic Runge-Kutta Methods for $T + V$ Split Hamiltonians: Parti- tioned Runge Kutta and Nyström Runge Kutta . . . . .	1177
12.3.1 Partioned Runge-Kutta . . . . .	1177
12.3.2 Nyström Runge-Kutta . . . . .	1177
12.4 Symplectic Runge-Kutta Methods for General Hamiltonians . . . . .	1177
12.4.1 Background . . . . .	1177
12.4.2 Condition for Symplecticity . . . . .	1179
12.4.3 The Single-Stage Case . . . . .	1179
12.4.4 Two-, Three-, and More-Stage Methods . . . . .	1182
12.5 Study of Single-Stage Method . . . . .	1183
12.6 Study of Two-Stage Method . . . . .	1189
12.7 Numerical Examples for One- and Two-Stage Methods . . . . .	1191
12.8 How Much Iteration Is Required for Implicit Methods? . . . . .	1191
12.9 Proof of Condition for Runge-Kutta to be Symplectic . . . . .	1192
12.10 Symplectic Integration of General Hamiltonians Using Generating Functions	1193
12.11 Explicit Symplectic Integrator for Motion in General Electromagnetic Fields	1193
12.12 Zassenhaus Formulas and Map Computation . . . . .	1199
12.12.1 Case of $T + V$ or General Electromagnetic Field Hamiltonians . .	1199
12.12.2 Case of Hamiltonians Expanded in Homogeneous Polynomials . .	1200
12.13 Other Zassenhaus Formulas and Their Use . . . . .	1205
<b>13 Transfer Maps for Idealized Straight Beam-Line Elements</b>	<b>1217</b>
13.1 Background . . . . .	1217
13.1.1 Specification of Design Orbit . . . . .	1217
13.1.2 Deviation Variables . . . . .	1218
13.1.3 Deviation Variable Hamiltonian . . . . .	1219
13.1.4 Dimensionless Scaled Deviation Variables . . . . .	1220
13.1.5 Scaled Deviation-Variable Hamiltonian . . . . .	1220
13.2 Axial Rotation . . . . .	1223
13.3 Drift . . . . .	1223
13.4 Solenoid . . . . .	1223
13.5 Wiggler/Undulator . . . . .	1223
13.6 Quadrupole . . . . .	1223
13.7 Sextupole . . . . .	1223
13.8 Octupole . . . . .	1223
13.9 Higher-Order Multipoles . . . . .	1223
13.10 Thin Lens Multipoles . . . . .	1223
13.11 Combined Function Quadrupole . . . . .	1223
13.12 Radio Frequency Cavity . . . . .	1223

<b>14</b>	<b>Transfer Maps for Idealized Curved Beam-Line Elements</b>	<b>1227</b>
14.1	Background . . . . .	1227
14.2	Sector Bend . . . . .	1227
14.3	Parallel Faced (Rectangular) Bend . . . . .	1227
14.3.1	Preliminaries . . . . .	1227
14.3.2	Determination of Trajectories . . . . .	1229
14.3.3	Specification of Design Orbit . . . . .	1233
14.3.4	Expansion About the Design Orbit . . . . .	1236
14.3.5	Scaled and Dimensionless Deviation Variables . . . . .	1244
14.4	Hard-Edge Fringe Fields . . . . .	1245
14.5	Pole Face Rotations . . . . .	1245
14.6	General Bend . . . . .	1245
14.7	Combined Function Bend . . . . .	1245
<b>15</b>	<b>Taylor and Spherical and Cylindrical Harmonic Expansions</b>	<b>1247</b>
15.1	Introduction . . . . .	1247
15.2	Spherical Expansion . . . . .	1249
15.2.1	Harmonic Functions and Absolute and Expansion Coordinates . . . . .	1249
15.2.2	Spherical and Cylindrical Coordinates . . . . .	1250
15.2.3	Harmonic Polynomials, Harmonic Polynomial Expansions, and General Spherical Polynomials . . . . .	1251
15.2.4	Spherical Polynomial Vector Fields . . . . .	1253
15.2.5	Determination of Minimum Vector Potential: the Poincaré-Coulomb Gauge . . . . .	1254
15.2.6	Uniqueness of Poincaré-Coulomb Gauge . . . . .	1260
15.2.7	Direct Construction of Poincaré-Coulomb Gauge Vector Potential . . . . .	1261
15.3	Cylindrical Harmonic Expansion . . . . .	1269
15.3.1	Complex Cylindrical Harmonic Expansion . . . . .	1269
15.3.2	Real Cylindrical Harmonic Expansion in terms of Real On-axis Gradients . . . . .	1272
15.3.3	Some Simple Examples: $m = 0, 1, 2$ . . . . .	1276
15.3.4	Magnetic Field Expansions for the General Case . . . . .	1278
15.3.5	Symmetry and Allowed and Forbidden Multipoles . . . . .	1281
15.3.6	Relation between Harmonic Polynomials in Spherical and Cylindrical Coordinates . . . . .	1282
15.4	Determination of the Vector Potential: Azimuthal-Free Gauge . . . . .	1287
15.4.1	Derivation . . . . .	1288
15.4.2	Some Simple Examples: $m = 1, 2$ . . . . .	1290
15.5	Determination of the Vector Potential: Symmetric Coulomb Gauge . . . . .	1294
15.5.1	The $m = 0$ Case . . . . .	1294
15.5.2	The $m \geq 1$ Cases . . . . .	1298
15.6	Nonuniqueness of Coulomb Gauge . . . . .	1309
15.6.1	The General Case . . . . .	1309
15.6.2	Normal Dipole Example . . . . .	1311
15.7	Determination of the Vector Potential: Poincaré-Coulomb Gauge . . . . .	1316

15.7.1	The $m = 0$ Case . . . . .	1317
15.7.2	The $m \geq 1$ Cases . . . . .	1318
15.8	Relations Between Vector Potentials in Various Gauges and Associated Gauge Functions . . . . .	1323
15.8.1	Transformation Between Azimuthal-Free Gauge and Symmetric Coulomb Gauge . . . . .	1324
15.8.2	Transformation Between Symmetric Coulomb Gauge and Poincaré-Coulomb Gauge . . . . .	1325
15.8.3	Transformation Between Azimuthal-Free Gauge and Poincaré-Coulomb Gauge . . . . .	1328
15.9	Scalar Potentials from Sources . . . . .	1329
15.9.1	Preliminaries . . . . .	1329
15.9.2	Monopole Volume Distributions . . . . .	1329
15.9.3	Monopole Surface Distributions . . . . .	1330
15.9.4	Dipole Surface Distributions . . . . .	1330
15.9.5	Scalar Potential in Terms of Volume and Single and Double Layer Source Distributions . . . . .	1331
15.9.6	Green's Theorem . . . . .	1332
15.9.7	Application of Green's Theorem . . . . .	1332
15.10	Normal Magnetic Monopole Doublet Example and Applications . . . . .	1334
15.10.1	Magnetic Scalar Potential and Magnetic Field . . . . .	1334
15.10.2	Analytic On-Axis Gradients for the Normal Monopole Doublet . . . . .	1341
15.11	Minimum Vector Potential for Normal Magnetic Monopole Doublet . . . . .	1349
15.11.1	Computation from the Scalar Potential and Associated Magnetic Field . . . . .	1350
15.11.2	Computation from the On-Axis Gradients . . . . .	1351
15.12	Scalar Potentials Produced by Single-Layer Multipole Ring Sources . . . . .	1354
15.12.1	Normal Multipole Case . . . . .	1354
15.12.2	Skew Multipole Case . . . . .	1356
15.13	On-Axis Gradients for these Scalar Potentials . . . . .	1357
15.14	Approximating Delta, Signum, and Bump Functions . . . . .	1360
15.14.1	Approximating Delta Functions . . . . .	1360
15.14.2	Approximating Signum Functions . . . . .	1364
15.14.3	Approximating Bump Functions . . . . .	1367
15.15	Relation between Potentials Produced by Analogous Single- and Double-Layer Ring Sources . . . . .	1371
15.15.1	Double-Layer Ring Distributions . . . . .	1371
15.15.2	Explicit Formula Relating Potentials . . . . .	1373
15.15.3	Explicit Formula Relating On-Axis Gradients . . . . .	1375
15.15.4	Explicit Formula for Potential due to Double-Layer Ring Source . . . . .	1375
15.16	Potentials Produced by Single-Layer and Double-Layer Ring Sources Uniformly Distributed on a Cylindrical Surface . . . . .	1376
15.16.1	Use of Single-Layer Ring Source . . . . .	1376
15.16.2	Use of Double-Layer Ring Source . . . . .	1376
15.17	Closing Remarks . . . . .	1376

15.17.1	Caveat about Significance of Integrated Multipoles . . . . .	1376
15.17.2	Need for On-Axis Gradients and the Use of Surface Data . . . .	1378
15.17.3	Limitations Imposed by Symmetry and Hamilton and Maxwell .	1379
<b>16</b>	<b>Realistic Transfer Maps for Straight Iron-Free Beam-Line Elements</b>	<b>1385</b>
16.1	Terminating End Fields . . . . .	1385
16.1.1	Preliminary Observations . . . . .	1385
16.1.2	Matching Conditions . . . . .	1387
16.1.3	Changing Gauge . . . . .	1393
16.1.4	Application to Fringe-Field Termination . . . . .	1395
16.2	Solenoids . . . . .	1395
16.2.1	Preliminaries . . . . .	1396
16.2.2	Simple Air-Core Solenoid . . . . .	1398
16.2.3	Opposing Simple Solenoid Doublet . . . . .	1403
16.2.4	More Complicated Air-Core Solenoids . . . . .	1405
16.2.5	Computation of Transfer Map . . . . .	1406
16.2.6	Solenoidal Fringe-Field Effects: Attempts to Hard-Edge Model Them . . . . .	1411
16.2.7	Consequences of Terminating Solenoidal End Fields . . . . .	1432
16.3	Two Common Iron-Free Dipoles . . . . .	1445
16.3.1	Preliminaries . . . . .	1445
16.3.2	Current Windings for two Common Air-Core Dipoles . . . . .	1446
16.4	Bassetti-Biscari Windings for Pure Multipoles . . . . .	1451
16.4.1	Winding Geometry . . . . .	1452
16.4.2	Specification of Currents for a Pure Dipole . . . . .	1452
16.4.3	Description of Resulting On-Axis Gradient and On-Axis Field . .	1454
16.4.4	(Place Holder) Mathematical Model for a Pure Normal Dipole Based on both Single Layer and Double Layer Monopole Distribu- tions . . . . .	1456
16.4.5	Specification of Currents for a Pure Quadrupole . . . . .	1456
16.4.6	Description of Resulting On-Axis Gradient and On-Axis Field . .	1457
16.4.7	(Place Holder) Mathematical Model for a Pure Normal Quadrupole Based on both Single Layer and Double Layer Monopole Distribu- tions . . . . .	1460
16.4.8	Sextupoles and Beyond . . . . .	1460
16.5	Stream-Function Windings for Pure Multipoles . . . . .	1460
16.5.1	General Current Ansatz . . . . .	1460
16.5.2	Canonical Stream Function . . . . .	1461
16.5.3	Plan of Attack . . . . .	1464
16.5.4	Execution of Plan for the Solenoidal ( $m = 0$ ) Case . . . . .	1466
16.5.5	Preliminary Work for the Normal $m \geq 1$ Cases . . . . .	1469
16.5.6	Normal Dipole ( $m = 1$ ) Case . . . . .	1470
16.5.7	Continued Work on the General $m > 1$ Normal Cases . . . . .	1474
16.5.8	Final Results for the General $m > 1$ Normal Cases . . . . .	1482
16.5.9	Use of Vector Potential as a Stepping Stone . . . . .	1492



16.6	Rare Earth Cobalt (REC) Pure Multipoles . . . . .	1507
16.6.1	Description of Resulting On-Axis Gradient and On-Axis Field for a REC Quadrupole . . . . .	1507
16.6.2	Overlapping Fringe Fields . . . . .	1510
16.6.3	Hard-Edge Quadrupoles . . . . .	1510
16.6.4	Terminating Quadrupole End Fields . . . . .	1510
16.7	Lambertson Windings . . . . .	1516
16.8	Limited Utility of Cylindrical Harmonic Expansions for Dipoles . . . . .	1516
16.8.1	Terminating Dipole End Fields . . . . .	1518
16.8.2	Limited Utility of Hard-Edge Models for Dipole Fringe Fields . . . . .	1518
16.9	Air-Core Wiggler/Undulator Models . . . . .	1519
16.9.1	Simple Air-Core Wiggler/Undulator Model . . . . .	1519
16.9.2	Iron-Free Rare Earth Cobalt (REC) Wiggler/Undulator . . . . .	1520
16.9.3	Terminating Wiggler/Undulator End Fields . . . . .	1520
16.10	Lithium Lenses . . . . .	1527
<b>17</b>	<b>Surface Methods for General Straight Beam-Line Elements</b>	<b>1531</b>
17.1	Introduction . . . . .	1531
17.2	Use of Potential Data on Surface of Circular Cylinder . . . . .	1536
17.3	Use of Field Data on Surface of Circular Cylinder . . . . .	1539
17.4	Use of Field Data on Surface of Elliptical Cylinder . . . . .	1541
17.4.1	Background . . . . .	1541
17.4.2	Elliptic Coordinates . . . . .	1543
17.4.3	Mathieu Equations . . . . .	1545
17.4.4	Periodic Mathieu Functions and Separation Constants . . . . .	1546
17.4.5	Modified Mathieu Functions . . . . .	1561
17.4.6	Analyticity in $x$ and $y$ . . . . .	1565
17.4.7	Elliptic Cylinder Harmonic Expansion and On-Axis Gradients . . . . .	1565
17.5	Use of Field Data on Surface of Rectangular Cylinder . . . . .	1570
17.5.1	Finding the Magnetic Scalar Potential $\psi(x, y, z)$ . . . . .	1570
17.5.2	Finding the On-Axis Gradients . . . . .	1576
17.5.3	Fourier-Bessel Connection Coefficients . . . . .	1578
17.6	Attempted Use of Nearly On-Axis and Midplane Field Data . . . . .	1587
17.6.1	Use of Nearly On-Axis Data . . . . .	1587
17.6.2	Use of Midplane Field Data . . . . .	1589
17.7	Terminating End Fields . . . . .	1591
17.7.1	Preliminary Observations . . . . .	1591
17.7.2	Changing Gauge . . . . .	1593
17.7.3	Finding the Minimal Vector Potential . . . . .	1594
17.7.4	The $m = 0$ Case: Solenoid Example . . . . .	1599
17.7.5	The $m = 1$ Case: Magnetic Monopole Doublet and Wiggler Ex- amples . . . . .	1602
17.7.6	The $m = 2$ Case . . . . .	1605
17.7.7	The $m = 3$ Case . . . . .	1606
17.7.8	More Text . . . . .	1606



<b>18 Tools for Numerical Implementation</b>	<b>1613</b>
18.1 Third-Order Splines . . . . .	1613
18.1.1 Fitting Over an Interval . . . . .	1613
18.1.2 Periodic Splines . . . . .	1616
18.1.3 Error Estimate for Spline Approximation . . . . .	1618
18.2 Interpolation . . . . .	1620
18.2.1 Bicubic Interpolation . . . . .	1621
18.2.2 Bicubic Spline Interpolation . . . . .	1625
18.3 Fourier Transforms . . . . .	1626
18.3.1 Exact Fourier Transform and Its Large $ k $ Behavior . . . . .	1626
18.3.2 Inverse Fourier Transform . . . . .	1627
18.3.3 Discrete Fourier Transform . . . . .	1631
18.3.4 Discrete Inverse Fourier Transform . . . . .	1635
18.3.5 Spline-Based Fourier Transforms . . . . .	1635
18.3.6 Fast Spline-Based Fourier Transforms . . . . .	1645
18.4 Bessel Functions . . . . .	1646
18.5 Mathieu Functions . . . . .	1646
18.5.1 Calculation of Separation Constants $a_n(q)$ and $b_n(q)$ . . . . .	1646
18.5.2 Calculation of Mathieu Functions . . . . .	1646
18.5.3 Calculation of Fourier and Mathieu-Bessel Connection Coefficients	1649
<b>19 Numerical Benchmarks</b>	<b>1653</b>
19.1 Circular Cylinder Numerical Results for Monopole Doublet . . . . .	1653
19.1.1 Testing the Spline-Based Inverse ( $k \rightarrow z$ ) Fourier Transform . . .	1653
19.1.2 Testing the Forward ( $z \rightarrow k$ ) and ( $\phi \rightarrow m$ ) Fourier Transforms .	1660
19.1.3 Test of Interpolation off a Grid . . . . .	1664
19.1.4 Reproduction of Interior Field Values . . . . .	1666
19.2 Elliptical Cylinder Numerical Results for Monopole Doublet . . . . .	1679
19.2.1 Finding the Mathieu Coefficients . . . . .	1679
19.2.2 Behavior of Kernels . . . . .	1688
19.2.3 Truncation of Series . . . . .	1689
19.2.4 Approximation of Angular Integrals by Riemann Sums . . . . .	1695
19.2.5 Further Tests . . . . .	1704
19.2.6 Completion of Test . . . . .	1704
19.3 Rectangular Cylinder Numerical Results for Monopole Doublet . . . . .	1716
<b>20 Smoothing and Insensitivity to Errors</b>	<b>1719</b>
20.1 Introduction . . . . .	1719
20.1.1 Preliminary Considerations . . . . .	1719
20.1.2 Analyticity . . . . .	1719
20.1.3 Equivalent Spatial Kernel . . . . .	1720
20.1.4 What Work Lies Ahead . . . . .	1726
20.2 Circular Cylinders . . . . .	1726
20.3 Elliptic Cylinders . . . . .	1743
20.4 Rectangular Cylinders . . . . .	1767

<b>21</b>	<b>Realistic Transfer Maps for General Straight Beam-Line Elements</b>	<b>1771</b>
21.1	Solenoids . . . . .	1771
21.1.1	Preliminaries . . . . .	1771
21.1.2	Qualitatively Correct Iron-Dominated Solenoid Model . . . . .	1772
21.1.3	Improved Model for Iron-Dominated Solenoid . . . . .	1774
21.1.4	Quantitatively Correct Iron-dominated Solenoid . . . . .	1778
21.2	Realistic Wigglers/Undulators . . . . .	1778
21.2.1	An Iron-Dominated Superconducting Wiggler/Undulator . . . . .	1778
21.3	Quadrupoles . . . . .	1778
21.3.1	Validation of Circular Cylinder Surface Method . . . . .	1778
21.3.2	Final Focus Quadrupoles . . . . .	1785
21.4	Closely Adjacent Quadrupoles and Sextupoles . . . . .	1785
21.5	Application to Radio-Frequency Cavities . . . . .	1785
<b>22</b>	<b>Realistic Transfer Maps for General Curved Beam-Line Elements: Theory</b>	<b>1791</b>
22.1	Introduction . . . . .	1791
22.2	Mathematical Tools . . . . .	1793
22.2.1	Electric Dirac Strings . . . . .	1793
22.2.2	Magnetic Dirac Strings . . . . .	1797
22.2.3	Helmholtz Decomposition . . . . .	1804
22.3	Construction of Kernels $G^n$ and $G^t$ . . . . .	1812
22.3.1	Background . . . . .	1812
22.3.2	Construction of $\mathbf{G}^n$ Using Half-Infinite String Monopoles . . . . .	1812
22.3.3	Discussion . . . . .	1814
22.3.4	Construction of $\mathbf{G}^t$ . . . . .	1815
22.3.5	Final Discussion . . . . .	1817
22.4	Expansion of Kernels . . . . .	1821
22.4.1	Our Goal . . . . .	1821
22.4.2	Binomial Theorem . . . . .	1821
22.4.3	Expansion of $\mathbf{G}^t(\mathbf{r}, \mathbf{r}')$ . . . . .	1821
22.4.4	Expansion of $\mathbf{G}^n(\mathbf{r}, \mathbf{r}')$ . . . . .	1821
<b>23</b>	<b>Realistic Transfer Maps for General Curved Beam-Line Elements: Exact Monopole Doublet Results</b>	<b>1825</b>
23.1	Magnetic Monopole Doublet Vector Potential . . . . .	1825
23.2	Selection of Hamiltonian and Scaled Variables . . . . .	1829
23.3	Design Orbit and Fields . . . . .	1830
23.4	Terminating End Fields . . . . .	1842
23.4.1	Minimum Vector Potential for End Fields . . . . .	1842
23.4.2	Associated Termination Error . . . . .	1842
23.4.3	Taylor Expansion of String Vector Potential . . . . .	1845
23.4.4	Finding the Associated Gauge Function . . . . .	1846
23.5	Gauge Transformation Map . . . . .	1846
23.6	Pole Face Rotation . . . . .	1846

23.7	Computation of Transfer Map . . . . .	1846
23.8	Scraps . . . . .	1846
<b>24</b>	<b>Realistic Transfer Maps for General Curved Beam-Line Elements: Bent Box Monopole Doublet Results</b>	<b>1849</b>
24.1	Choice of Surrounding Bent Box . . . . .	1849
24.2	Comparison of Fields . . . . .	1851
24.2.1	Preliminaries . . . . .	1851
24.2.2	Evaluation of Surface Integrals . . . . .	1854
24.2.3	Resulting Vector Potential . . . . .	1857
24.2.4	Comparison of Fields . . . . .	1857
24.3	Comparison of Design Orbits . . . . .	1863
24.4	Terminating End Fields . . . . .	1863
24.5	Gauge Transformation Map . . . . .	1866
24.6	Pole Face Rotation . . . . .	1866
24.7	Comparison of Maps . . . . .	1866
24.8	Smoothing and Insensitivity to Errors . . . . .	1866
<b>25</b>	<b>Realistic Transfer Maps for General Curved Beam-Line Elements: Application to a Storage-Ring Dipole</b>	<b>1869</b>
<b>26</b>	<b>The Euclidean Group and Error Effects</b>	<b>1873</b>
26.1	The Euclidean Group . . . . .	1873
<b>27</b>	<b>Representations of <math>sp(2n)</math> and Related Matters</b>	<b>1875</b>
27.1	Structure of $sp(2, \mathbb{R})$ . . . . .	1876
27.2	Representations of $sp(2, \mathbb{R})$ . . . . .	1878
27.3	Symplectic Classification of Analytic Vector Fields in Two Variables . . .	1882
27.4	Structure of $sp(4, \mathbb{R})$ . . . . .	1891
27.5	Representations of $sp(4, \mathbb{R})$ . . . . .	1894
27.6	Symplectic Classification of Analytic Vector Fields in Four Variables . . .	1905
27.7	Structure of $sp(6, \mathbb{R})$ . . . . .	1910
27.8	Representations of $sp(6, \mathbb{R})$ . . . . .	1914
27.9	Symplectic Classification of Analytic Vector Fields in Six Variables . . . .	1920
27.10	Scalar Product and Projection Operators for Vector Fields . . . . .	1925
27.11	Products and Casimir Operators . . . . .	1934
27.11.1	The Quadratic Casimir Operator . . . . .	1934
27.11.2	Applications of the Quadratic Casimir Operator . . . . .	1940
27.11.3	Higher-Order Casimir Operators . . . . .	1944
27.12	The Killing Form . . . . .	1949
27.13	Enveloping Algebra . . . . .	1951
27.14	The Symplectic Lie Algebras $sp(8)$ and Beyond . . . . .	1958
27.15	Momentum Maps, Noether's Theorem, and Casimirs . . . . .	1959
27.15.1	Momentum Maps, Noether's Theorem, and Conservation Laws . . . . .	1959
27.15.2	Use of Casimirs . . . . .	1962

<b>28 More About Various Groups and their Interrelations and other Miscellanea</b>	<b>1971</b>
<b>29 Numerical Study of Stroboscopic Duffing Map</b>	<b>2089</b>
29.1 Introduction . . . . .	2089
29.2 Review of Simple Harmonic Oscillator Behavior . . . . .	2090
29.3 Behavior for Small Driving when Nonlinearity is Included . . . . .	2094
29.4 What Happens Initially When the Driving Is Increased? . . . . .	2096
29.4.1 Saddle-Node (Blue-Sky) Bifurcations . . . . .	2096
29.4.2 Basins . . . . .	2099
29.4.3 Symmetry . . . . .	2099
29.4.4 Amplitude Jumps . . . . .	2101
29.4.5 Hysteresis . . . . .	2102
29.5 Pitchfork Bifurcations and Symmetry . . . . .	2103
29.6 Period Tripling Bifurcations and Fractal Basin Boundaries . . . . .	2108
29.7 Asymptotic $\omega$ Behavior . . . . .	2114
29.8 Period Doubling Cascade . . . . .	2119
29.9 Strange Attractor . . . . .	2126
29.10 Acknowledgment . . . . .	2127
<b>30 General Maps</b>	<b>2131</b>
30.1 Lie Factorization of General Maps . . . . .	2131
30.2 Classification of General Two-Dimensional Quadratic Maps . . . . .	2136
30.3 Lie Factorization of General Two-Dimensional Quadratic Maps . . . . .	2141
30.4 Fixed Points . . . . .	2150
30.4.1 Attack a Map at its Fixed Points . . . . .	2150
30.4.2 Fixed Points are Generally Isolated . . . . .	2150
30.4.3 Finding Fixed Points with Contraction Maps . . . . .	2151
30.4.4 Persistence of Fixed Points . . . . .	2153
30.4.5 Application to Accelerator Physics . . . . .	2156
30.5 Poincaré Index . . . . .	2161
30.6 Manifolds, and Homoclinic Points and Tangles . . . . .	2174
30.7 The General Hénon Map . . . . .	2185
30.8 Preliminary Study of General Hénon Map . . . . .	2193
30.8.1 Location, Expansion About, and Nature of Fixed Points . . . . .	2193
30.8.2 Lie Factorization About the First (Hyperbolic) Fixed Point . . . . .	2200
30.8.3 Location and Nature of Second Fixed Point . . . . .	2203
30.8.4 Expansion and Lie Factorization About Second Fixed Point . . . . .	2212
30.9 Period Doubling and Strange Attractors . . . . .	2218
30.9.1 Behavior about Hyperbolic Fixed Point . . . . .	2218
30.9.2 Behavior about Second Fixed Point . . . . .	2218
30.10 Attempts at Integrals . . . . .	2220
30.11 Quadratic Maps in Higher Dimensions . . . . .	2220
30.12 Truncated Taylor Approximations to Stroboscopic Duffing Map . . . . .	2220
30.12.1 Saddle-Node Bifurcations . . . . .	2220

30.12.2	Pitchfork Bifurcations . . . . .	2234
30.12.3	Infinite Period-Doubling Cascade and Strange Attractor . . . . .	2242
30.12.4	Undoing a Cascade by Successive Mergings . . . . .	2256
30.12.5	Convergence of Taylor Maps: Performance of Lower-Order Polynomial Approximations . . . . .	2263
30.12.6	Concluding Summary and Discussion . . . . .	2269
30.12.7	Acknowledgment . . . . .	2270
30.13	Analytic Properties of Fixed Points and Eigenvalues . . . . .	2270
<b>31</b>	<b>Normal Forms for Symplectic Maps and Their Applications</b>	<b>2277</b>
31.1	Equivalence Relations . . . . .	2277
31.2	Symplectic Conjugacy of Symplectic Maps . . . . .	2278
31.3	Normal Forms for Maps . . . . .	2278
31.4	Sample Normal Forms . . . . .	2280
31.5	Static Maps Without Translation Factor . . . . .	2281
31.5.1	Properties of Linear Part . . . . .	2281
31.6	Static Maps With Translation Factor . . . . .	2287
31.7	Tunes, Phase Advances and Slips, Momentum Compaction, Chromaticities, and Anharmonicities . . . . .	2287
31.8	Courant-Snyder Invariants and Lattice Functions . . . . .	2287
31.9	Dynamic Maps Without Translation Factor . . . . .	2287
31.10	Dynamic Maps With Translation Factor . . . . .	2287
31.11	Analysis of Tracking Data . . . . .	2287
<b>32</b>	<b>Lattice Functions</b>	<b>2291</b>
<b>33</b>	<b>Solved and Unsolved Polynomial Orbit Problems: Invariant Theory</b>	<b>2293</b>
33.1	Introduction . . . . .	2293
33.2	Solved Polynomial Orbit Problems . . . . .	2295
33.2.1	First-Order Polynomials . . . . .	2295
33.2.2	Second-Order Polynomials . . . . .	2296
33.3	Mostly Unsolved Polynomial Orbit Problems . . . . .	2324
33.3.1	Cubic Polynomials . . . . .	2325
33.3.2	Quartic Polynomials . . . . .	2325
33.4	Application to Analytic Properties . . . . .	2327
<b>34</b>	<b>Beam Description and Moment Transport</b>	<b>2339</b>
34.1	Preliminaries . . . . .	2339
34.2	Moments and Moment Transport . . . . .	2340
34.3	Various Beam Distributions and Beam Matching . . . . .	2341
34.4	Some Properties of First-Order Moments . . . . .	2341
34.4.1	Transformation Properties . . . . .	2341
34.4.2	Normal Form . . . . .	2343
34.5	Kinematic Moment Invariants . . . . .	2343
34.6	Some Properties of Second-Order Moments . . . . .	2345

34.6.1	Positive Definite Property . . . . .	2345
34.6.2	Transformation Properties . . . . .	2345
34.6.3	Williamson Normal Form . . . . .	2347
34.6.4	Eigen Emittances . . . . .	2347
34.6.5	Classical Uncertainty Principle . . . . .	2350
34.6.6	Minimum Emittance Theorem . . . . .	2351
34.6.7	Nonexistence of Maximum Emittances . . . . .	2354
34.6.8	Second-Order Moments about the Beam Centroid . . . . .	2355
34.6.9	Summary of What We Have Learned . . . . .	2357
34.7	Construction of Initial Distributions with Small/Optimized Eigen Emittances	2362
34.8	Realization of Eigen Emittances as Mean-Square Emittances . . . . .	2362
<b>35</b>	<b>Optimal Evaluation of Symplectic Maps</b>	<b>2365</b>
35.1	Overview of Symplectic Map Approximation . . . . .	2365
35.2	Symplectic Completion of Symplectic Jets . . . . .	2371
35.2.1	Criteria . . . . .	2371
35.2.2	Monomial Approximation . . . . .	2371
35.2.3	Generating Function Approximation . . . . .	2371
35.2.4	Cremona Maps . . . . .	2371
35.3	Connection Between Mixed-Variable Generating Functions and Lie Generators . . . . .	2371
35.3.1	Method of Calculation . . . . .	2372
35.3.2	Computing $g_2$ . . . . .	2374
35.3.3	Low Order Results: Computing $g_3$ and $g_4$ . . . . .	2375
35.3.4	Two Examples . . . . .	2378
35.3.5	Exploration . . . . .	2379
35.3.6	Comments and Comparisons . . . . .	2389
35.4	Use of Poincaré Generating Function . . . . .	2393
35.4.1	Determination of Poincaré Generating Function in Terms of $H$ . . . . .	2393
35.4.2	Application to Quadratic Hamiltonian . . . . .	2394
35.4.3	Application to Symplectic Approximation . . . . .	2395
35.5	Use of Other Generating Functions . . . . .	2397
35.6	Cremona Approximation . . . . .	2398
<b>36</b>	<b>Orbit Stability, Long-Term Behavior, and Dynamic Aperture</b>	<b>2403</b>
<b>37</b>	<b>Reversal Symmetry</b>	<b>2405</b>
37.1	Reversal Operator . . . . .	2405
37.2	Applications . . . . .	2411
37.3	General Consequences for Straight and Circular Machines . . . . .	2419
37.4	Consequences for some Special Cases . . . . .	2424
37.5	Consequences for Closed Orbit in a Circular Machine . . . . .	2425
37.6	Consequences for Courant-Snyder Functions in a Circular Machine . . . . .	2430
37.7	Some Nonlinear Consequences . . . . .	2436

<b>38 Standard First- and Higher-Order Optical Modules</b>	<b>2447</b>
<b>39 Analyticity and Convergence</b>	<b>2449</b>
39.1 Analyticity in One Complex Variable . . . . .	2449
39.2 Analyticity in Several Complex Variables . . . . .	2453
39.3 Convergence of Homogeneous Polynomial Series . . . . .	2466
39.4 Application to Potentials and Fields . . . . .	2474
39.5 Application to Taylor Maps: The Anharmonic Oscillator . . . . .	2474
39.6 Application to Taylor Maps: The Pendulum . . . . .	2474
39.7 Convergence of the BCH Series . . . . .	2474
39.8 Convergence of Lie Transformations and the Factored Product Representation	2474
<b>40 Truncated Power Series Algebra</b>	<b>2479</b>
40.1 Introduction . . . . .	2479
40.2 Monomial Indexing . . . . .	2480
40.2.1 An Obvious but Memory Intensive Method . . . . .	2480
40.2.2 Polynomial Grading . . . . .	2481
40.2.3 Monomial Ordering . . . . .	2481
40.2.4 Labeling Based on Ordering . . . . .	2483
40.2.5 Formulas for Lowest and Highest Indices . . . . .	2484
40.2.6 The Giorgilli Formula . . . . .	2486
40.2.7 Finding the Required Binomial Coefficients . . . . .	2487
40.2.8 Computation of the Index $i$ Given the Exponent Array $j$ . . . .	2489
40.2.9 Preparing a Look-Up Table for the Exponent Array $j$ Given the Index $i$ . . . . .	2490
40.2.10 Verification of the Giorgilli Formula . . . . .	2493
40.3 Scalar Multiplication and Polynomial Addition . . . . .	2498
40.4 Polynomial Multiplication . . . . .	2499
40.5 Look-Up Tables . . . . .	2500
40.6 Scripts . . . . .	2506
40.7 Look-Back Tables . . . . .	2513
40.8 Poisson Bracketing . . . . .	2521
40.9 Linear Map Action . . . . .	2529
40.10 General Vector Fields . . . . .	2532
40.11 Expanding Functions of Polynomials . . . . .	2534
40.12 Automatic Differentiation/Differential Algebra . . . . .	2534
40.13 Other Methods . . . . .	2534
<b>A Størmer-Cowell and Nyström Integration Methods</b>	<b>2537</b>
A.1 Preliminary Derivation of Størmer-Cowell Method . . . . .	2537
A.2 Summed Formulation . . . . .	2539
A.2.1 Procedure . . . . .	2539
A.2.2 Derivation . . . . .	2540
A.3 Computation of First Derivative . . . . .	2542



A.4	Example Program and Numerical Results . . . . .	2543
A.4.1	Program . . . . .	2543
A.4.2	Numerical Results . . . . .	2546
A.5	Nyström Runge-Kutta Methods . . . . .	2547
<b>B</b>	<b>Computer Programs for Numerical Integration</b>	<b>2553</b>
B.1	A 3 <sup>rd</sup> Order Runge-Kutta Routine . . . . .	2554
B.1.1	Butcher Tableau for <i>RK3</i> . . . . .	2554
B.1.2	The Routine <i>RK3</i> . . . . .	2554
B.2	A 4 <sup>th</sup> Order Runge-Kutta Routine . . . . .	2555
B.2.1	Butcher Tableau for <i>RK4</i> . . . . .	2555
B.2.2	The Routine <i>RK4</i> . . . . .	2555
B.3	A Subroutine to Compute <b>f</b> . . . . .	2556
B.4	A Partial Double-Precision Version of <i>RK3</i> . . . . .	2557
B.5	A 6 <sup>th</sup> Order 8 Stage Runge-Kutta Routine . . . . .	2559
B.5.1	Butcher Tableau for <i>RK6</i> . . . . .	2559
B.5.2	The Routine <i>RK6</i> . . . . .	2559
B.6	Embedded Runge-Kutta Pairs . . . . .	2561
B.6.1	Preliminaries . . . . .	2561
B.6.2	Fehlberg 4(5) Pair . . . . .	2562
B.6.3	Dormand-Prince 5(4) Pair . . . . .	2564
B.7	A 5 <sup>th</sup> Order PECEC Adams Routine . . . . .	2566
B.8	A 10 <sup>th</sup> Order PECEC Adams Routine . . . . .	2568
<b>C</b>	<b>Baker-Campbell-Hausdorff and Zassenhaus Formulas, Bases, and Paths</b>	<b>2573</b>
C.1	Differentiating the Exponential Function . . . . .	2573
C.2	The Baker-Campbell-Hausdorff Formula . . . . .	2573
C.3	The Baker-Campbell-Hausdorff Series . . . . .	2573
C.4	Zassenhaus Formulas . . . . .	2577
C.5	Bases . . . . .	2577
C.6	Paths . . . . .	2577
C.6.1	Paths in the Group Yield Paths in the Lie Algebra . . . . .	2577
C.6.2	Paths in the Lie Algebra Yield Paths in the Group . . . . .	2577
C.6.3	Differential Equations . . . . .	2577
<b>D</b>	<b>Canonical Transformations</b>	<b>2581</b>
<b>E</b>	<b>Mathematica Notebooks</b>	<b>2583</b>
<b>F</b>	<b>Properties of Harmonic Functions, Analyticity, Aberration Expansions, and Smoothing</b>	<b>2585</b>
F.1	The Static Case . . . . .	2585
F.2	The Time Dependent Case . . . . .	2597
F.3	Smoothing Properties of the Laplacian Kernel . . . . .	2599
<b>G</b>	<b>Specification of <math>m \geq 1</math> Current Filaments/Windings</b>	<b>2603</b>



<b>H</b>	<b>Harmonic Functions</b>	<b>2605</b>
H.1	Representation of Gradients . . . . .	2605
H.1.1	Low-Order Results . . . . .	2605
H.1.2	Results to All Orders . . . . .	2607
H.2	Range of Transverse Gradient Operators . . . . .	2616
H.2.1	Solution of $\partial_x \psi = \chi$ . . . . .	2616
H.2.2	Solution of $\partial_y \psi = \chi$ . . . . .	2620
H.3	Harmonic Functions in Two Variables and Their Associated Fields . . . .	2623
H.3.1	Harmonic Functions in $x, z$ . . . . .	2624
H.3.2	Harmonic Functions in $y, z$ . . . . .	2627
H.3.3	More About $\mathbf{B}^{od}(y, z)$ and Another Application of Analytic Function Theory . . . . .	2628
<b>I</b>	<b>Poisson Bracket Relations</b>	<b>2633</b>
I.1	Poisson Brackets . . . . .	2633
I.2	Preparatory Results . . . . .	2635
I.3	Application . . . . .	2636
<b>J</b>	<b>Feigenbaum Cascade Denied/Achieved</b>	<b>2639</b>
J.1	Simple Map and Its Initial Bifurcations . . . . .	2639
J.2	Complete Cascade Denied . . . . .	2640
J.3	Complete Cascade Achieved . . . . .	2642
<b>K</b>	<b>Supplement to Chapter 17</b>	<b>2647</b>
K.1	Computation of On-Axis Gradients from Spinning Coil Data . . . . .	2647
K.2	Computation of On-Axis Gradients from Coil Geometry and Current Data	2649
<b>L</b>	<b>Spline Routines</b>	<b>2653</b>
<b>M</b>	<b>Routines for Mathieu Separation Constants <math>a_n(q)</math> and <math>b_n(q)</math></b>	<b>2659</b>
<b>N</b>	<b>Mathieu-Bessel Connection Coefficients</b>	<b>2667</b>
<b>O</b>	<b>Quadratic Forms</b>	<b>2669</b>
O.1	Background . . . . .	2669
O.2	Effect of Small Perturbations in the Definite Case . . . . .	2670
<b>P</b>	<b>Parameterization of the Coset Space <math>GL(2n, \mathbb{R})/Sp(2n, \mathbb{R})</math></b>	<b>2673</b>
P.1	Introduction . . . . .	2673
P.2	$M$ Must Have Positive Determinant . . . . .	2673
P.3	It is Sufficient to Consider $SL(2n, \mathbb{R})/Sp(2n, \mathbb{R})$ . . . . .	2674
P.4	Some Symmetries . . . . .	2674
P.5	Connection between Symmetries and Being $J$ -Symmetric . . . . .	2676
P.6	Relation to Darboux Matrices . . . . .	2677
P.7	Some Observations on $SL(2n, \mathbb{R})/Sp(2n, \mathbb{R})$ . . . . .	2678
P.8	Action of $\sigma$ on $sl(2n, \mathbb{R})$ . . . . .	2678

P.9	Lie Triple System . . . . .	2679
P.10	A Factorization Theorem (Theorem 1.1 of Goodman) . . . . .	2680
P.10.1	A Particular Mapping from Real Symmetric Matrices to Positive- Definite Matrices . . . . .	2680
P.10.2	The Map Is Real Analytic . . . . .	2680
P.10.3	Trace and Determinant Properties . . . . .	2681
P.10.4	Study of the Inverse of the Map . . . . .	2681
P.10.5	Formula for $S^a$ in terms of $Z$ . . . . .	2681
P.10.6	Uniqueness of Solution for $S^a$ . . . . .	2682
P.10.7	Verification of Expected Symmetry for $S^a$ . . . . .	2683
P.10.8	Formula for $S^c$ in Terms of $Z$ . . . . .	2683
P.10.9	Verification of Expected Symmetry for $S^c$ . . . . .	2684
P.10.10	Conclusion . . . . .	2684
P.10.11	Motivation for Mapping . . . . .	2684
P.11	Theorem 1.2 of Goodman Due to Mostow . . . . .	2685
P.12	Goodman's Work on Symplectic Polar Decomposition . . . . .	2687
P.12.1	Some More Symmetry Operations . . . . .	2687
P.12.2	Fixed-Point Subgroups Associated with Symmetry Operations . . . . .	2690
P.13	Decomposition of Lie Algebras . . . . .	2693
P.14	Preparation for Lemma 2.1 of Goodman . . . . .	2697
P.15	Lemma 2.1 of Goodman . . . . .	2697
P.16	Preparation for Theorem 2.1 of Goodman . . . . .	2699
P.17	Theorem 2.1 of Goodman . . . . .	2701
P.18	Search for Counter Examples . . . . .	2703
<b>Q</b>	<b>Improving Convergence of Fourier Representation</b>	<b>2707</b>
Q.1	Introduction . . . . .	2707
Q.2	Application . . . . .	2709
<b>R</b>	<b>Abstract Lie Group Theory</b>	<b>2713</b>
<b>S</b>	<b>Mathematica Realization of TPSA and Taylor Map Computation</b>	<b>2717</b>
S.1	Background . . . . .	2717
S.2	AD Tools . . . . .	2718
S.2.1	Labeling Scheme . . . . .	2718
S.2.2	Implementation of Labeling Scheme . . . . .	2721
S.2.3	Pyramid Operations: General Procedure . . . . .	2724
S.2.4	Pyramid Operations: Scalar Multiplication and Addition . . . . .	2724
S.2.5	Pyramid Operations: Background for Polynomial Multiplication . . . . .	2725
S.2.6	Pyramid Operations: Implementation of Multiplication . . . . .	2728
S.2.7	Pyramid Operations: Implementation of Powers . . . . .	2736
S.2.8	Replacement Rule and Automatic Differentiation . . . . .	2736
S.2.9	Taylor Rule . . . . .	2739
S.3	Numerical Integration and Replacement Rule . . . . .	2742

S.3.1	Numerical Integration . . . . .	2742
S.3.2	Replacement Rule, Single Equation/Variable Case . . . . .	2743
S.3.3	Multi Equation/Variable Case . . . . .	2746
S.4	Duffing Equation Application . . . . .	2749
S.5	Relation to the Complete Variational Equations . . . . .	2752
S.6	Acknowledgment . . . . .	2755
<b>T</b>	<b>Quadrature and Cubature Formulas</b>	<b>2759</b>
T.1	Quadrature Formulas . . . . .	2759
T.1.1	Introduction . . . . .	2759
T.1.2	Newton Cotes . . . . .	2761
T.1.3	Legendre Gauss . . . . .	2762
T.1.4	Clenshaw Curtis . . . . .	2764
T.1.5	Convergence . . . . .	2765
T.1.6	Quadrature on a Circle/One-Sphere . . . . .	2766
T.2	Cubature Formulas . . . . .	2771
T.2.1	Introduction . . . . .	2771
T.2.2	Cubature on a Square . . . . .	2771
T.2.3	Cubature on a Rectangle . . . . .	2776
T.2.4	Cubature on the Two-Sphere . . . . .	2780
<b>U</b>	<b>Rotational Classification and Properties of Polynomials and Analytic/Polynomial Vector Fields</b>	<b>2783</b>
U.1	Introduction . . . . .	2783
U.2	Polynomials and Spherical Polynomials . . . . .	2783
U.2.1	Polynomials . . . . .	2783
U.2.2	Spherical Polar Coordinates and Harmonic Polynomials . . . . .	2784
U.2.3	Examples of Harmonic Polynomials and Missing Homogeneous Polynomials . . . . .	2785
U.2.4	Spherical Polynomials . . . . .	2785
U.3	Analytic/Polynomial Vector Fields and Spherical Polynomial Vector Fields	2786
U.3.1	Vector Spherical Harmonics . . . . .	2786
U.3.2	Spherical Polynomial Vector Fields . . . . .	2788
U.3.3	Examples of and Counting Spherical Polynomial Vector Fields . . . . .	2788
U.4	Independence/Orthogonality/Integral Properties of Polynomials and Poly- nomial Vector Fields . . . . .	2792
U.4.1	Polynomial Results . . . . .	2792
U.4.2	Polynomial Vector Field Results . . . . .	2794
U.5	Differential Properties of Spherical Polynomials and Spherical Polynomial Vector Fields . . . . .	2797
U.5.1	Gradient Action on Spherical Polynomials . . . . .	2797
U.5.2	Divergence Action on Spherical Polynomial Vector Fields . . . . .	2798
U.5.3	Curl Action on Spherical Polynomial Vector Fields . . . . .	2798
U.6	Multiplicative Properties of Spherical Polynomials and Spherical Polyno- mial Vector Fields . . . . .	2799

U.6.1	Ordinary Multiplication . . . . .	2800
U.6.2	Dot Product Multiplication . . . . .	2800
U.6.3	Cross Product Multiplication . . . . .	2801
<b>V</b>	<b>PROT without and in the Presence of a Magnetic Field</b>	<b>2807</b>
V.1	The Case of No Magnetic Field . . . . .	2807
V.2	The Constant Magnetic Field Case . . . . .	2807
V.2.1	Preliminaries . . . . .	2807
V.2.2	Dimensionless Variables and Limiting Hamiltonian . . . . .	2808
V.2.3	Design Trajectory . . . . .	2809
V.2.4	Deviation Variables . . . . .	2810
V.2.5	Deviation Variable Hamiltonian . . . . .	2810
V.2.6	Computation of Transfer Map . . . . .	2810
V.3	The Inhomogeneous Field Case . . . . .	2812
V.3.1	Vector Potential for the General Inhomogeneous Field Case . . .	2812
V.3.2	Transition to Cylindrical Coordinates . . . . .	2813
V.3.3	Dimensionless Variables and Limiting Vector Potential . . . . .	2814
V.3.4	Computation of Limiting Hamiltonian in Dimensionless Variables	2815
V.3.5	Deviation Variable Hamiltonian . . . . .	2815
V.3.6	Expansion of Deviation Variable Hamiltonian and Computation of Transfer Map . . . . .	2816
<b>W</b>	<b>Smoothing for Harmonic Functions</b>	<b>2819</b>
W.1	Introduction . . . . .	2819
W.2	The Line in Two Space . . . . .	2819
W.3	The Plane in Three Space . . . . .	2823
W.4	The Circle in Two Space . . . . .	2828
W.5	The Circular Cylinder in Three Space . . . . .	2833
W.6	The Ellipse in Two Space . . . . .	2840
W.7	The Elliptical Cylinder in Three Space . . . . .	2848
W.8	The Rectangle in Two Space . . . . .	2848
W.9	The Rectangular Cylinder in Three Space . . . . .	2848
W.10	The Sphere in Three Space . . . . .	2848
W.11	The Ellipsoid in Three Space . . . . .	2848
<b>X</b>	<b>Lie Algebraic Theory of Light Optics</b>	<b>2851</b>
X.1	Hamiltonian Formulation . . . . .	2851
X.2	Assumption of Axial Symmetry and Lie-algebraic Consequences . . . .	2854
X.2.1	Preliminaries . . . . .	2854
X.2.2	What Generators Can Occur and Their Relation to Aberrations .	2856
X.2.3	Equivariance . . . . .	2860
X.3	Lie-Algebraic Decomposition of Polynomials . . . . .	2864
X.3.1	Introduction of $sp(2, \mathbb{R})$ . . . . .	2864
X.3.2	Fourth Degree Homogeneous Polynomials . . . . .	2865
X.3.3	Second Degree Homogeneous Polynomials . . . . .	2868

X.3.4	Sixth and Eighth Degree Homogeneous Polynomials . . . . .	2870
X.3.5	Proof of Orthogonality and Definition/Use of the Quadratic Casimir Operator . . . . .	2871
X.4	Applications of Multiplet Decompositions . . . . .	2877
X.5	Wave Aberrations . . . . .	2886
X.6	Maps/Lie Generators for Continuous Systems . . . . .	2891
X.7	Maps/Lie Generators for Discontinuous Systems . . . . .	2891
X.8	Three Sample Designs . . . . .	2893
X.8.1	Aberration Corrected Spot-Forming System . . . . .	2893
X.8.2	Aberration Corrected Doublet Imaging System . . . . .	2893
X.8.3	Aberration Corrected Hubble and James Webb Telescopes . . . .	2910
X.9	Inclusion of Chromatic Effects . . . . .	2910
X.10	Possibly Complementary Approaches . . . . .	2910
X.10.1	The Constant Index Case . . . . .	2910
X.10.2	The Graded Index Case . . . . .	2911
<b>Y</b>	<b>Relation between the Classical Poisson Bracket Lie Algebra and the Quantum Commutator-Based Lie Algebra</b>	<b>2917</b>
Y.1	Classical Polynomial Basis . . . . .	2917
Y.2	Quantum Polynomial Basis . . . . .	2919
Y.3	A Natural Correspondence between Classical and Quantum Bases . . . .	2920
Y.4	Relation between the Lie Algebras $\mathcal{L}_{\text{cm}}$ and $\mathcal{L}_{\text{qm}}$ . . . . .	2921
Y.5	Historical Comment . . . . .	2923



# List of Figures

0.0.1	The Ancient of Days. “If the doors of perception were cleansed, everything would appear to man as it is: Infinite.” William Blake (1757-1827)	lxx
1.1.1	In Dynamics the future can be determined by performing a certain operation, called a mapping $\mathcal{M}$ , on the present. . . . .	4
1.2.1	The insect populations in two successive years are related by a map $\mathcal{M}$ .	12
1.2.2	The values $x_m$ as a function $m$ for the case $\lambda = 2.8$ . . . . .	14
1.2.3	The values $x_m$ as a function $m$ for the case $\lambda = 3.01$ . . . . .	15
1.2.4	Feigenbaum diagram showing limiting values $x_\infty$ as a function of $\lambda$ for the logistic map. . . . .	17
1.2.5	An enlargement of Figure 2.4 exhibiting how successive bifurcations scale.	19
1.2.6	Douady’s rabbit, the dynamic aperture in the mapping plane $z$ for the case $\gamma = 2.55268 - 0.959456i$ . . . . .	22
1.2.7	The Mandelbrot set $M$ in the control plane $\gamma$ . . . . .	22
1.2.8	Douady’s rabbit in color. The white points lie in the basin of $\infty$ under the action of $\mathcal{M}$ . The origin is a repelling fixed point of $\mathcal{M}$ . The other repelling fixed point has the location $z_f = .656747 - .129015i$ . Under the action of $\mathcal{M}^3$ , red points lie in the basin of $z^1$ , green points lie in the basin of $z^2$ , and yellow points lie in the basin of $z^3$ . . . . .	25
1.2.9	Schematic representation of the map (2.50). . . . .	28
1.2.10	The dynamic aperture of the Hénon map for the case $\theta/2\pi = 0.22$ . . . .	29
1.2.11	Stereographic view of the dynamic aperture of the Hénon map as a function of the parameter $\theta$ . The region shown is $q \in [-.8, .8]$ , $p \in [-.7.7]$ , $\theta/2\pi \in [0, .5]$ . . . . .	30
1.2.12	The Mandelbrot set in the $\mu$ plane. The “plate” has been somewhat “overexposed” compared to Figure 2.7 to bring out the island chains. .	47
1.2.13	The analog of Figure 2.4 for $\mu$ real and the variable $w$ . . . . .	47
1.3.1	An illustration of Theorem 3.1 in the case that “ $\mathbf{y}$ ” space is two dimensional. The solution $\mathbf{y}$ exists, is unique, and is continuous in $t$ as long as it remains within the large cylinder of base $R$ where $\mathbf{f}$ is continuous and the $\partial\mathbf{f}/\partial y_j$ are continuous. If the point $\mathbf{y}^0$ is varied slightly, the solution also changes only slightly so that nearby solutions form a bundle. . . .	57
1.4.1	The transfer map $\mathcal{M}$ sends the initial conditions $\mathbf{y}^i$ to the final conditions $\mathbf{y}^f$ . . . . .	61
1.5.1	Illustration of the $\rho, y, \phi$ cylindrical coordinate system and a sample unit-vector pair $\mathbf{e}_\rho$ and $\mathbf{e}_\phi$ . . . . .	78

1.6.1	Typical choice of a Cartesian coordinate system for the description of charged-particle trajectories in a magnet. . . . .	88
1.6.2	Top view of a particle trajectory in a rectangular magnet. . . . .	89
1.6.3	Top view of a particle trajectory in a wedge magnet. The trajectory is conveniently described using the cylindrical coordinates $\rho, y, \phi$ . See Figure 5.1. . . . .	89
2.1.1	The Time Axis . . . . .	168
2.3.1	The result of integrating with RK3 the set (2.7) through (2.9) to $t = 1.5$ with several different step sizes to illustrate how the cumulative error depends on $h$ . The error is measured by $\ \mathbf{y}(1.5) - \mathbf{y}_e(1.5)\ $ where $\mathbf{y}_e$ is the exact solution. The dashed line on the right has a slope of $+3$ showing that the global truncation error at first decreases as $h^3$ . The dashed line on the left has a slope of $-1$ showing that in this example the global round-off error increases as the number of steps $N$ . These calculations were made on a computer that had an accuracy of about $8\frac{1}{2}$ significant figures. . . . .	182
3.4.1	Possible cases for the eigenvalues of a $2 \times 2$ real symplectic matrix. . . .	281
3.4.2	Possible eigenvalue configurations for a $4 \times 4$ real symplectic matrix. The mirror image of each configuration is also a possible configuration, and therefore is not shown in order to save space. Various authors have given these configurations various names. Notably, Case 1 is commonly called a <i>Krein quartet</i> . . . . .	282
3.4.3	Eigenvalues of a $2 \times 2$ real symplectic matrix $M$ as a function of $A = \text{tr}(M)$ . . . .	285
3.4.4	Eigenvalues of a $4 \times 4$ real symplectic matrix $M$ as a function of the coefficients $A$ and $B$ in its characteristic polynomial. . . . .	287
3.5.1	Illustration of eigenvalues colliding and then leaving the unit circle to form what is called a Krein quartet. . . . .	296
4.3.1	Schematic depiction of matrix space showing the zero matrix, the identity matrix $I$ , the ray $N(\lambda M)$ , and the unit ball around the identity matrix. . . . .	466
4.4.1	The matrices $R$ and $M$ are connected by a path that is both an affine geodesic and is perpendicular to the subspace of symplectic matrices at the point $R$ . . . . .	495
5.4.1	a) The summation points in $m, n$ space for the sum (4.7) indicating that the inner sum is over $m$ followed by a sum over $n$ . b) The summation points for the sum (4.8) illustrating that the points are the same, but the inner sum is now over $n$ followed by a sum over $m$ . . . . .	540
5.8.1	Root diagram showing the root vectors for $su(3)$ . . . . .	562
5.8.2	Fundamental weights $\phi^1$ and $\phi^2$ for $su(3)$ . The root vectors are also shown. . . . .	564
5.8.3	Weight diagram for the representation $1 = \Gamma(0, 0)$ . . . . .	566
5.8.4	Weight diagram for the representation $3 = \Gamma(1, 0)$ . . . . .	567
5.8.5	Weight diagram for the representation $\bar{3} = \Gamma(0, 1)$ . . . . .	567
5.8.6	Weight diagram for the representation $6 = \Gamma(2, 0)$ . . . . .	568



5.8.7	Weight diagram for the representation $\bar{6} = \Gamma(0, 2)$ . . . . .	568
5.8.8	Weight diagram for the adjoint representation $8 = \Gamma(1, 1)$ . The 6 weights at the hexagonal vertices lie at the tips of the root vectors $\pm\alpha$ , $\pm\beta$ , $\pm\gamma$ shown in Figure 8.1. The highest weight lies at the tip of the vector $\alpha$ . There are two eigenvectors corresponding to the weight at the origin. . . . .	569
5.8.9	General form of the weight diagram for the representation $\Gamma(m, n)$ . Shown here is the case $(m, n) = (7, 3)$ . All eigenvectors $ \mathbf{w}\rangle$ corresponding to weights $\mathbf{w}$ on a given layer have the same multiplicity. Those corresponding to sites on the boundary have multiplicity 1. Those corresponding to sites on the next two layers have multiplicities 2 and 3, respectively. Those corresponding to sites on the two triangular layers have multiplicity 4. . . . .	570
5.9.1	Stability diagram for $Sp(2, \mathbb{R})$ showing the quantity $r_{\max}$ as a function of $\beta_0$ . All elements with $r < r_{\max}$ are stable, and all elements with $r > r_{\max}$ are unstable. That is, the shaded regions are stable, and the unshaded regions are unstable. In accord with toroidal topology, corresponding points on the dashed lines at the top and bottom of the figure ( $\beta_0 = \pm\pi$ ) are to be identified. . . . .	593
6.1.1	The map $\mathcal{M}$ sends $z$ to $\bar{z}(z, t)$ . . . . .	664
6.1.2	The action of a symplectic map $\mathcal{M}$ on phase space. The general point $z^0$ is mapped to the point $\bar{z}^0$ , and the small vectors $dz$ and $\delta z$ are mapped to the small vectors $d\bar{z}$ and $\delta\bar{z}$ . The figure is only schematic since in general phase space has a large number of dimensions. . . . .	666
6.4.1	A trajectory in augmented phase space. Under the Hamiltonian flow specified by a Hamiltonian $H$ , the general phase-space point $z^i$ is mapped into the phase-space point $z^f$ . The mapping $\mathcal{M}$ is symplectic for any Hamiltonian. . . . .	688
6.4.2	The symplectic map family $\mathcal{N}(t)$ in augmented symplectic map space. . . . .	690
6.5.1	A trajectory of $H(\zeta, t)$ in the augmented $\xi, \eta, t$ phase space having initial coordinates $q$ and final momenta $P$ . . . . .	714
6.7.1	A trajectory of $H^g(\zeta, \tau)$ in the augmented $(\zeta, t) = (\xi, \eta; t)$ phase space. Given a Darboux matrix $\alpha$ , an initial time $t^i$ , a final time $t$ , and the $2n$ -vector $u$ , the initial condition $\zeta(t^i) = z$ is to be selected such that $C^\alpha Z + D^\alpha z = u$ where $\zeta(t) = Z$ . . . . .	757
6.8.1	An <i>ordinary</i> camel and needle in $R^3$ . . . . .	791
6.8.2	The domain $\Gamma_2$ in $\alpha, \beta$ space. Also shown is its subdivision into rectangles of sides $d\alpha$ , $d\beta$ and its boundary $\Gamma_1$ . . . . .	795
6.8.3	The closed paths $C^i$ and $C^f$ in augmented phase space and the trajectories that join them. . . . .	801

6.8.4	The $t, \tau$ parameter space. The left and right boundaries are the curves $t^i(\tau)$ and $t^f(\tau)$ , and their augmented phase-space images are the paths $C^i$ and $C^f$ . Also shown as dashed lines are pairs of parameter-space paths traversed in opposite directions whose images are augmented phase-space trajectories traversed in opposite directions. Note that the lines $\tau = 0$ and $\tau = 1$ have the same image in augmented phase space. . . . .	803
6.8.5	Two adjacent loops in parameter space. . . . .	803
6.8.6	The loops in augmented phase space corresponding to the two parameter-space loops of Figure 8.4. Note that the long sides of the loops are trajectories for the Hamiltonian $H$ , and the short sides are pieces of $C^i$ and $C^f$ . . . . .	804
6.8.7	The integral over a loop is the sum of integrals over top and bottom halves. . . . .	804
6.8.8	The integral over a half loop is the integral over a trajectory of $H$ or its reverse plus the change in the integral resulting from deforming this path. . . . .	804
6.8.9	Initial phase-space distribution for Exercise 8.1. . . . .	806
6.9.1	Two surfaces of section in augmented phase space. Trajectories leaving $S^g$ are assumed to eventually enter and cross $S^h$ , perhaps at different times. . . . .	809
8.3.1	The composite action of two maps $\mathcal{M}_f$ and $\mathcal{M}_g$ . . . . .	880
8.3.2	Successive passage of a trajectory with initial condition $z$ through beam line elements $f$ and $g$ resulting in the intermediate condition $\bar{z}$ and final condition $\bar{\bar{z}}$ . . . . .	880
8.6.1	Various possibilities for the representation of maps in the operation of concatenation. . . . .	901
8.6.2	Product of a map in Lie form with a map in Taylor form. . . . .	903
9.4.1	Concatenation of origin-preserving maps in an enlarged phase space to find equivalent results for maps, including translations, in the original phase space. The concatenator depicted at the top of the figure works with the usual phase space. When translations are taken into account, it involves the use of complicated feed-down formulae as illustrated in Section 9.3. The concatenator at the bottom of the figure works in an enlarged phase space, and employs the far-simpler concatenation rules for origin preserving maps. . . . .	970
9.4.2	A recursive step that takes a map ${}^{r-1}\hat{\mathcal{N}}_{\hat{h}}$ and a pair of indices $\ell(r)$ and $m(r)$ as input, and produces a map ${}^r\hat{\mathcal{N}}_{\hat{h}}$ and polynomial $\tilde{h}_{\ell}^m$ as output. . . . .	978
14.3.1	Top view of symmetric design orbit in a rectangular bend magnet showing <i>local</i> Cartesian coordinates attached to the design orbit. See also Figure 1.6.2 where <i>global</i> Cartesian coordinates are displayed. . . . .	1235
15.10.1	A normal monopole doublet consisting of two magnetic monopoles of equal and opposite sign placed on the $y$ axis and centered on the origin. Also shown, for future reference, is a cylinder with circular cross section placed in the interior field. . . . .	1336

15.10.2	The interior field of a normal monopole doublet in the $z = 0$ plane. Also shown is an ellipse whose purpose will become clear in Sections 17.4 and 19.2. . . . .	1337
15.10.3	The on-axis field component $B_y(x = 0, y = 0, z)$ for the normal monopole doublet in the case that $a = 2.5$ cm and $g = 1$ Tesla-(cm) <sup>2</sup> . The coordinate $z$ is given in centimeters. . . . .	1337
15.10.4	The field component $B_x$ on the line $\rho = 1/2$ cm, $\phi = \pi/4$ , $z \in [-\infty, \infty]$ for the normal monopole doublet in the case that $a = 2.5$ cm and $g = 1$ Tesla-(cm) <sup>2</sup> . In Cartesian coordinates, this is the line $x = y \simeq .353$ cm, $z \in [-\infty, \infty]$ . The coordinate $z$ is given in centimeters. . . . .	1338
15.10.5	The field component $B_z$ on the line $\rho = 1/2$ cm, $\phi = \pi/4$ , $z \in [-\infty, \infty]$ for the normal monopole doublet in the case that $a = 2.5$ cm and $g = 1$ Tesla-(cm) <sup>2</sup> . In Cartesian coordinates, this is the line $x = y \simeq .353$ cm, $z \in [-\infty, \infty]$ . The coordinate $z$ is given in centimeters. . . . .	1339
15.10.6	The quantity $B_\rho(R, \phi, z = 0)$ for the normal monopole doublet in the case that $R = 2$ cm, $a = 2.5$ cm, and $g = 1$ Tesla-(cm) <sup>2</sup> . . . . .	1339
15.10.7	The quantity $B_\rho(R, \phi = \pi/2, z)$ for the normal monopole doublet in the case that $R = 2$ cm, $a = 2.5$ cm, and $g = 1$ Tesla-(cm) <sup>2</sup> . The coordinate $z$ is given in centimeters. . . . .	1340
15.10.8	The on-axis gradient function $C_{1,s}^{[0]}$ for the normal monopole doublet in the case that $a = 2.5$ cm and $g = 1$ Tesla-(cm) <sup>2</sup> . . . . .	1345
15.10.9	The on-axis gradient function $C_{1,s}^{[6]}$ for the normal monopole doublet in the case that $a = 2.5$ cm and $g = 1$ Tesla-(cm) <sup>2</sup> . . . . .	1346
15.10.10	An enlargement of a portion of Figure 10.9 showing a zero hidden in a tail. . . . .	1346
15.10.11	The on-axis gradient function $C_{3,s}^{[0]}$ for the normal monopole doublet in the case that $a = 2.5$ cm and $g = 1$ Tesla-(cm) <sup>2</sup> . . . . .	1347
15.10.12	The on-axis gradient function $C_{3,s}^{[4]}$ for the normal monopole doublet in the case that $a = 2.5$ cm and $g = 1$ Tesla-(cm) <sup>2</sup> . . . . .	1347
15.10.13	The on-axis gradient function $C_{5,s}^{[0]}$ for the normal monopole doublet in the case that $a = 2.5$ cm and $g = 1$ Tesla-(cm) <sup>2</sup> . . . . .	1348
15.10.14	The on-axis gradient function $C_{5,s}^{[2]}$ for the normal monopole doublet in the case that $a = 2.5$ cm and $g = 1$ Tesla-(cm) <sup>2</sup> . . . . .	1348
15.10.15	The on-axis gradient function $C_{7,s}^{[0]}$ for the normal monopole doublet in the case that $a = 2.5$ cm and $g = 1$ Tesla-(cm) <sup>2</sup> . . . . .	1349
15.14.1	The approximating delta function (14.10) when $a = .2$ . . . . .	1362
15.14.2	The approximating delta function (14.10) when $a = .02$ . . . . .	1362
15.14.3	The approximating delta function (14.11) when $a = .2$ . . . . .	1362
15.14.4	The approximating delta function (14.11) when $a = .02$ . . . . .	1363
15.14.5	The approximating signum function (14.36) when $a = .2$ . . . . .	1366
15.14.6	The approximating signum function (14.36) when $a = .02$ . . . . .	1366
15.14.7	The approximating bump function (14.63) when $a = .2$ and $L = 1$ . . . . .	1370
15.14.8	The approximating bump function (14.63) when $a = .02$ and $L = 1$ . . . . .	1370
16.2.1	Coordinate system for a solenoid. . . . .	1397

16.2.2	The approximating signum function (2.26) when $a = .2$ . . . . .	1399
16.2.3	The approximating signum function (2.26) when $a = .02$ . . . . .	1400
16.2.4	The soft-edge bump function (2.17) when $a = .2$ and $L = 1$ . . . . .	1401
16.2.5	The soft-edge bump function (2.17) when $a = .02$ and $L = 1$ . . . . .	1401
16.2.6	The function $\text{bump}''$ when $a = .2$ and $L = 1$ . . . . .	1404
16.2.7	The function $\text{bump}''$ when $a = .02$ and $L = 1$ . . . . .	1404
16.3.1	Coils and cylinders: Part $c$ of this figure shows coils draped like saddles, above and below, over a circular cylinder. Apart from the coil ends, most of the winding runs along straight lines parallel to the cylinder axis. . .	1447
16.3.2	Artist's illustration of coils for the two-in-one 15 meter long dipoles of the CERN Large Hadron Collider. Note that the fringe fields near the dipole ends are <i>not</i> portrayed. . . . .	1448
16.3.3	A winding composed of two oppositely tilted solenoids to form a canted $\cos(\theta)$ dipole. . . . .	1449
16.3.4	The individual and net $C_0^{[1]}(z)$ for a canted $\cos(\theta)$ dipole. . . . .	1450
16.3.5	The on-axis gradient $C_{1,s}^{[0]}(z)$ in Tesla for a canted $\cos(\theta)$ dipole. Also shown is a hard-edge bump function approximation. . . . .	1450
16.3.6	The on-axis gradient $C_{3,s}^{[0]}(z)$ (above) and on-axis gradient $C_{5,s}^{[0]}(z)$ (below) in dimensionless units for a canted $\cos(\theta)$ dipole. They are small for $z \simeq L/2$ , but do not vanish everywhere. Nevertheless their integrated strengths do vanish. . . . .	1451
16.4.1	A net of $n$ coils draped over a cylinder. The $k^{\text{th}}$ coil carries a current $I_k$ . . . . .	1452
16.4.2	Top view of the right ends of the coils shown in Figure 3.7. The $z$ axis comes out of the plane of the paper. . . . .	1453
16.4.3	The approximating signum function (3.21) when $a = .2$ . . . . .	1454
16.4.4	The approximating signum function (3.21) when $a = .02$ . . . . .	1455
16.4.5	The soft-edge bump function given by (3.20) and (3.21) when $a = 0.2$ and $L = 1$ . . . . .	1455
16.4.6	The soft-edge bump function given by (3.20) and (3.21) when $a = 0.02$ and $L = 1$ . . . . .	1456
16.4.7	The approximating signum function (5.29) when $a = .2$ . . . . .	1458
16.4.8	The approximating signum function (5.29) when $a = .02$ . . . . .	1458
16.4.9	The soft-edge bump function given by (5.28) and (5.29) when $a = .2$ and $L = 1$ . . . . .	1459
16.4.10	The soft-edge bump function given by (5.28) and (5.29) when $a = .02$ and $L = 1$ . . . . .	1459
16.6.1	The approximating signum function (5.35) when $r_1 = .2$ and $r_2 = .5$ . . .	1508
16.6.2	The approximating signum function (5.35) when $r_1 = .02$ and $r_2 = .5$ . .	1508
16.6.3	The soft-edge bump function (5.34) when $r_1 = .2$ , $r_2 = .5$ , and $L = 1$ . .	1509
16.6.4	The soft-edge bump function (5.34) when $r_1 = .02$ , $r_2 = .5$ , and $L = 1$ . .	1509
16.6.5	(Place Holder) Derivative of the soft-edge bump function given by (5.28) and (5.29) when $a = .2$ and $L = 1$ , and shown in Figure 5.9. . . . .	1513
16.6.6	(Place Holder) Derivative of the soft-edge bump function given by (5.28) and (5.29) when $a = .02$ and $L = 1$ , and shown in Figure 5.10. . . . .	1513

16.6.7	(Place Holder) Derivative of the soft-edge bump function (5.34) when $r_1 = .2$ , $r_2 = .5$ , and $L = 1$ , and shown in Figure 5.13. . . . .	1513
16.6.8	(Place Holder) Derivative of the soft-edge bump function (5.34) when $r_1 = .02$ , $r_2 = .5$ , and $L = 1$ , and shown in Figure 5.14. . . . .	1514
16.8.1	The ratio $a/L$ as a function of $\theta$ . . . . .	1517
16.9.1	The three-pole wiggler/undulator profile function (4.1) when $a = 0.1$ and $L = 0.5$ . . . . .	1520
16.9.2	The five-pole wiggler/undulator profile function (4.4) when $a = 0.1$ and $L = 0.5$ . . . . .	1520
16.9.3	(Place Holder) The three-pole wiggler/undulator profile function $wig'(3, z, a, L)$ when $a = 0.1$ and $L = 0.5$ . . . . .	1524
17.1.1	Calculation of realistic design trajectory $z^d$ and its associated realistic transfer map $\mathcal{M}$ based on data provided on a 3-dimensional grid for a real beam-line element. Only a few points on the 3-dimensional grid are shown. In this illustration, data from the 3-dimensional grid is interpolated onto the surface of a cylinder with circular cross section, and this surface data is then processed to compute the design trajectory and the transfer map. The use of other surfaces is also possible, and may offer various advantages. . . . .	1533
17.2.1	A circular cylinder of radius $R$ , centered on the $z$ -axis, fitting within the bore of a beam-line element, in this case a wiggler, and extending beyond the fringe-field regions at the ends of the beam-line element. . . . .	1537
17.4.1	An elliptical cylinder, centered on the $z$ -axis, fitting within the bore of a wiggler, and extending beyond the fringe-field regions at the ends of the wiggler. . . . .	1542
17.4.2	Elliptical coordinates showing contours of constant $u$ and constant $v$ . . . . .	1543
17.4.3	A square or rectangular grid in the $x, y$ plane for a fixed $z$ value on the 3-dimensional grid. Values at data points near the ellipse are to be interpolated onto the ellipse. . . . .	1544
17.4.4	The functions $a_0(q)$ through $a_2(q)$ and $b_1(q)$ and $b_2(q)$ for negative values of $q$ . . . . .	1547
17.4.5	An enlargement of a portion of Figure 4.4. For $q$ fixed and slightly negative, the curves, in order of increasing value, are $a_0(q)$ , $a_1(q)$ , $b_1(q)$ , $b_2(q)$ , and $a_2(q)$ . See (4.24) through (4.28). Note that the pair $a_0(q)$ and $a_1(q)$ tends to merge for large negative $q$ , as does the pair $b_1(q)$ and $b_2(q)$ . Similarly, although not shown in this figure, the pair $a_2(q)$ and $a_3(q)$ tends to merge as does the pair $b_3(q)$ and $b_4(q)$ , etc. See (4.29) and (4.30). . . . .	1547

17.4.6	The effective potentials $\lambda(v, q)$ for the $ce_n(v, q)$ in the case $q = -2$ . They are displayed as a function of $v$ , over the interval $[-\pi, \pi]$ , for various $n$ values with $a = a_n(q)$ . The top two curves, which very nearly coincide so as to almost look identical on the scale of the figure, are for the cases $n = 0$ and $n = 1$ . According to Figure 4.5, the curve for $n = 0$ lies just slightly above that for $n = 1$ . The bottom curve is that for $n = 5$ . The curves in between are for $n = 2, 3, 4$ in that order. . . . .	1549
17.4.7	The effective potentials $\lambda(v, q)$ for the $se_n(v, q)$ in the case $q = -2$ . They are displayed as a function of $v$ , over the interval $[-\pi, \pi]$ , for various $n$ values with $a = b_n(q)$ . The top curve is that for $n = 1$ , and the bottom that for $n = 5$ . The curves in between are for $n = 2, 3, 4$ in that order. .	1550
17.4.8	The function $ce_0(v, q)$ as a function of $v$ , over the interval $[-\pi, \pi]$ , for $q = -2$ . High magnification of this figure would reveal that the graph of $ce_0(v, q)$ never touches or crosses, but always lies above, the $v$ axis so that $ce_0(v, q)$ has no zeroes. . . . .	1551
17.4.9	The function $ce_1(v, q)$ as a function of $v$ , over the interval $[-\pi, \pi]$ , for $q = -2$ . . . . .	1551
17.4.10	The function $ce_2(v, q)$ as a function of $v$ , over the interval $[-\pi, \pi]$ , for $q = -2$ . . . . .	1551
17.4.11	The function $se_1(v, q)$ as a function of $v$ , over the interval $[-\pi, \pi]$ , for $q = -2$ . The small dips at $v = \pm\pi/2$ arise from passage through forbidden regions. . . . .	1552
17.4.12	The function $se_2(v, q)$ as a function of $v$ , over the interval $[-\pi, \pi]$ , for $q = -2$ . . . . .	1552
17.4.13	The effective potentials $\lambda(v, q)$ for the $ce_n(v, q)$ in the case $q = -300$ . They are displayed as a function of $v$ , over the interval $[-\pi, \pi]$ , for the $n$ values $n = 0, 1, 2, 3, 4, 5$ with $a = a_n(q)$ . The top two curves, which very nearly coincide so as to almost look identical on the scale of the figure, are for the cases $n = 0$ and $n = 1$ . The next two curves, which also nearly coincide, are for $n = 2$ and $n = 3$ . Finally, the bottom two curves also nearly coincide and are for the cases $n = 4$ and $n = 5$ . As in Figure 4.6, the higher the $n$ value, the lower the curve. . . . .	1553
17.4.14	The effective potentials $\lambda(v, q)$ for the $se_n(v, q)$ in the case $q = -300$ . They are displayed as a function of $v$ , over the interval $[-\pi, \pi]$ , for the $n$ values $n = 1, 2, 3, 4, 5, 6$ with $a = b_n(q)$ . The top two curves, which very nearly coincide so as to almost look identical on the scale of the figure, are for the cases $n = 1$ and $n = 2$ . The next two curves, which also nearly coincide, are for $n = 3$ and $n = 4$ . Finally, the bottom two curves also nearly coincide and are for the cases $n = 5$ and $n = 6$ . As in Figure 4.7, the higher the $n$ value, the lower the curve. . . . .	1554
17.4.15	The function $ce_0(v, q)$ as a function of $v$ , over the interval $[-\pi, \pi]$ , for $q = -300$ . Most of the $v$ axis is forbidden. . . . .	1554
17.4.16	The function $ce_1(v, q)$ as a function of $v$ , over the interval $[-\pi, \pi]$ , for $q = -300$ . Most of the $v$ axis is forbidden. . . . .	1555



17.4.17	The function $ce_2(v, q)$ as a function of $v$ , over the interval $[-\pi, \pi]$ , for $q = -300$ . Most of the $v$ axis is forbidden. . . . .	1555
17.4.18	The function $ce_{22}(v, q)$ as a function of $v$ , over the interval $[-\pi, \pi]$ , for $q = -300$ . For these $q$ and $n$ values all of the $v$ axis is allowed, and the function is fully oscillatory. . . . .	1556
17.4.19	The function $se_1(v, q)$ as a function of $v$ , over the interval $[-\pi, \pi]$ , for $q = -300$ . Most of the $v$ axis is forbidden. . . . .	1556
17.4.20	The function $se_2(v, q)$ as a function of $v$ , over the interval $[-\pi, \pi]$ , for $q = -300$ . Most of the $v$ axis is forbidden. . . . .	1557
17.4.21	The function $se_{23}(v, q)$ as a function of $v$ , over the interval $[-\pi, \pi]$ , for $q = -300$ . For these $q$ and $n$ values all of the $v$ axis is allowed, and the function is fully oscillatory. . . . .	1557
17.4.22	The function $\lambda_{\max}(q)$ for the $n$ values 0 through 5 in the case $a = a_n(q)$ . When $\lambda_{\max}(q) < 0$ , all of the $v$ axis is allowed, and the function $ce_n(v, q)$ is fully oscillatory. When $\lambda_{\max}(q) > 0$ , part of the $v$ axis is forbidden. The higher the $n$ value, the lower the curve. Note that the ‘ $y$ ’ intercepts have the values $-n^2$ in accord with (4.24) through (4.26) and (4.47). The ‘ $x$ ’ intercepts are the values $q_{\text{cr}}(n)$ . Note also that the values of $\lambda_{\max}(q)$ for $n = 0$ and $n = 1$ tend to merge for large negative $q$ , as do the values for $n = 2$ and $n = 3$ , etc. See Figure 4.5 and (4.48). . . . .	1559
17.4.23	The function $\lambda_{\max}(q)$ for the $n$ values 1 through 6 in the case $a = b_n(q)$ . When $\lambda_{\max}(q) < 0$ , all of the $v$ axis is allowed, and the function $se_n(v, q)$ is fully oscillatory. When $\lambda_{\max}(q) > 0$ , part of the $v$ axis is forbidden. The higher the $n$ value, the lower the curve. Note that the ‘ $y$ ’ intercepts have the values $-n^2$ in accord with (4.27), (4.28), and (4.47). The ‘ $x$ ’ intercepts are the values $q_{\text{cr}}(n)$ . Note also that the values of $\lambda_{\max}(q)$ for $n = 1$ and $n = 2$ tend to merge for large negative $q$ , as do the values for $n = 3$ and $n = 4$ , etc. See Figure 4.5 and (4.49). . . . .	1559
17.4.24	The effective potentials $\Lambda(u, q)$ for the $Ce_n(v, q)$ in the case $q = -2$ . They are displayed as a function of $u$ for the $n$ values $n = 0, 1, 2, 3, 4, 5$ with $a = a_n(q)$ . As in Figure 4.6, the curves for $n = 0$ and $n = 1$ nearly coincide. Now, because of the difference in sign between (4.46) and (4.73), the higher the $n$ value the higher the curve. . . . .	1563
17.4.25	The quantities $\Lambda(0, q)$ with $a = a_n(q)$ and $n = 0, 1, 2, 3$ . The higher the $n$ value, the higher the curve. Note that the ‘ $y$ ’ intercepts have the values $n^2$ in agreement with (4.24) through (4.26). Also, values of $\Lambda(0, q)$ for $n = 0$ and $n = 1$ tend to merge for large negative $q$ , as do the values for $n = 2$ and $n = 3$ , etc. See Figure 4.5 and (4.76). . . . .	1563
17.4.26	The quantities $\Lambda(0, q)$ with $a = b_n(q)$ and $n = 1, 2, 3, 4$ . The higher the $n$ value, the higher the curve. Note that the ‘ $y$ ’ intercepts have the values $n^2$ in agreement with (4.27) and (4.28). Also, values of $\Lambda(0, q)$ for $n = 1$ and $n = 2$ tend to merge for large negative $q$ , as do the values for $n = 3$ and $n = 4$ , etc. See Figure 4.5 and (4.77). . . . .	1564

17.4.27	The functions $Ce_0(u, q)$ through $Ce_2(u, q)$ , as a function of $u$ , for $q = -2$ . At $u = 1$ they satisfy the inequalities $Ce_0(1, -2) < Ce_1(1, -2) < Ce_2(1, -2)$ . . . . .	1564
17.4.28	The functions $Se_1(u, q)$ and $Se_2(u, q)$ , as a function of $u$ , for $q = -2$ . At $u = 1$ they satisfy the inequality $Se_1(1, -2) < Se_2(1, -2)$ . . . . .	1565
17.5.1	Hypothetical $B_y^t(x, z)$ data in the interval $x \in [-W/2, W/2]$ and its extension to the full $x$ axis to facilitate Fourier analysis. In this example, $W = 8$ so that $[-W/2, W/2] = [-4, 4]$ . The extension has period $2W = 16$ , is even about the points $x = \pm W/2 = \pm 4$ and their periodic counterparts, and is continuous. Generally, the first derivative is discontinuous at the points $x = \pm W/2 = \pm 4$ and their periodic counterparts. . . . .	1571
18.1.1	The 31-point spline fit associated with $y_{15} = 1$ and all other $y_j = 0$ . Also, $f'(0)$ and $f'(3)$ are set to zero. Note that the fit falls rapidly to zero on either side of $x = 1.5$ . . . . .	1616
18.1.2	The spline fit associated with $f'(x_0) = 1$ , all $y_j = 0$ , and $f'(x_{30}) = 0$ . Note that the fit falls rapidly to zero for $x$ beyond $x_0 = 0$ . Only the results over the interval $x \in [0, 2]$ are displayed. . . . .	1617
18.1.3	The function $f$ and its spline fit $f_{sa}$ for $h = .1$ . They appear identical. . . . .	1619
18.1.4	The difference between the function $f$ and its spline fit $f_{sa}$ for $h = .1$ . Here error = $f(x) - f_{sa}(x)$ . The spline $f_{sa}$ is constructed using the exact values for the end-point derivatives. . . . .	1619
18.1.5	The difference between the function $f$ and its spline fit $f_{sa}$ for $h = .1$ . Here error = $f(x) - f_{sa}(x)$ . The spline $f_{sa}$ is constructed using (1.24) to estimate the end-point derivatives. . . . .	1620
18.2.1	The point $\bar{x}_i, \bar{y}_i$ and its 16 nearest-neighbor grid points. The coordinates of the grid point at the lower left corner are $X_J$ and $Y_K$ . . . . .	1622
18.3.1	The function $f_{-1,1}(z)$ . . . . .	1628
18.3.2	The function $f_{0,2}(z)$ . . . . .	1629
18.3.3	The function $\Re \tilde{f}_{-1,1}(k)$ . . . . .	1629
18.3.4	The function $\Re \tilde{f}_{0,2}(k)$ . . . . .	1630
18.3.5	The function $\Im \tilde{f}_{0,2}(k)$ . . . . .	1630
18.3.6	The exact, discrete, and spline-based Fourier transforms of $f_{-1,1}(z)$ for $h = .10$ . On the scale of this figure the exact and spline-based Fourier transforms are indistinguishable. They are both shown as a solid line. The discrete Fourier transform is shown as a dashed line. Note that it is quasi-periodic while the exact and spline-based Fourier transforms fall to zero for large $ k $ . . . . .	1633
18.3.7	Difference between the exact and discrete Fourier transforms of $f_{-1,1}(z)$ for $h = .10$ . . . . .	1634
18.3.8	Difference between the exact and spline-based Fourier transforms of $f_{-1,1}(z)$ for $h = .10$ . . . . .	1637
18.3.9	Reconstruction of $f_{-1,1} = 1 - z^4$ using forward and inverse discrete Fourier transforms. . . . .	1639



18.3.10	Error in reconstruction of $f_{-1,1} = 1 - z^4$ using forward and inverse discrete Fourier transforms. . . . .	1640
18.3.11	The function $\tilde{f}_{sa}(k)$ (solid line) and its 21-point spline approximation $\tilde{f}_{sasa}(k)$ (dashed line) over the Nyquist band $k \in [-K_{Ny}, K_{Ny}]$ . . . . .	1641
18.3.12	The function $f_{-1,1}(z) = 1 - z^4$ and its reconstruction using the 21-point spline approximation $\tilde{f}_{sasa}(k)$ in (3.41). . . . .	1642
18.3.13	The function $f_{-1,1}(z) = 1 - z^4$ and its reconstruction using, in (3.41), the 51-point spline approximation $\tilde{f}_{sasa}(k)$ over the interval $k \in [-50, 50]$ . . . . .	1643
18.3.14	The difference between the exact function $f_{-1,1}(z) = 1 - z^4$ and its reconstruction using, in (3.41), the 51-point spline approximation $\tilde{f}_{sasa}(k)$ over the interval $k \in [-50, 50]$ . . . . .	1644
19.1.1	The real part of $\tilde{B}_\rho^s(R, 1, k)$ as a function of $k$ for the monopole doublet in the case that $R = 2$ cm and $a = 2.5$ cm. The imaginary part vanishes. . . . .	1656
19.1.2	The real part of $\Re \tilde{B}_\rho^s(R, 7, k)$ as a function of $k$ for the monopole doublet in the case that $R = 2$ cm and $a = 2.5$ cm. The imaginary part vanishes. . . . .	1656
19.1.3	The kernel $[k^{n+m-1}/I'_m(kR)]$ as a function of $k$ in the case that $m = 1$ , $n = 0$ , and $R = 2$ cm. . . . .	1657
19.1.4	The kernel $[k^{n+m-1}/I'_m(kR)]$ as a function of $k$ in the case that $m = 1$ , $n = 6$ , and $R = 2$ cm. . . . .	1657
19.1.5	The kernel $[k^{n+m-1}/I'_m(kR)]$ as a function of $k$ in the case that $m = 7$ , $n = 0$ , and $R = 2$ cm. . . . .	1658
19.1.6	The integrand $(ik)^n \tilde{C}_{m,s}^{[0]}(k)$ for $m = 1$ and $n = 0$ as a function of $k$ in the case that $R = 2$ cm. It is required to compute $C_{1,s}^{[0]}(z)$ . . . . .	1659
19.1.7	The integrand $(ik)^n \tilde{C}_{m,s}^{[0]}(k)$ for $m = 1$ and $n = 6$ as a function of $k$ in the case that $R = 2$ cm. It is required to compute $C_{1,s}^{[6]}(z)$ . . . . .	1659
19.1.8	Exact and numerical results for $C_{1,s}^{[0]}(z)$ . Exact results are shown as a solid line (see Figure 13.7.8), and numerical results are shown as dots. . . . .	1660
19.1.9	Exact and numerical results for $C_{1,s}^{[6]}(z)$ . Exact results are shown as a solid line (see Figure 13.7.9), and numerical results are shown as dots. . . . .	1661
19.1.10	Difference between exact and spline-based numerical results for $C_{1,s}^{[0]}(z)$ using an exact integrand in (14.3.23). . . . .	1661
19.1.11	Difference between exact and spline-based numerical results for $C_{1,s}^{[6]}(z)$ using an exact integrand in (14.3.23). . . . .	1662
19.1.12	Difference between exact and numerical results for $C_{1,s}^{[0]}(z)$ using a spline-based integrand in (14.3.23) and exact values of $B_\rho(R, \phi, z)$ on the cylinder. . . . .	1664
19.1.13	Difference between exact and numerical results for $C_{1,s}^{[6]}(z)$ using a spline-based integrand in (14.3.23) and exact values of $B_\rho(R, \phi, z)$ on the cylinder. . . . .	1665
19.1.14	Difference between exact and completely numerical results for $C_{1,s}^{[0]}(z)$ using a spline-based integrand in (14.3.23) and interpolated values of $B_\rho(R, \phi, z)$ on the cylinder based on field data provided on a grid. . . . .	1666

19.1.15	Difference between exact and completely numerical results for $C_{1,s}^{[6]}(z)$ using a spline-based integrand in (14.3.23) and interpolated values of $B_\rho(R, \phi, z)$ on the cylinder based on field data provided on a grid. . . .	1667
19.1.16	Exact and completely numerical results for $C_{7,s}^{[0]}(z)$ . Exact results are shown as a solid line (see Figure 13.7.15), and numerical results are shown as dots. . . . .	1667
19.1.17	Difference between exact and completely numerical results for $C_{7,s}^{[0]}(z)$ using a spline-based integrand in (14.3.23) and interpolated values of $B_\rho(R, \phi, z)$ on the cylinder based on field data provided on a grid. . . .	1668
19.1.18	The quantity $B_\rho^{\text{Tr}}(R = 2, \phi, z = 0)$ for the monopole doublet in the case that $a = 2.5$ cm and $g = 1$ Tesla-(cm) <sup>2</sup> . . . . .	1669
19.1.19	Difference between $B_\rho(R = 2, \phi, z = 0)$ and $B_\rho^{\text{Tr}}(R = 2, \phi, z = 0)$ for the monopole doublet in the case that $a = 2.5$ cm and $g = 1$ Tesla-(cm) <sup>2</sup> . .	1669
19.1.20	The logarithm base 10 of the quantity $\ \mathbf{B}^{\text{TrA}} - \mathbf{B}^{\text{Exact}}\ /\ \mathbf{B}\ ^{\text{Max}}$ as a function of $\phi$ for three $\rho$ values and $z = 0$ , for the monopole doublet, in the case that $a = 2.5$ cm and $g = 1$ Tesla-(cm) <sup>2</sup> . The solid line corresponds to $\rho = 2$ , the dashed line to $\rho = 1$ , and the dotted line to $\rho = 1/2$ . . . . .	1670
19.1.21	The logarithm base 10 of the quantity $\ \mathbf{B}^{\text{TrA}} - \mathbf{B}^{\text{Exact}}\ /\ \mathbf{B}\ ^{\text{Max}}$ as a function of $\phi$ for three $\rho$ values and $z = 2.5$ , for the monopole doublet, in the case that $a = 2.5$ cm and $g = 1$ Tesla-(cm) <sup>2</sup> . The solid line corresponds to $\rho = 2$ , the dashed line to $\rho = 1$ , and the dotted line to $\rho = 1/2$ . . . . .	1671
19.1.22	The logarithm base 10 of the quantity $\ \mathbf{B}^{\text{TrA}} - \mathbf{B}^{\text{Exact}}\ /\ \mathbf{B}\ ^{\text{Max}}$ as a function of $\phi$ for three $\rho$ values and $z = 5$ , for the monopole doublet, in the case that $a = 2.5$ cm and $g = 1$ Tesla-(cm) <sup>2</sup> . The solid line corresponds to $\rho = 2$ , the dashed line to $\rho = 1$ , and the dotted line to $\rho = 1/2$ . . . . .	1672
19.1.23	The quantities $\log_{10}(2 a_j )$ as a function of $j$ . For large $j$ the points fall on a straight line having slope $\log_{10}(.8)$ . . . . .	1676
19.1.24	The real part of $\tilde{B}_\rho(R = 2, \phi, k = 0)$ for the monopole doublet in the case that $a = 2.5$ cm and $g = 1$ Tesla-(cm) <sup>2</sup> . The imaginary part vanishes. .	1677
19.1.25	The real part of $\tilde{B}_\rho(R = 2, \phi, k = 20)$ for the monopole doublet in the case that $a = 2.5$ cm and $g = 1$ Tesla-(cm) <sup>2</sup> . The imaginary part vanishes.	1677
19.1.26	The quantities $\log_{10}[\ \tilde{\tilde{B}}_\rho(R = 2, n, k = 0)\ ]$ as a function of $n$ . For large $n$ the points fall on a straight line having slope $\log_{10}(.8)$ . . . . .	1678
19.1.27	The quantities $\log_{10}[\ \tilde{\tilde{B}}_\rho(R = 2, n, k = 20)\ ]$ as a function of $n$ . For large $n$ the points fall on a straight line having slope $\log_{10}(.8)$ . . . . .	1678
19.2.1	The real part of $\tilde{F}(v, k = 0)$ for the monopole doublet in the case that $x^{\text{max}} = 4$ cm, $y^{\text{max}} = 2$ cm, $a = 2.5$ cm, and $g = 1$ Tesla-(cm) <sup>2</sup> . The imaginary part vanishes. . . . .	1683
19.2.2	The real part of $\tilde{F}(v, k = 20)$ for the monopole doublet in the case that $x^{\text{max}} = 4$ cm, $y^{\text{max}} = 2$ cm, $a = 2.5$ cm, and $g = 1$ Tesla-(cm) <sup>2</sup> . The imaginary part vanishes. . . . .	1683

- 19.2.3 The real part of  $\tilde{F}(v = \pi/2, k)$  for the monopole doublet in the case that  $x^{\max} = 4$  cm,  $y^{\max} = 2$  cm,  $a = 2.5$  cm, and  $g = 1$  Tesla-(cm)<sup>2</sup>. The imaginary part vanishes. . . . . 1684
- 19.2.4 The real parts of the Mathieu coefficients  $\tilde{F}_r^s(k)$  as a function of  $k$ , with  $r = 1, 3, 5, 7, 9, 11$ , for the monopole doublet in the case that  $x^{\max} = 4$  cm,  $y^{\max} = 2$  cm,  $a = 2.5$  cm, and  $g = 1$  Tesla-(cm)<sup>2</sup>. The imaginary parts vanish. The solid curve, the one with the largest negative excursion at  $k = 0$ , is that for  $r = 1$ . The curves alternate in sign, and the magnitudes of their values at  $k = 0$  decrease, for each successive value of  $r$ . For example, the curve with the largest positive excursion at  $k = 0$  is that for  $r = 3$ . . . . . 1685
- 19.2.5 The real parts of the Mathieu coefficients  $\tilde{F}_r^s(k)$  as a function of  $k$ , with  $r = 17, 19, 21, 23, 25$ , for the monopole doublet in the case that  $x^{\max} = 4$  cm,  $y^{\max} = 2$  cm,  $a = 2.5$  cm, and  $g = 1$  Tesla-(cm)<sup>2</sup>. The imaginary parts vanish. The solid curve, the one with the largest negative excursion at  $k = 0$ , is that for  $r = 17$ . The curves alternate in sign, and the magnitudes of their values at  $k = 0$  decrease for each successive value of  $r$ . For example, the curve with the largest positive excursion at  $k = 0$  is that for  $r = 19$ . . . . . 1686
- 19.2.6 The quantity  $\sqrt{2} \|\tilde{F}\|$  as a function of  $k$  for the monopole doublet in the case that  $x^{\max} = 4$  cm,  $y^{\max} = 2$  cm,  $a = 2.5$  cm, and  $g = 1$  Tesla-(cm)<sup>2</sup>. 1687
- 19.2.7 The kernels  $k^m \beta_m^r(k)/\text{Se}_r'(U, q)$  for the case  $m = 1$  and  $r = 1, 3, 5, 7, 9, 11$ , as a function of  $k$ , with  $q$  and  $k$  related by (2.24) and  $U$  given by (2.1). The kernel for  $r = 1$  is the one with the largest positive value at  $k = 0$ . Kernels for successive values of  $r$  alternate in sign. Their absolute values at  $k = 0$  decrease monotonically with increasing  $r$ . . . . . 1688
- 19.2.8 Absolute values of the kernels  $k^m \beta_m^r(k)/\text{Se}_r'(U, q)$  evaluated at  $k = 0$  for the case  $m = 1$  and  $r \in [1, 15]$  with  $U$  given by (2.1). . . . . 1689
- 19.2.9 The kernels  $k^m \beta_m^r(k)/\text{Se}_r'(U, q)$  for the case  $m = 7$  and  $r = 1, 3, 5$ , as a function of  $k$ , with  $q$  and  $k$  related by (2.24) and  $U$  given by (2.1). The kernel that has the largest positive value is that for  $r = 5$ . The kernel with the next largest positive value is that for  $r = 3$ . The remaining kernel is that for  $r = 1$ . . . . . 1690
- 19.2.10 The kernels  $k^m \beta_m^r(k)/\text{Se}_r'(U, q)$  for the case  $m = 7$  and  $r = 7, 9, 11$ , as a function of  $k$ , with  $q$  and  $k$  related by (2.24) and  $U$  given by (2.1). The kernel for  $r = 7$  is the one with the smallest positive value at  $k = 0$ . Kernels for successive values of  $r$  alternate in sign. Their magnitudes at  $k = 0$  increase monotonically with increasing  $r$  in the range  $r \in [7, 11]$ . . 1691
- 19.2.11 The kernels  $k^m \beta_m^r(k)/\text{Se}_r'(U, q)$  for the case  $m = 7$  and  $r = 13, 15, 17, 19, 21, 23$ , as a function of  $k$ , with  $q$  and  $k$  related by (2.24) and  $U$  given by (2.1). The kernel for  $r = 13$  is the one with the largest negative value at  $k = 0$ . Kernels for successive values of  $r$  alternate in sign. Their magnitudes at  $k = 0$  decrease monotonically with increasing  $r$  in the range  $r \in [13, 23]$ . 1692

19.2.12	Absolute values of the kernels $k^m \beta_m^r(k)/\text{Se}'_r(U, q)$ evaluated at $k = 0$ for the case $m = 7$ and $r \in [7, 37]$ with $U$ given by (2.1). . . . .	1692
19.2.13	The real parts of $(1/2)^m(1/m!)k^m G_{m,s}(k)$ for the monopole doublet when $m = 1, 3, 5, 7$ . The imaginary parts vanish. The quantities decrease in magnitude with increasing $m$ . For example, the curve with the largest negative value at $k = 0$ is that for $m = 1$ . . . . .	1693
19.2.14	The real part of $(1/2)^m(1/m!)k^m G_{m,s}(k)$ for $m = 3$ . . . . .	1694
19.2.15	The real part of $(1/2)^m(1/m!)k^m G_{m,s}(k)$ for $m = 5$ . . . . .	1694
19.2.16	The real part of $(1/2)^m(1/m!)k^m G_{m,s}(k)$ for $m = 7$ . . . . .	1695
19.2.17	The real part of the last retained term in the sum for $(1/2)^m(1/m!)k^m G_{m,s}(k)$ with $m = 1$ based on truncating the series (14.4.84) beyond $r = r_{\max}(1) = 11$ . The imaginary part vanishes. . . . .	1696
19.2.18	The real part of the last retained term in the sum for $(1/2)^m(1/m!)k^m G_{m,s}(k)$ with $m = 3$ based on truncating the series (14.4.84) beyond $r = r_{\max}(3) = 19$ . The imaginary part vanishes. . . . .	1697
19.2.19	The real part of the last retained term in the sum for $(1/2)^m(1/m!)k^m G_{m,s}(k)$ with $m = 5$ based on truncating the series (14.4.84) beyond $r = r_{\max}(5) = 25$ . The imaginary part vanishes. . . . .	1698
19.2.20	The real part of the last retained term in the sum for $(1/2)^m(1/m!)k^m G_{m,s}(k)$ with $m = 7$ based on truncating the series (14.4.84) beyond $r = r_{\max}(7) = 29$ . The imaginary part vanishes. . . . .	1699
19.2.21	Real part of actual truncation error in $(1/2)^m(1/m!)k^m G_{m,s}(k)$ for $m = 1$ produced by truncating the series (14.4.84) beyond $r = r_{\max}(1) = 11$ . The imaginary part vanishes. . . . .	1700
19.2.22	Real part of actual truncation error in $(1/2)^m(1/m!)k^m G_{m,s}(k)$ for $m = 3$ produced by truncating the series (14.4.84) beyond $r = r_{\max}(3) = 19$ . The imaginary part vanishes. . . . .	1701
19.2.23	Real part of actual truncation error in $(1/2)^m(1/m!)k^m G_{m,s}(k)$ for $m = 5$ produced by truncating the series (14.4.84) beyond $r = r_{\max}(5) = 25$ . The imaginary part vanishes. . . . .	1702
19.2.24	Real part of actual truncation error in $(1/2)^m(1/m!)k^m G_{m,s}(k)$ for $m = 7$ produced by truncating the series (14.4.84) beyond $r = r_{\max}(7) = 29$ . The imaginary part vanishes. . . . .	1703
19.2.25	Difference between exact and completely numerically computed results for $C_{1,s}^{[0]}(z)$ based on field data provided on a grid and interpolated onto an elliptic cylinder with $x_{\max} = 4$ cm and $y_{\max} = 2$ cm. . . . .	1706
19.2.26	Difference between exact and completely numerically computed results for $C_{1,s}^{[6]}(z)$ based on field data provided on a grid and interpolated onto an elliptic cylinder with $x_{\max} = 4$ cm and $y_{\max} = 2$ cm. . . . .	1707
19.2.27	Difference between exact and completely numerically computed results for $C_{7,s}^{[0]}(z)$ based on field data provided on a grid and interpolated onto an elliptic cylinder with $x_{\max} = 4$ cm and $y_{\max} = 2$ cm.. . . .	1708
19.2.28	The quantity $F(U, v, z = 0)$ for the monopole doublet in the case that $x^{\max} = 4$ cm, $y^{\max} = 2$ cm, $a = 2.5$ cm, and $g = 1$ Tesla-(cm) <sup>2</sup> . . . . .	1711

19.2.29	Real part of ${}^\infty\tilde{F}_{29}^s(k)$ . The imaginary part vanishes. . . . .	1714
19.2.30	The base 10 logarithm of three quantities. The quantity $\log_{10}[\sqrt{2} \tilde{F}(\pi/2, k) ]$ is the top curve. The middle curve is the quantity $\log_{10}[\sqrt{2} \tilde{F} ]$ , and the bottom curve is $\log_{10}[-{}^\infty\tilde{F}_{29}^s(k)]$ . Together they illustrate the inequalities (2.32) and (2.35). . . . .	1714
19.2.31	Real part of the error quantity ${}^N\tilde{F}_{29}^s(k) - {}^\infty\tilde{F}_{29}^s(k)$ for $N = 40$ . The imaginary part vanishes. . . . .	1715
19.2.32	Real part of the error quantity ${}^N\tilde{F}_{29}^s(k) - {}^\infty\tilde{F}_{29}^s(k)$ for $N = 80$ . The imaginary part vanishes. . . . .	1715
19.2.33	Real part of the error quantity ${}^N\tilde{F}_{29}^s(k) - {}^\infty\tilde{F}_{29}^s(k)$ for $N = 120$ . The imaginary part vanishes. . . . .	1716
20.1.1	The spatial kernels $L_1^{[0]}(\Delta)$ through $L_3^{[0]}(\Delta)$ . For $\Delta = 0$ , the kernels $L_m^{[0]}(\Delta)$ decrease with increasing $m$ . . . . .	1723
20.1.2	The spatial kernels $L_1^{[n]}(\Delta)$ for $n = 0, 2, 4$ . Note that they satisfy (1.16). In particular, they have $n$ zeroes. . . . .	1723
20.1.3	The <i>scaled</i> spatial kernels $L_1^{[0]}(\Delta)$ through $L_3^{[0]}(\Delta)$ , all normalized to 1 at $\Delta = 0$ . The scaled $L_m^{[0]}$ become ever narrower with increasing $m$ . . . . .	1724
20.1.4	The integrands $\tilde{L}_m^{[0]}(\lambda)$ for $m = 1, 2, 3$ . For $\lambda = 0$ , the integrands decrease with increasing $m$ . . . . .	1724
20.1.5	The <i>scaled</i> integrands $\tilde{L}_m^{[0]}(\lambda)$ for $m = 1, 2, 3$ , all normalized to 1 at $\lambda = 0$ . The scaled integrands become ever broader with increasing $m$ . . . . .	1725
20.2.1	The function $B_\rho(R, \phi, z = 0)$ produced by a pure noise field. . . . .	1727
20.2.2	The function $B_\rho(R, \phi, z = 0)$ produced by a pure noise field arising from a second different random number seed. . . . .	1728
20.2.3	The function $B_\rho(R, \phi = \pi/2, z)$ produced by a pure noise field. . . . .	1729
20.2.4	The function $B_\rho(R, \phi = \pi/2, z)$ produced by a pure noise field arising from a second different random number seed. . . . .	1730
20.2.5	Real part of $\tilde{B}_\rho^s(R, m = 1, k)$ produced by a pure noise field. The imaginary part is comparable. . . . .	1731
20.2.6	Real part of $\tilde{B}_\rho(R, m = 1, k)$ produced by a pure noise field arising from a second different random number seed. The imaginary part is comparable. . . . .	1732
20.2.7	The product of $\Re\tilde{B}_\rho(R, m = 1, k)$ for the first random number seed and the kernel of Figure 16.1.3. . . . .	1733
20.2.8	The product of $\Re\tilde{B}_\rho(R, m = 1, k)$ for the second different random number seed and the kernel of Figure 16.1.3. . . . .	1734
20.2.9	The function $C_{1,s}^{[0]}(z)$ produced by a pure noise field. . . . .	1734
20.2.10	The function $C_{1,s}^{[0]}(z)$ produced by a pure noise field arising from a second different random number seed. . . . .	1735
20.2.11	The function $C_{1,s}^{[6]}(z)$ produced by a pure noise field. . . . .	1736
20.2.12	The function $C_{1,s}^{[6]}(z)$ produced by a pure noise field arising from a second different random number seed. . . . .	1736
20.2.13	The function $C_{7,s}^{[0]}(z)$ produced by a pure noise field. . . . .	1737

20.2.14	The function $C_{7,s}^{[0]}(z)$ produced by a pure noise field arising from a second different random number seed. . . . .	1737
20.2.15	The functions $C_{1,s}^{[0]}(z)$ produced by a pure noise field on circular cylinders having $R = 1$ (solid line) and $R = 2$ (dashed line). . . . .	1739
20.2.16	The functions $C_{1,s}^{[0]}(z)$ produced by a pure noise field on circular cylinders having $R = 1$ (solid line) and $R = 2$ (dashed line) and arising from a second different random number seed. . . . .	1739
20.2.17	The functions $C_{1,s}^{[6]}(z)$ produced by a pure noise field on circular cylinders having $R = 1$ (solid line) and $R = 2$ (dashed line). . . . .	1740
20.2.18	The functions $C_{1,s}^{[6]}(z)$ produced by a pure noise field on circular cylinders having $R = 1$ (solid line) and $R = 2$ (dashed line) and arising from a second different random number seed. . . . .	1740
20.2.19	The functions $C_{7,s}^{[0]}(z)$ produced by a pure noise field on circular cylinders having $R = 1$ (solid line) and $R = 2$ (dashed line). . . . .	1741
20.2.20	The functions $C_{7,s}^{[0]}(z)$ produced by a pure noise field on circular cylinders having $R = 1$ (solid line) and $R = 2$ (dashed line) and arising from a second different random number seed. . . . .	1741
20.2.21	The functions $C_{1,s}^{[0]}(z)$ produced by nearly the same pure noise fields on circular cylinders having $R = 1$ (solid line) and $R = 2$ (dashed line). . .	1742
20.3.1	The function $F(U, v, z = 0)$ produced by a pure noise field. . . . .	1743
20.3.2	The function $F(U, v, z = 0)$ produced by a pure noise field arising from a second different random number seed. . . . .	1744
20.3.3	The function $F(U, v = \pi/2, z)$ produced by a pure noise field. . . . .	1745
20.3.4	The function $F(U, v = \pi/2, z)$ produced by a pure noise field arising from a second different random number seed. . . . .	1746
20.3.5	Real part of $\tilde{F}(v = \pi/2, k)$ produced by a pure noise field. The imaginary part is comparable. . . . .	1747
20.3.6	Real part of $\tilde{F}(v = \pi/2, k)$ produced by a pure noise field arising from a second different random number seed. The imaginary part is comparable. . . . .	1748
20.3.7	Real parts of the first few functions $\tilde{F}_r^s(k)$ , those for $r = 1, 3$ , and $5$ , produced by a pure noise field. The imaginary parts are comparable. . .	1749
20.3.8	Real parts of the first few functions $\tilde{F}_r^s(k)$ , those for $r = 1, 3$ , and $5$ , produced by a pure noise field arising from a second different random number seed. The imaginary parts are comparable. . . . .	1750
20.3.9	Real part of $kG_{1,s}(k)$ computed from $\tilde{F}_r^s(k)$ associated with the first seed. The imaginary part is comparable. . . . .	1750
20.3.10	Real part of $kG_{1,s}(k)$ computed from $\tilde{F}_r^s(k)$ associated with the second seed. The imaginary part is comparable. . . . .	1751
20.3.11	A comparison of the circular cylinder $m = 1$ kernel $[1/I_1'(kR)]$ , shown as a solid line, and the first few relevant elliptical cylinder $m = 1$ kernels $[k\beta_1^r(k)/Se'_r(U, q)]$ , namely those for $r = 1, 3, 5, 7, 9$ , and $11$ , shown as a dashed lines. The elliptic kernels alternate in sign, and their magnitude at $k = 0$ decreases with increasing $r$ . See Figure 16.2.7. . . . .	1752



20.3.12	A comparison of the circular cylinder $m = 1$ kernel $[1/I_1'(kR)]$ and the first few elliptic cylinder $m = 1$ kernels $[k\beta_1^r(k)/Se_r'(U, q)]$ , all normalized to 1 at $k = 0$ . . . . .	1753
20.3.13	Dashed line: The function $C_{1,s}^{[0]}(z)$ produced by a pure noise field and using an elliptic cylinder. Solid line: The function $C_{1,s}^{[0]}(z)$ produced by a pure noise field and using a circular cylinder. . . . .	1754
20.3.14	Results for the second random number seed. Dashed line: The function $C_{1,s}^{[0]}(z)$ produced by a pure noise field and using an elliptic cylinder. Solid line: The function $C_{1,s}^{[0]}(z)$ produced by a pure noise field and using a circular cylinder. . . . .	1754
20.3.15	The function $C_{1,s}^{[6]}(z)$ produced by a pure noise field. Dashed line: Elliptic cylinder result. Solid line: Circular cylinder result. . . . .	1755
20.3.16	The function $C_{1,s}^{[6]}(z)$ produced by a pure noise field arising from a second different random number seed. Dashed line: Elliptic cylinder result. Solid line: Circular cylinder result. . . . .	1755
20.3.17	The function $C_{7,s}^{[0]}(z)$ produced by a pure noise field. Dashed line: Elliptic cylinder result. Solid line: Circular cylinder result. . . . .	1756
20.3.18	The function $C_{7,s}^{[0]}(z)$ produced by a pure noise field arising from a second different random number seed. Dashed line: Elliptic cylinder result. Solid line: Circular cylinder result. . . . .	1756
20.3.19	A comparison of the circular cylinder $m = 1$ kernel $[1/I_1'(kR)]$ , shown as a solid line, and the first few relevant elliptical cylinder $m = 1$ kernels $[k\alpha_1^r(k)/Ce_r'(U, q)]$ , namely those for $r = 1, 3, 5, 7, 9$ , and $11$ , shown as a dashed lines. The elliptic kernels alternate in sign, and their magnitude at $k = 0$ decreases with increasing $r$ . . . . .	1757
20.3.20	A comparison of the circular cylinder $m = 1$ kernel $[1/I_1'(kR)]$ and the first few elliptic cylinder $m = 1$ kernels $[k\alpha_1^r(k)/Ce_r'(U, q)]$ , all normalized to 1 at $k = 0$ . . . . .	1758
20.3.21	Dashed line: The function $C_{1,c}^{[0]}(z)$ produced by a pure noise field and using an elliptic cylinder. Solid line: The function $C_{1,c}^{[0]}(z)$ produced by a pure noise field and using a circular cylinder. . . . .	1758
20.3.22	Results for the second random number seed. Dashed line: The function $C_{1,c}^{[0]}(z)$ produced by a pure noise field and using an elliptic cylinder. Solid line: The function $C_{1,c}^{[0]}(z)$ produced by a pure noise field and using a circular cylinder. . . . .	1759
20.3.23	The function $C_{1,c}^{[6]}(z)$ produced by a pure noise field. Dashed line: Elliptic cylinder result. Solid line: Circular cylinder result. . . . .	1759
20.3.24	The function $C_{1,c}^{[6]}(z)$ produced by a pure noise field arising from a second different random number seed. Dashed line: Elliptic cylinder result. Solid line: Circular cylinder result. . . . .	1760
20.3.25	The function $C_{7,c}^{[0]}(z)$ produced by a pure noise field. Dashed line: Elliptic cylinder result. Solid line: Circular cylinder result. . . . .	1760

20.3.26	The function $C_{7,c}^{[0]}(z)$ produced by a pure noise field arising from a second different random number seed. Dashed line: Elliptic cylinder result. Solid line: Circular cylinder result. . . . .	1761
20.3.27	The functions $C_{1,c}^{[0]}(z)$ produced by pure noise fields generated by 12 seeds using data on a circular cylinder. Broken lines: Results from individual seeds. Solid line: Averaged results. . . . .	1762
20.3.28	The functions $C_{1,c}^{[0]}(z)$ produced by pure noise fields generated by 12 seeds using data on an elliptical cylinder. Broken lines: Results from individual seeds. Solid line: Averaged results. . . . .	1762
20.3.29	The functions $C_{1,c}^{[6]}(z)$ produced by pure noise fields generated by 12 seeds using data on a circular cylinder. Broken lines: Results from individual seeds. Solid line: Averaged results. . . . .	1763
20.3.30	The functions $C_{1,c}^{[6]}(z)$ produced by pure noise fields generated by 6 seeds using data on an elliptical cylinder. Broken lines: Results from individual seeds. For clarity, in this graphic only results for 6 seeds are shown. Solid line: Averaged results. As in other related figures, results for 12 seeds were used in computing the average. . . . .	1763
20.3.31	The functions $C_{7,c}^{[0]}(z)$ produced by pure noise fields generated by 12 seeds using data on a circular cylinder. Broken lines: Results from individual seeds. Solid line: Averaged results. . . . .	1764
20.3.32	The functions $C_{7,c}^{[0]}(z)$ produced by pure noise fields generated by 12 seeds using data on an elliptical cylinder. Broken lines: Results from individual seeds. Solid line: Averaged results. . . . .	1764
20.3.33	The function $\{< [C_{1,c}^{[0]}(z)]^2 >\}^{1/2}$ produced by 12 pure noise fields. Dashed line: Result from using an elliptic cylinder. Solid line: Result from using a circular cylinder. . . . .	1765
20.3.34	The function $\{< [C_{1,c}^{[6]}(z)]^2 >\}^{1/2}$ produced by 12 pure noise fields. Dashed line: Result from using an elliptic cylinder. Solid line: Result from using a circular cylinder. . . . .	1765
20.3.35	The function $\{< [C_{7,c}^{[0]}(z)]^2 >\}^{1/2}$ produced by 12 pure noise fields. Dashed line: Result from using an elliptic cylinder. Solid line: Result from using a circular cylinder. . . . .	1766
20.3.36	The functions $C_{1,c}^{[0]}(z)$ produced by assigning a non-zero field value to only a single grid point. Dashed line: Result from using an elliptic cylinder. Solid line: Result from using a circular cylinder. . . . .	1766
21.1.1	Schematic of an iron-dominated solenoid with an inter-pole gap $L$ substantially smaller than the bore radius $R$ . . . . .	1776
21.1.2	The profile function $F(z/R, L/R)$ as given by (2.14) in the cases $L/R = 0$ and $L/R = 1/2$ , and the approximate profile function $G(z/R)$ . The two curves that nearly agree are those for $F$ , with the highest curve being that for $F$ when $L/R = 0$ . The third curve is that for $G$ . . . . .	1778
21.3.1	The angle integrated surface data $b_2(R, z)$ . The magnet occupies the interval $z \in [-0.128 \text{ m}, 0.128 \text{ m}]$ . . . . .	1780
21.3.2	The angle integrated surface data $b_6(R, z)$ . . . . .	1780



21.3.3	The function $C_{2,s}^{[0]}(z)$ as calculated numerically from surface data (dots) and analytically (solid line). . . . .	1781
21.3.4	The function $C_{6,s}^{[0]}(z)$ as calculated numerically from surface data (dots) and analytically (solid line). . . . .	1781
21.3.5	The function $C_{2,s}^{[4]}(z)$ as calculated numerically from surface data (dots) and analytically (solid line). . . . .	1782
21.3.6	The function $C_{2,s}^{[4]}(z)$ as calculated numerically from noisy (seed #2) surface data (dots), and analytically (solid line). . . . .	1783
21.3.7	Difference between the solid line and dots of Figure 8.6. . . . .	1783
21.3.8	Real part of the function $\tilde{b}_2(R, k)$ . The imaginary part vanishes. . . . .	1785
21.3.9	Real part of the function $\tilde{\epsilon}_2(k)$ . The imaginary part has similar features. . . . .	1785
21.3.10	Real (solid line) and imaginary part (dashed line) of the Fourier transform of the function $b_2(R, z)\epsilon_2(z)$ . . . . .	1786
21.3.11	The factor $[k^5/I_2'(kR)]$ that appears in the calculation of $C_{2,s}^{[4]}$ . . . . .	1786
21.3.12	A plot of the real part of the product of the two functions of Figures 9.3 and 9.4. The imaginary part has similar features. . . . .	1787
22.1.1	A bent box with straight end legs. . . . .	1791
22.2.1	(Place Holder) A path $L$ from the point $A$ to the point $B$ . Dipoles are laid out and aligned along the path to form a string. . . . .	1796
22.2.2	(Place holder.) A surface $\Sigma$ spanning the two strings $s$ and $s'$ . . . . .	1801
22.2.3	(Place holder.) A straight half-infinite string extending from $\mathbf{r}_A$ to infinity in the direction $\mathbf{m}$ . . . . .	1802
22.2.4	(Place holder.) A straight full infinite string extending from $\mathbf{r}_A$ to infinity in the directions $\pm\mathbf{m}$ . . . . .	1804
23.1.1	(Place holder) A monopole doublet consisting of two magnetic monopoles of equal and opposite sign placed on the $y$ axis and centered on the origin. Also shown are half-infinite Dirac strings extending from the $+g$ monopole along the positive $y$ axis and from the $-g$ monopole along the negative $y$ axis. . . . .	1826
23.1.2	Behavior of $A_x$ on the line $(0, 0, z)$ . The quantity $z$ is in cm. . . . .	1828
23.1.3	Behavior of $A_z$ on the line $(-1/2, 0, z)$ . The quantity $z$ is in cm. . . . .	1829
23.3.1	Design orbit $x(z) = \hat{x}(z)$ . Also shown is a surrounding bent box with straight end legs. It will be employed in Chapter 24. The center curve is the design orbit. The outer curves are the boundary of the surrounding bent box with with straight end legs. For ease of visualization, the seams between the bent box and the straight end legs are also shown. The quantities $x$ and $z$ are in cm. . . . .	1834
23.3.2	(Place holder) The canonical momentum $\hat{p}_x(z)$ on the design orbit. The quantity $z$ is in cm. . . . .	1835
23.3.3	The scaled mechanical momentum $\hat{p}_x^{\text{mech}}(z)$ on the design orbit. The quantity $z$ is in cm. . . . .	1836
23.3.4	The quantity $\hat{x}'(z)$ on the design orbit. The quantity $z$ is in cm. . . . .	1837
23.3.5	The quantity $B_y$ on the design orbit. The quantity $z$ is in cm. . . . .	1838

23.3.6	(Place holder) The quantity $\mathcal{A}_x$ on the design orbit. The quantity $z$ is in cm. . . . .	1839
23.3.7	(Place Holder?) The quantity $\mathcal{A}_z$ on the design orbit. The quantity $z$ is in cm. . . . .	1840
23.4.1	(Place Holder) The orthonormal triad $\mathbf{e}_\xi$ , $\mathbf{e}_\eta$ , $\mathbf{e}_\zeta$ and associated local deviation variables $\xi, \eta, \zeta$ for the entry of the left leg of the bent box with legs. . . . .	1844
24.1.1	Design orbit $x(z)$ and best approximating circular arc with straight-line extensions. The solid line is the design orbit, and the dotted line is the best approximating circular arc with straight-line extensions. The quantities $x$ and $z$ are in cm. . . . .	1850
24.2.1	The quantity $B_n = B_y$ on the upper face, $y = 2$ cm, and directly above the design orbit. The quantity $z$ is in cm. . . . .	1852
24.2.2	The quantity $\psi$ on the upper face, $y = 2$ cm, and directly above the design orbit. The quantity $z$ is in cm. . . . .	1853
24.2.3	The quantity $A_x^{sd}$ on the design orbit. The quantity $z$ is in cm. . . . .	1858
24.2.4	The quantity $A_z^{sd}$ on the design orbit. The quantity $z$ is in cm. . . . .	1859
24.2.5	The relative error $\Delta_y$ on the design orbit. The quantity $z$ is in cm. . . .	1860
24.2.6	Place holder. The quantity $\Delta =  \Delta $ as a function of $\xi$ and $z$ in the vicinity of the design orbit and in the plane $y = 0$ . The quantities $\xi$ , $y$ , and $z$ are in cm. . . . .	1861
24.2.7	Place holder. The quantity $\Delta =  \Delta $ as a function of $\xi$ and $z$ in the vicinity of the design orbit and in the plane $y = 1$ . The quantities $\xi$ , $y$ , and $z$ are in cm . . . . .	1862
27.1.1	Root vectors for $sp(2)$ . . . . .	1877
27.2.1	The fundamental weight $\phi^1$ and the root vectors $\pm\alpha$ for $sp(2)$ . . . . .	1878
27.2.2	Weight diagrams for the $sp(2)$ representations $\Gamma(0)$ , $\Gamma(1)$ , $\Gamma(2)$ , and $\Gamma(3)$ . . . . .	1879
27.4.1	Root diagram showing the root vectors for $sp(4)$ . . . . .	1891
27.5.1	Fundamental weights $\phi^1$ and $\phi^2$ for $sp(4)$ . The root vectors are also shown. . . . .	1895
27.5.2	Weight diagram for the representation $1 = \Gamma(0, 0)$ . . . . .	1896
27.5.3	Weight diagram for the fundamental representation $4 = \Gamma(1, 0)$ . . . . .	1896
27.5.4	Weight diagram for the representation $5 = \Gamma(0, 1)$ . . . . .	1897
27.5.5	Weight diagram for the adjoint representation $10 = \Gamma(2, 0)$ . The circled weight at the origin has multiplicity 2. The other eight weights are located at the tips of the $sp(4)$ root vectors. . . . .	1898
27.5.6	Weight diagram for the representation $16 = \Gamma(1, 1)$ . The circled weights on the inner diamond have multiplicity 2. . . . .	1899
27.5.7	Weight diagram for the representation $14 = \Gamma(0, 2)$ . The circled weight at the origin has multiplicity 2. . . . .	1899
27.7.1	Root diagram showing the root vectors for $sp(6)$ . The 6 tips of the long root vectors $\pm\alpha^1$ , $\pm\beta^1$ , $\pm\gamma^1$ form the vertices of a regular octahedron. These root vectors have length 2. The remaining 12 short root vectors . . .	1911

27.7.2	Top view of $sp(6)$ root vectors of Figure 7.1 showing root vectors of an $sp(4)$ subgroup. Only the $sp(6)$ root vectors in the $\mathbf{e}^1, \mathbf{e}^2$ plane are displayed. For clarity, all others are omitted. The vector $\mathbf{e}^3$ is out of the plane of the paper. . . . .	1912
27.7.3	View against the unit vector $\mathbf{n}$ of the $sp(6)$ root vectors of Figure 7.1 showing root vectors of an $su(3)$ subgroup. Only the $sp(6)$ root vectors in the $\alpha^3, \beta^3, \gamma^3$ plane and the $\mathbf{e}^1, \mathbf{e}^2, \mathbf{e}^3$ axes are displayed. For clarity, all others are omitted. The vector $\mathbf{n}$ is out of the plane of the paper. . .	1913
27.8.1	Fundamental weights $\phi^1, \phi^2$ and $\phi^3$ for $sp(6)$ . The root vectors are also shown. . . . .	1915
27.8.2	Weight diagram for the representation $1 = \Gamma(0, 0, 0)$ . . . . .	1916
27.8.3	Weight diagram for the fundamental representation $6 = \Gamma(1, 0, 0)$ . . . .	1916
27.8.4	Weight diagram for the representation $14 = \Gamma(0, 1, 0)$ . The circled weight at the origin has multiplicity 2. Observe from Figure 7.1 that the 12 other weights are located at the tips $\cdots$ . . . . .	1917
27.8.5	Weight diagram for the adjoint representation $21 = \Gamma(2, 0, 0)$ . The doubly circled weight at the origin has multiplicity 3. The 18 other weights are located at the tips of the $sp(6)$ root vectors. . . . .	1917
29.2.1	The quantity $A(\beta, \omega)$ as a function of $\omega$ (for the case $\beta = 0.1$ ). . . . .	2091
29.2.2	The quantity $\phi(\beta, \omega)$ as a function of $\omega$ (for the case $\beta = 0.1$ ). . . . .	2092
29.2.3	Feigenbaum diagram showing limiting values $q_\infty$ as a function of $\omega$ (when $\beta = 0.1$ and $\epsilon = .15$ ) for the stroboscopic driven damped simple harmonic oscillator map. . . . .	2092
29.2.4	Feigenbaum diagram showing limiting values $p_\infty$ as a function of $\omega$ (when $\beta = 0.1$ and $\epsilon = .15$ ) for the stroboscopic driven damped simple harmonic oscillator map. . . . .	2093
29.2.5	Feigenbaum diagram showing both limiting values $q_\infty$ and $p_\infty$ as a function of $\omega$ (when $\beta = 0.1$ and $\epsilon = .15$ ) for the stroboscopic driven damped simple harmonic oscillator map. . . . .	2093
29.3.1	Feigenbaum diagram showing limiting values $q_\infty$ as a function of $\omega$ (when $\beta = 0.1$ and $\epsilon = .15$ ) for the stroboscopic Duffing map. . . . .	2095
29.3.2	Feigenbaum diagram showing both limiting values $q_\infty$ and $p_\infty$ as a function of $\omega$ (when $\beta = 0.1$ and $\epsilon = .15$ ) for the stroboscopic Duffing map. . . . .	2095
29.4.1	Feigenbaum/bifurcation diagram showing limiting values $q_\infty$ as a function of $\omega$ (when $\beta = 0.1$ and $\epsilon = 1.5$ ) for the stroboscopic Duffing map. Also shown, in red, is the trail of the unstable fixed point. Finally, jumps in the steady-state amplitude are illustrated by vertical dashed lines at $\omega \simeq 1.8$ and $\omega \simeq 2.6$ . . . . .	2097

29.4.2	Feigenbaum/bifurcation diagram showing limiting values of $p_\infty$ as a function of $\omega$ (when $\beta = 0.1$ and $\epsilon = 1.5$ ) for the stroboscopic Duffing map. Also shown, in red, is the trail of the unstable fixed point. Finally, a downward jump in the steady-state value $p_\infty$ at $\omega \simeq 1.8$ is illustrated by a vertical dashed line. There is also an upward jump between the two black curves at $\omega \simeq 2.6$ , but this feature is too small to be easily indicated by a second vertical dashed line. . . . .	2098
29.4.3	Basins of attraction for the two stable fixed points (when $\omega = 2.25$ , $\beta = 0.1$ , and $\epsilon = 1.5$ ) for the stroboscopic Duffing map. Green points are in the basin of the attracting fixed point $w^1$ and red points are in the basin of the attracting fixed point $w^2$ . There is also an unstable fixed point $w^3$ . See Figures 29.6.7 and 29.6.8. . . . .	2100
29.4.4	Stable periodic orbits $q(\tau)$ (when $\omega = 2.25$ , $\beta = 0.1$ , and $\epsilon = 1.5$ ) for the Duffing equation. . . . .	2101
29.4.5	Unstable periodic orbit $q(\tau)$ (when $\omega = 2.25$ , $\beta = 0.1$ , and $\epsilon = 1.5$ ) for the Duffing equation. . . . .	2102
29.5.1	Feigenbaum diagram showing limiting values $q_\infty$ as a function of $\omega$ (when $\beta = 0.1$ and $\epsilon = 2.2$ ) for the stroboscopic Duffing map. It displays that a bubble has now formed at $\omega \approx .8$ . . . . .	2103
29.5.2	Feigenbaum diagram showing limiting values $q_\infty$ as a function of $\omega$ (when $\beta = 0.1$ and $\epsilon = 5.5$ ) for the stroboscopic Duffing map. The first bubble has grown, a second smaller bubble has formed to its left, and the sub-resonant peak between them has saddle-node bifurcated to become the second saddle-node bifurcation. . . . .	2104
29.5.3	Feigenbaum diagram showing both limiting values $q_\infty$ and $p_\infty$ as a function of $\omega$ (when $\beta = 0.1$ and $\epsilon = 5.5$ ) for the stroboscopic Duffing map. . . . .	2104
29.5.4	An enlargement of Figure 5.2 with the addition of red lines indicating the trails of unstable fixed points. . . . .	2105
29.5.5	Transformation of a pitchfork bifurcation into a saddle-node bifurcation due to the inclusion of the symmetry breaking perturbation $0.02q^2$ . Also shown as red lines are the trails of unstable fixed points. Note, however, that the stable-unstable pair of fixed points born at $\omega \approx 1$ self annihilates at $\omega \approx 1.3$ rather than the unstable fixed point annihilating the other stable fixed point as happens in Figure 4.1. . . . .	2106
29.5.6	Stable periodic orbits $q(\tau)$ (when $\omega = 1.1$ , $\beta = 0.1$ , and $\epsilon = 5.5$ ) for the Duffing equation. . . . .	2107
29.5.7	Unstable periodic orbit $q(\tau)$ (when $\omega = 1.1$ , $\beta = 0.1$ , and $\epsilon = 5.5$ ) for the Duffing equation. . . . .	2108
29.6.1	An enlargement of Figure 5.2 showing, for $\mathcal{M}$ , the period-one fixed points in red (two stable and one unstable) and the stable-unstable pairs of period-three fixed points in green. . . . .	2109
29.6.2	A blue-sky bifurcation that produces, and then subsequently destroys, a pair of stable (black) and unstable (red) period-three fixed points. These points correspond to the upper green feature shown in Figure 6.1. . . .	2110

29.6.3	A blue-sky bifurcation that produces, and then subsequently destroys, a pair of stable (black) and unstable (red) period-three fixed points. These points correspond to the center green feature shown in Figure 6.1. . . .	2111
29.6.4	A blue-sky bifurcation that produces, and then subsequently destroys, a pair of stable (black) and unstable (red) period-three fixed points. These points correspond to the bottom green feature shown in Figure 6.1. . .	2112
29.6.5	Basins, using the map $\mathcal{M}^3$ and with $\omega = 4.21$ , for the period-one attracting fixed points $w^1$ (white) and $w^2$ (blue), and the period-three attracting fixed points $z^1$ (red), $z^2$ (green), and $z^3$ (yellow). . . . .	2113
29.6.6	An enlargement of a portion of Figure 6.5. The fixed points $w^1$ and $z^1$ , $z^2$ , and $z^3$ themselves are shown as small black dots. The small black dot at the center of the figure is the fixed point $w^1$ . Three small black dots near the ends of the red, green, and yellow filaments surround $w^1$ . These are the $\mathcal{M}^3$ fixed points $z^1$ , $z^2$ , and $z^3$ , respectively. The principal components of the period-three basins contain the fixed points $z^1$ , $z^2$ , and $z^3$ . Note the crowding of the red, green, and yellow pieces of the period-three basins against the blue basin of $w^2$ (but still separated by ever smaller white areas) thereby making this basin boundary structure fractal. . . . .	2115
29.7.1	The quantity $[\ddot{q} + 2\beta\dot{q}]$ as a function of $\tau$ for the periodic solution when $\omega = .01$ (and $\beta = .1$ and $\epsilon = 5.5$ ). . . . .	2117
29.7.2	The quantity $[2\beta\dot{q} + q + q^3]$ as a function of $\tau$ for the periodic solution when $\omega = 15$ (and $\beta = .1$ and $\epsilon = 5.5$ ). . . . .	2118
29.8.1	Feigenbaum diagram showing limiting values $q_\infty$ as a function of $\omega$ (when $\beta = 0.1$ and $\epsilon = 22.125$ ) for the stroboscopic Duffing map. . . . .	2120
29.8.2	Enlargement of a portion of Figure 8.1 displaying limiting values of $q_\infty$ as a function of $\omega$ (when $\beta = 0.1$ and $\epsilon = 22.125$ ) for the stroboscopic Duffing map. It shows part of the first bubble at the far right, the second bubble, and part of a third bubble at the far left. Examine the first and second bubbles. Each initially consists of two stable period-one fixed points. Each also contains the beginnings of period-doubling cascades. These cascades do not complete, but rather cease and then undo themselves by successive mergings to again result in a pair of stable period-one fixed points. There are also many higher-period fixed points and their associated cascades. . . . .	2122
29.8.3	Feigenbaum diagram showing limiting values $q_\infty$ as a function of $\omega$ (when $\beta = 0.1$ and $\epsilon = 25$ ) for the stroboscopic Duffing map. . . . .	2123
29.8.4	Enlargement of a portion Figure 8.3 showing the first, second, and third bubbles. The period-doubling cascades in each of the first and second bubbles now complete. Then they undo themselves as $\omega$ is further increased. There is no period doubling in the third bubble when $\epsilon = 25$ . . . . .	2124

29.8.5	Detail of part of the first bubble in Figure 8.4 showing upper and lower infinite period-doubling cascades. Part of the trail of the stable fixed point associated with the second saddle-node bifurcation accidentally appears to overlay the upper period doubling bifurcation. Finally, associated with higher-period fixed points, there are numerous cascades and followed by successive mergings. . . . .	2125
29.8.6	Detail of part of the upper cascade in Figure 8.5 showing an infinite period-doubling cascade, followed by chaos, for what was initially a stable period-one fixed point. . . . .	2125
29.9.1	Limiting values of $q_\infty, p_\infty$ for the stroboscopic Duffing map when $\omega = 1.2902$ (and $\beta = .1$ and $\epsilon = 25$ ). They appear to lie on a strange attractor.	2126
29.9.2	Enlargement of boxed portion of Figure 9.1 illustrating the beginning of self-similar fractal structure. . . . .	2127
30.5.1	The isolated fixed point $z^\alpha$ surrounded by a small circle $c$ and the associated vectors $v(z)$ drawn from the common origin $(0,0)$ . . . . .	2162
30.5.2	A closed curve $C$ that surrounds several fixed points, and the curve $C'$ formed by shrinking $C$ . . . . .	2164
30.5.3	The contours $C(E_1)$ (inner) and $C(E_2)$ (outer) for the values $E_1 = 25$ and $E_2 = 100$ . Also shown are the vectors $v(z)$ for selected (and labeled) points $z$ on $C(E_2)$ . Observe that all vectors point inward and terminate on some lesser (inner) energy contour. The Duffing parameters have the values $\omega = 2.25$ , $\beta = .1$ , and $\epsilon = 1.5$ . . . . .	2166
30.5.4	The vectors $v(z)$ of Figure 5.3 labeled and drawn from the common origin $(0,0)$ . As the points $z$ on $C(E_2)$ make one counterclockwise revolution, the vectors $v(z)$ undergo one counterclockwise revolution, thereby indicating that $C(E_2)$ has index $+1$ . . . . .	2167
30.5.5	The basin structure for the complex logistic map when $\gamma = \gamma'_D = -.55268 + .959456i$ . The origin is a repelling fixed point, and the three lobes that meet at the origin each contain one of the three attracting period-three fixed points $z^1$ (red), $z^2$ (green), and $z^3$ (yellow). The action of $\mathcal{M}$ on points near the origin is essentially a counterclockwise rotation about the origin by $120^\circ$ . . . . .	2173
30.6.1	Schematic illustration of the action of $\mathcal{M}$ on points near $z^\alpha$ in the linear approximation. Points on $v_<$ are moved inward toward $z^\alpha$ , and points on $v_>$ are moved outward. Others are moved on hyperbolas. . . . .	2174
30.6.2	The (transverse) intersection of the unstable and stable manifolds emanating from a hyperbolic fixed point resulting in a homoclinic point $K$ . Also displayed is the elliptic fixed point and the behavior of points near the elliptic fixed point. . . . .	2176
30.6.3	Successive homoclinic intersections of the unstable and stable manifolds showing the first few points $\mathcal{M}^n K$ . The other halves of $W_u$ and $W_s$ , those pieces that go off to infinity, are not shown. Also not shown are the elliptic fixed point and the behavior of points near it. . . . .	2177



30.6.4	The regions $\mathcal{R}$ and $\bar{\mathcal{R}}$ . Observe that, in the right panel, the unstable manifold “oscillates” about the stable manifold in the interval between $K$ and $\mathcal{MK}$ . When $\mathcal{M}$ is symplectic, the two small regions produced by this oscillation must have equal areas. . . . .	2178
30.6.5	Successive oscillations of $W_u$ about $W_s$ and of $W_s$ about $W_u$ in the vicinity of the hyperbolic fixed point. The spacing between successive oscillations becomes exponentially finer, and the oscillation amplitude becomes exponentially larger. . . . .	2179
30.6.6	A continuation of Figure 6.5 near the origin (the hyperbolic fixed point) showing the formation of a grid of intersecting lines. The spacing of the grid becomes finer and finer as it approaches the hyperbolic fixed point. Each grid intersection is a homoclinic point. The result of all these intersections is an ever denser cloud of homoclinic points that has the hyperbolic fixed point as a limit point. . . . .	2180
30.6.7	A blow up of part of Figure 23.4.3 illustrating the basins of attraction, the unstable fixed point (23.4.3), and the eigenvector $v_1$ (the one with eigenvalue less than 1) for the stroboscopic Duffing map. The unstable fixed point lies on, and the vector $v_1$ points along, the boundary between the two basins. . . . .	2181
30.6.8	The stable (blue) and unstable (red) manifolds for the unstable fixed point (23.4.3) of the stroboscopic Duffing map. Note that the unstable manifold spirals into the stable fixed points (23.4.1) and (23.4.2), and the stable manifold lies along the basin boundaries. The stable and unstable manifolds do not intersect, so there are no homoclinic points. . . . .	2182
30.7.1	Feigenbaum diagram showing limiting values $q_\infty$ as a function of $a$ (and $b$ held at $b = +.3$ ) for a non-orientation preserving case of the general Hénon map. . . . .	2186
30.7.2	Enlargement of the boxed region in Figure 7.1. The upper cascade is that readily visible in the box in Figure 7.1. The lower cascade, which seems to appear out of nowhere and then terminate abruptly, corresponds to the small speck near the bottom of the box in Figure 7.1. . . . .	2186
30.7.3	Successive enlargements of the attracting set $q_\infty, p_\infty$ for a non-orientation preserving case of the general Hénon map ( $a = 1.4, b = +.3$ ). The attractor appears to be fractal, and therefore strange. . . . .	2188
30.7.4	(Partial) Feigenbaum diagram showing limiting values $q_\infty$ as a function of $a$ (and $b$ held at $b = -.3$ ) for an orientation preserving case of the general Hénon map. . . . .	2189
30.7.5	Full Feigenbaum diagram showing limiting values $q_\infty$ and $p_\infty$ as a function of $a$ (and $b$ held at $b = -.3$ ) for an orientation preserving case of the general Hénon map. . . . .	2190
30.7.6	Successive enlargements of the attracting set $q_\infty, p_\infty$ for an orientation preserving case of the general Hénon map ( $a = 2.11, b = -.3$ ). The attractor appears to be fractal, and therefore strange. . . . .	2191



30.8.1	Values of $q_f^\pm$ , when $b = -.3$ , as a function of $a$ . A horizontal tic mark indicates where $q_f^+$ and $q_f^-$ meet when $a = a_{\min}$ . . . . .	2194
30.8.2	Values of $q_f^\pm$ , when $b = -.9$ , as a function of $a$ . A horizontal tic mark indicates where $q_f^+$ and $q_f^-$ meet when $a = a_{\min}$ . . . . .	2194
30.8.3	Eigenvalues $\lambda$ of $R_h^*$ , when $b = -.3$ and $q_f = q_f^-$ , as a function of $a$ . . .	2196
30.8.4	Eigenvalues $\lambda$ of $R_h^*$ , when $b = -.9$ and $q_f = q_f^-$ , as a function of $a$ . . .	2197
30.8.5	Eigenvalues $\lambda$ of $R_h^*$ , when $b = -.3$ and $q_f = q_f^+$ , as a function of $a$ . Note the small “line” of positive real eigenvalues for $a < 0$ . Its endpoints coincide with the edges of the gap in the curve shown in Figure 8.3. . .	2198
30.8.6	Eigenvalues $\lambda$ of $R_h^*$ , when $b = -.9$ and $q_f = q_f^+$ , as a function of $a$ . Note the barely visible line of positive real eigenvalues for $a < 0$ . Its endpoints coincide with the edges of the tiny gap in the curve shown in Figure 8.4. . .	2198
30.8.7	The parameter $a$ as a function of $\nu$ for various values of $b$ . . . . .	2202
30.8.8	The quantity $q_f$ for the mobile fixed point as a function of $\nu$ in the symplectic case $b = -1$ . . . . .	2204
30.8.9	The quantity $\tau$ as a function of $\nu$ in the symplectic case $b = -1$ . . . . .	2204
30.8.10	The quantity $\tau$ as a function of $\nu$ in the nonsymplectic case $b = -.3$ . . .	2205
30.8.11	The quantity $q_f$ for the mobile fixed point as a function of $\nu$ in the nonsymplectic case $b = -.3$ . . . . .	2205
30.8.12	The quantity $p_f$ for the mobile fixed point as a function of $\nu$ in the nonsymplectic case $b = -.3$ . . . . .	2206
30.8.13	Location of the mobile fixed point for the nonsymplectic case $b = -.3$ and $\nu$ varying over the range $[-20, 20]$ . . . . .	2206
30.8.14	Value of $\cdots$ in the symplectic case $b = -1$ . . . . .	2209
30.8.15	Spectrum of $\tilde{M}_f$ (and of the linear part of $\mathcal{M}_-$ about its second fixed point) for $\nu$ varying over the range $[0, 3]$ in the symplectic case $b = -1$ . An identical picture is produced for $\nu$ varying in the range $[-3, 0]$ as is evident from (8.97) and Figure 8.14. The eigenvalues leave the unit circle at $\nu = \pm 1.763$ as is also evident from (8.97) and Figure 8.14. See Exercise 8.18. . . . .	2209
30.8.16	Phase advance of $\tilde{M}_f$ (and of the linear part of $\mathcal{M}_-$ about its second fixed point) as a function of $\nu$ in the symplectic case $b = -1$ . Only the range $\nu \in [-1.763, 1.763]$ is shown because the eigenvalues leave the unit circle outside this range. . . . .	2210
30.8.17	Value of $\cdots$ in the case $b = -.3$ . . . . .	2210
30.8.18	Spectrum of $\tilde{M}_f$ (and of the linear part of $\mathcal{M}_-$ about its second fixed point) for $\nu$ varying over the range $[0, 3]$ in the nonsymplectic case $b = -.3$ . . . . .	2210
30.8.19	Phase advance of $\tilde{M}_f'$ as a function of $\nu$ in the nonsymplectic case $b = -.3$ . Only the ranges $\nu \in [-1.886, -.839]$ and $\nu \in [.839, 1.886]$ are shown because the eigenvalues of $\tilde{M}_f'$ leave the unit circle for $\nu$ outside these ranges. See Figure 8.17 and Exercise 8.15. . . . .	2211
30.8.20	Maximum value of $\lambda_+$ as a function of $ru$ . . . . .	2211
30.9.1	Stable and unstable manifolds for $\mathcal{M}_-$ and behavior of points near the second fixed point for the case $\Lambda = 3$ . . . . .	2219

30.9.2	Stable and unstable manifolds for $\mathcal{M}_-$ and behavior of points near the second fixed point for the case $\Lambda = 4$ . . . . .	2219
30.12.1	Bifurcation diagram showing limiting values $q_\infty$ as a function of $\omega$ (when $\beta = 0.1$ and $\epsilon = 0.3$ ) for the stroboscopic Duffing map. The trail of the fixed point that is unique and stable for small values of $\omega$ is shown in blue. A pair of fixed points, one stable and one unstable, is born at $\omega = \omega_1 = 1.30305 \dots$ . The trail of the stable fixed point is shown in green and the trail of the unstable fixed point is shown in red. The black dot at the left end of the red trail is the value of $\omega = \omega_1$ at which the pair is born. The blue stable fixed point and the red unstable fixed point annihilate at $\omega = \omega_2 = 1.38386 \dots$ . This point is indicated by the black dot at the right end of the red trail. For larger $\omega$ values only the green fixed point remains. The black dot near the center of the red trail marks the expansion point to be used in preparing Figures 12.4 through 12.6. . . . .	2222
30.12.2	Eigenvalues of $L(2\pi)$ , the linear part of the stroboscopic map (in the variables $z_1$ and $z_2$ ), about the fixed points shown in Figure 12.1. The color coding is that same as in Figure 12.1. . . . .	2223
30.12.3	Eigenvalues of $L(2\pi)$ shown from a different perspective. . . . .	2224
30.12.4	The analog of Figure 12.1 computed using $\mathcal{M}_8$ , an eighth-order approximation to $\mathcal{M}$ including parameter dependence. The black point near the center of the red trail is the point about which the Taylor expansion of the stroboscopic Duffing map is constructed. The black dots near the ends of the red trail are the exact values of the fixed points for the exact values of $\omega_1$ and $\omega_2$ . . . . .	2227
30.12.5	The analog of Figure 12.2 computed using $\mathcal{M}_8$ , an eighth-order approximation to $\mathcal{M}$ including parameter dependence. . . . .	2228
30.12.6	Data of Figure 12.5 shown from a different perspective. . . . .	2229
30.12.7	The analog of Figure 12.1 computed using two eighth-order polynomial maps including parameter dependence. The black dots at the ends of the red trail, located at $\omega_1$ and $\omega_2$ , are the points about which the Taylor expansions of the stroboscopic Duffing map are constructed. . . . .	2231
30.12.8	The analog of Figure 12.2 computed using two eighth-order polynomial maps including parameter dependence. . . . .	2232
30.12.9	Data of Figure 12.8 shown from a different perspective. . . . .	2233
30.12.10	Bifurcation diagram for the Duffing stroboscopic map in the case $\epsilon = 2.5$ (and $\beta = 0.1$ ) for $\omega$ in the vicinity of the first bubble. The trail of the stable fixed point before the pitchfork bifurcation and after the pitchfork merger is shown in black. The trails of the two stable fixed points that exist after the pitchfork bifurcation and before the pitchfork merger are shown in blue and green. The trail of the associated unstable fixed point is shown in red. The black dot at the left end of the red trail is located at $\omega = \omega_1$ . and the black dot at the right end of the red trail is located at $\omega = \omega_2$ . The black dot near the middle of the red trail indicates the value $\omega = \omega_{\text{mid}}$ to be used as an expansion point. . . . .	2235

30.12.11	Eigenvalues of $L(2\pi)$ , the linear part of the stroboscopic map (in the variables $z_1$ and $z_2$ ), about the fixed points shown in Figure 12.10. The color coding is that same as in Figure 12.10. Note two of the curves are colored blue-green because, as explained in the text, there is overlap because of equivariance symmetry. . . . .	2236
30.12.12	Data of Figure 12.11 shown from a different perspective. . . . .	2237
30.12.13	The analog of Figure 12.10 computed using $\mathcal{M}_8$ , an eighth-order approximation to $\mathcal{M}$ including parameter dependence. The black point near the center of the red trail is the point $\omega_{\text{mid}} = .916349$ about which the Taylor expansion of the stroboscopic Duffing map was constructed. The other two black points are located at the exact values of $\omega_1$ and $\omega_2$ . . .	2239
30.12.14	The analog of Figure 12.11 computed using $\mathcal{M}_8$ , an eighth-order approximation to $\mathcal{M}$ including parameter dependence. . . . .	2240
30.12.15	Data of Figure 12.14 shown from a different perspective. . . . .	2241
30.12.16	Detail of part of the period doubling bifurcation shown in Figure 25.8.6. The map $\mathcal{M}$ has one fixed point $z_f$ before period doubling, it is stable, and its trail is shown in black. After period doubling $\mathcal{M}$ still has one fixed point $z_f$ , it is unstable, and its trail is shown in red. These fixed points are, of course, also fixed points of $\mathcal{M}^2$ . After period doubling, $\mathcal{M}^2$ has two additional fixed points whose trails are shown in blue and green. These period-two fixed points are not fixed points of $\mathcal{M}$ . Instead, they are sent into each other under the action of $\mathcal{M}$ . . . . .	2243
30.12.17	Eigenvalues of the linear part of $\mathcal{M}$ in the vicinity of its period-doubling bifurcation. . . . .	2244
30.12.18	Different perspective of the eigenvalues of the linear part of $\mathcal{M}$ in the vicinity of its period-doubling bifurcation. . . . .	2245
30.12.19	Eigenvalues of the linear part of $\mathcal{M}^2$ in the vicinity of the period doubling bifurcation of $\mathcal{M}$ . . . . .	2246
30.12.20	Different perspective of the eigenvalues of the linear part of $\mathcal{M}^2$ in the vicinity of the period doubling bifurcation of $\mathcal{M}$ . . . . .	2247
30.12.21	Bifurcation diagram for the map $\mathcal{M}_3$ , the third-order polynomial approximation to $\mathcal{M}$ (including parameter dependence) expanded about the period-doubling bifurcation point shown in black. The polynomial map has one fixed point $z_f$ before period doubling. It is stable and its trail is shown in black. After period doubling $\mathcal{M}_3$ still has one fixed point $z_f$ . It is unstable and its trail is shown in red. These fixed points are, of course, also fixed points of $(\mathcal{M}_3)^2$ . After period doubling, $(\mathcal{M}_3)^2$ has two additional fixed points whose trails are shown in blue and green. These period-two fixed points are not fixed points of $\mathcal{M}_3$ . Instead, they are sent into each other under the action of $\mathcal{M}_3$ . . . . .	2249
30.12.22	Eigenvalues of the linear part of $(\mathcal{M}_3)^2$ in the vicinity of the period doubling bifurcation of $\mathcal{M}_3$ . . . . .	2250
30.12.23	Different perspective of the eigenvalues of the linear part of $(\mathcal{M}_3)^2$ in the vicinity of the period doubling bifurcation of $\mathcal{M}_3$ . . . . .	2251

30.12.24	Partial Feigenbaum diagram for the map $\mathcal{M}_8$ . The black dot marks the point about which $\mathcal{M}$ is expanded to yield $\mathcal{M}_8$ . . . . .	2253
30.12.25	Full Feigenbaum diagram for the map $\mathcal{M}_8$ . The black dot again marks the expansion point. . . . .	2254
30.12.26	Limiting values of $q_\infty, p_\infty$ for the map $\mathcal{M}_8$ when $\omega = 1.2902$ . They appear to lie on a strange attractor. . . . .	2255
30.12.27	Enlargement of boxed portion of Figure 12.26 illustrating the beginning of self-similar fractal structure. . . . .	2256
30.12.28	Enlargement of boxed portion of Figure 12.27 illustrating the continuation of self-similar fractal structure. . . . .	2257
30.12.29	Enlargement of boxed portion of Figure 12.28 illustrating the further continuation of self-similar fractal structure. . . . .	2258
30.12.30	Partial Feigenbaum diagram for the map $\mathcal{M}_8$ showing a full cascade followed by successive mergings. The black dot marks the point about which $\mathcal{M}$ is now expanded to yield $\mathcal{M}_8$ . . . . .	2260
30.12.31	Full Feigenbaum diagram for the map $\mathcal{M}_8$ showing a full cascade followed by successive mergings. The black dot again marks the point about which $\mathcal{M}$ is expanded to yield $\mathcal{M}_8$ . . . . .	2261
30.12.32	Full Feigenbaum diagram for the exact map $\mathcal{M}$ . See Figure 25.8.4 for a related partial Feigenbaum diagram. The black dot again marks the expansion point used in Figures 12.30 and 12.31. There appears to be a gap around $\omega \approx 1.33$ separating two chaotic regions. Within the right side of the gap (to the right of $\omega \approx 1.335$ ) there are three yellow trails corresponding to a period-three stable orbit. As $\omega$ is decreased, there are pitchfork bifurcations so that each yellow trail splits into two yellow trails. There are then six yellow trails corresponding to two period-three stable orbits. Thus the gap, on the scale shown, is essentially a period-three window. . . . .	2262
30.12.33	Partial Feigenbaum diagram for the map $\mathcal{M}_3$ . The black dot marks the point about which $\mathcal{M}$ is expanded to yield $\mathcal{M}_3$ . . . . .	2263
30.12.34	Limiting values of $q_\infty, p_\infty$ for the map $\mathcal{M}_3$ when $\omega = 1.2902$ . They appear to lie on a strange attractor. . . . .	2264
30.12.35	Enlargement of boxed portion of Figure 12.34 illustrating the beginning of self-similar fractal structure. . . . .	2265
30.12.36	Partial Feigenbaum diagram for the map $\mathcal{M}_5$ . The black dot marks the point about which $\mathcal{M}$ is expanded to yield $\mathcal{M}_5$ . . . . .	2266
30.12.37	Limiting values of $q_\infty, p_\infty$ for the map $\mathcal{M}_5$ when $\omega = 1.2902$ . They appear to lie on a strange attractor. . . . .	2267
30.12.38	Enlargement of boxed portion of Figure 12.37 illustrating the beginning of self-similar fractal structure. . . . .	2268
31.1.1	Decomposition of a set $X$ into disjoint equivalence classes, with a normal form element representative for each equivalence class. . . . .	2278
31.4.1	Four broad possibilities for general maps. . . . .	2281

33.2.1	Normal forms $g_2^N$ and eigenvalue spectrum of associated Hamiltonian matrices in the case of 2-dimensional phase space. The normal forms given in the three columns above are for the cases $\delta < 0$ , $\delta = 0$ , and $\delta > 0$ , respectively. . . . .	2301
33.2.2	Equivalence classes (orbits/leaves) for the space $\mathcal{P}_2$ of second-order polynomials in two variables. They are displayed in terms of the variables $\xi, \eta, \zeta$ . In this figure the $\xi$ axis points upward, the $\eta$ axis points out of the page, and the $\zeta$ axis points to the right. Case <i>a</i> , for which $\delta < 0$ , shows a typical one-sheeted hyperboloid. The point on the equator given by (2.53) and (2.54) corresponds to the normal form $(-\delta)^{1/2}(q^2 - p^2)$ for that value of $\delta$ . Also shown on this diagram are the two cones for $\delta = 0$ . The point on the front of the top cone given by ((2.60) and (2.61) corresponds to the normal form $+q^2$ and the point on the rear of the bottom cone given (2.62) and (2.63) by corresponds to the normal form $-q^2$ . The origin where the cones meet is the single-element equivalence class $g_2 = 0$ . Case <i>b</i> , for which $\delta > 0$ , shows a typical two-sheeted hyperboloid. Also shown is the sphere (2.50) that just kisses the hyperboloid. The two kissing points (the points on the upper and lower sheets that are closest to the origin) correspond to the normal forms $\pm\delta^{1/2}(p^2 + q^2)$ . For simplicity, cases <i>a</i> and <i>b</i> are shown separately. They should actually be superimposed along with many other such hyperboloids to show all the one-sheeted and two-sheeted hyperboloids for all values of $\delta$ . . . . .	2304
33.2.3	Eigenvalues of a $4 \times 4$ real Hamiltonian matrix as a function of the coefficients $C$ and $D$ in its characteristic polynomial. . . . .	2308
33.2.4	Eigenvalues of $B$ as a function of $\epsilon$ when $\omega_1 = 1.5$ and $\omega_2 = -1.6$ . . . .	2323
33.4.1	Curves of constant $\Lambda/\lambda$ and flow directions for the equations of motion (4.13) and (4.14). These curves were made with $\lambda = 1$ , which simply sets the scale for $q$ and $p$ , and $\Lambda = 0, \pm 5$ . . . . .	2328
33.4.2	(Place Holder) Curve on which the map $\mathcal{N}^{\text{tr}}(1)$ becomes singular. The map is well defined and analytic for phase-space points to the right of this curve. Points on the curve are sent to infinity. The possible action of the map on points to the left of the curve is unknown. . . . .	2331
33.4.3	(Place Holder) Curves of constant $\Lambda/\lambda$ and flow directions for the equations of motion (4.44) and (4.45). These curves were made with $\lambda = 1$ , which simply sets the scale for $q$ and $p$ , and $\Lambda = 0, \pm 5$ . . . . .	2333
33.4.4	(Place Holder) Curve on which the map $\mathcal{N}^{\text{tr}}(1)$ becomes singular. The map is well defined and analytic for phase-space points to the right of this curve. Points on the curve are sent to infinity. The possible action of the map on points to the left of the curve is unknown. . . . .	2336
35.1.1	Phase-space portrait, in the case $\theta/2\pi = 0.22$ , resulting from applying the map $\mathcal{M}$ repeatedly (2000 times) to the seven initial conditions $(q, p) = (.01, 0), (.1, 0), (.15, 0), (.2, 0), (.25, 0), (.3, 0)$ , and $(.35, 0)$ to find their orbits. . . . .	2367

35.1.2	Phase-space portrait, in the case $\theta/2\pi = 0.22$ , resulting from applying the map $\mathcal{M}^{\text{tr}}$ repeatedly (2000 times) to the two initial conditions $(q, p) = (.01, 0)$ and $(.4, 0)$ to find their orbits. The orbits appear to spiral into the origin. . . . .	2368
35.1.3	Phase-space portrait, in the case $\theta/2\pi = 0.22$ , resulting from applying the map $\mathcal{M}^{\text{tr}3}$ repeatedly (2000 times) to the four initial conditions $(q, p) = (.01, 0)$ , $(.075, 0)$ , $(.1, 0)$ , and $(.125, 0)$ to find their orbits. The orbits appear to move away from origin. . . . .	2370
35.3.1	Phase-space portrait, in the case $\theta/2\pi = 0.22$ , resulting from applying the map $\mathcal{M}^{\text{sc}}$ repeatedly (2000 times) to the four initial conditions $(q, p) = (.01, 0)$ , $(.1, 0)$ , $(.15, 0)$ , and $(.2, 0)$ to find their orbits. . . . .	2384
35.3.2	Phase-space portrait, in the case $\theta/2\pi = 0.22$ , resulting from applying the map $\mathcal{M}^{\text{isc}}$ repeatedly (2000 times) to the seven initial conditions $(q, p) = (.01, 0)$ , $(.1, 0)$ , $(.15, 0)$ , $(.2, 0)$ , $(.25, 0)$ , $(.3, 0)$ , and $(.35, 0)$ to find their orbits. . . . .	2386
35.3.3	Phase-space portrait, in the case $\theta/2\pi = 0.22$ , resulting from applying the map $\mathcal{M}^{\text{psc}}$ repeatedly (2000 times) to the to the seven initial conditions $(q, p) = (.01, 0)$ , $(.1, 0)$ , $(.15, 0)$ , $(.2, 0)$ , $(.25, 0)$ , $(.3, 0)$ , and $(.35, 0)$ to find their orbits. . . . .	2388
35.3.4	Phase-space portrait, in the case $\theta/2\pi = 0.22$ , resulting from applying the map $\mathcal{M}^{\text{ipsc}}$ repeatedly (2000 times) to the seven initial conditions $(q, p) = (.01, 0)$ , $(.1, 0)$ , $(.15, 0)$ , $(.2, 0)$ , $(.25, 0)$ , $(.3, 0)$ , and $(.35, 0)$ to find their orbits. . . . .	2389
37.1.1	Actions of a map $\mathcal{M}$ and its reversed counterpart $\mathcal{M}^r$ . . . . .	2410
37.5.1	Schematic drawing of a ring showing the locations (Poincaré surfaces of section) $0; 1, \tilde{1}; 2, \tilde{2}; 3, \tilde{3}$ ; etc. . . . .	2429
37.7.1	The dynamic aperture of the Hénon map for the case $\phi/(2\pi) = 0.22$ . . .	2437
39.2.1	Two of many possible orderings for the terms in a double series. . . . .	2455
39.2.2	Possible Reinhardt diagram for the case of two complex variables. The complete Reinhardt set consists of those points $z = (z_1, z_2)$ for which the pairs $ z_1 $ , $ z_2 $ lie in the shaded area, or the darkened portions of the axes representing possible thorns. The quantities $R_1$ , $R_2$ on the boundary of the shaded area are conjugate radii. . . . .	2456
39.2.3	The logarithmic image of the shaded area in Figure 2.2. This image is convex if any two points $P, Q$ in the image can be joined by a straight line that is also in the image. . . . .	2457
39.2.4	Determining the conjugate radii by fixing $R_1$ and searching for the closest singularity in $z_2$ as $\phi_1$ varies to yield $R_2$ . . . . .	2459
39.2.5	Determining the conjugate radii by fixing $R_2$ and searching for the closest singularity in $z_1$ as $\phi_2$ varies to yield $R_1$ . . . . .	2459
39.2.6	A point charge located at unit distance from the origin along the $x_2$ axis.	2460
39.2.7	The Reinhardt diagram for the series (2.24), which represents the function $f(z)$ given by (2.25), is a cone. . . . .	2461



39.2.8	Reinhardt diagrams, for three values of $x_3$ , of the series (2.30) that represents $f(z; x_3)$ . Diagrams for negative values of $x_3$ are not shown since the diagrams for $\pm x_3$ are identical. . . . .	2462
39.2.9	Analytic continuation along a path out of a domain $\mathcal{D}$ in the complex $w$ plane by making successive related Taylor expansions in overlapping disks along the path. . . . .	2464
39.2.10	Reinhardt diagram for a complete Reinhardt domain that is not logarithmically convex. The dashed <i>curved</i> line segment is the inverse image of the dashed <i>straight</i> line segment in Figure 2.11. The domain becomes logarithmically convex if the region corresponding to the area below the dashed line is annexed to that corresponding to the shaded area. . . . .	2464
39.2.11	The logarithmic image of the shaded region of Figure 2.10. Augmenting the image by adding the area below the dashed <i>straight</i> line segment makes the image convex. . . . .	2465
39.3.1	Real $x_1, x_2$ convergence sets for the homogeneous polynomial series (3.51) for various values of $x_3$ . Together they form a hyperbola of revolution. Sets are not shown for negative values of $x_3$ since the sets for $\pm x_3$ are identical. . . . .	2473
40.2.1	Sample extraction of a two-column array from a three-column array. . .	2495
40.2.2	Path to the exponent $j = (1, 0, 2)$ down the modified glex sequence in 3 variables. . . . .	2496
J.1.1	The curves $y = f(a, b; x)$ for $b = 11.5$ and various values of $a \in [-5, 0]$ . Also shown is the line $y = x$ . Intersections of the line and the curve correspond to fixed points. . . . .	2640
J.1.2	Bifurcation diagram showing $x_\infty$ as a function of $a$ for the map (1.1) with $b = 11.5$ and $a \in [-5, 5]$ . For $a = -5$ , there is only one fixed point, and it is stable. As $a$ is increased from this value, a blue-sky bifurcation occurs at $x_\infty \simeq +1$ when $a \simeq -4.8$ . Here a pair of fixed points, one stable and one unstable, is born. Now there are three fixed points. The one that bifurcates to larger values of $x_\infty$ is stable, and the one that bifurcates to smaller values of $x_\infty$ is unstable. The original fixed point persists, and remains stable. At $x_\infty \simeq +1$ and $a \simeq +4.8$ a blue-sky merger occurs where two fixed points, one stable and the other unstable, annihilate. For $a$ values larger than this there is only one fixed point. In between the values $a \simeq -4.8$ and $a \simeq +4.8$ there are two incomplete period-doubling cascades. . . . .	2641



J.3.1	A portion of the Feigenbaum diagram for the map (1.1) with $b = 11.7$ . Also shown are the paths of all period-one fixed points, both stable and unstable. The full diagram is similar to that of Figure 1.2 except that both period-doubling cascades now run to completion. Specifically, for the upper cascade shown here, a blue-sky bifurcation again occurs and, as $a$ is further increased, the stable fixed point begins a Feigenbaum perioding doubling cascade that now runs to completion followed by a region of chaos. But then, as $a$ is increased still further, the cascades undoes itself until there is again only a single stable fixed point. The behavior for the lower cascade is analogous. . . . .	2643
S.2.1	A grid of points representing the set $\Gamma_3^4$ . For future reference a subset of $\Gamma_3^4$ , called a <i>box</i> , is shown in blue. . . . .	2721
T.2.1	Sampling points for $*C^2:5-1$ . . . . .	2774
T.2.2	Sampling points for $*C^2:5-2$ . . . . .	2774
W.2.1	The function $\psi^\delta(x, y)$ as a function of $x$ for various values of $y$ . . . . .	2821
W.2.2	The function $\psi^\delta(x, y)$ as a function of $y$ for various values of $x$ . . . . .	2821
W.3.1	The function $\psi^\delta(x, y, z) = \psi^\delta(\rho, z)$ as a function of $\rho$ for various values of $z$ . . . . .	2826
W.3.2	The function $\psi^\delta(x, y, z) = \psi^\delta(\rho, z)$ as a function of $z$ for various values of $\rho$ . . . . .	2826
W.4.1	(Place Holder) The function $\hat{\psi}^\delta(\lambda, \theta)$ as a function of $\theta$ for various values of $\lambda$ . . . . .	2831
W.5.1	The function $\eta(\tau)$ . It appears to be monotonically increasing. . . . .	2836
W.5.2	(Place Holder) The kernel $K(m, k; \rho, R)$ as function of $m$ and $k$ for the case $\rho = 2$ cm and $R = 2.5$ cm. The quantity $k$ has units of inverse centimeters. . . . .	2837
W.5.3	(Place Holder) The function $\psi^\delta(\rho, \phi, z)$ as a function of $\phi$ and $z$ when $\rho = 2$ cm and $R = 2.5$ cm. . . . .	2838
W.5.4	(Place Holder) The function $\psi^\delta(\rho, \phi, z)$ as a function of $\phi$ and $z$ when $\rho = 1$ cm and $R = 2.5$ cm. . . . .	2838
W.5.5	(Place Holder) The function $\psi^\delta(1, 0, z)$ as a function of $z$ when $R = 2.5$ cm. . . . .	2839
W.6.1	(Place Holder) The function $\psi^\delta(u, v)$ as a function of $v$ for various values of $u$ when $U = 0.5$ and therefore $\tanh(U) = 0.46 \cdots$ . . . . .	2844
X.1.1	Optical system consisting of an optical device preceded and followed by simple transit. A ray originates at $P^i$ with <i>initial</i> location $\mathbf{r}^i$ and <i>initial</i> direction $\hat{\mathbf{s}}^i$ , and terminates at $P^f$ with <i>final</i> location $\mathbf{r}^f$ and <i>final</i> direction $\hat{\mathbf{s}}^f$ . . . . .	2852
X.8.1	Schematic layout of doublet imaging system that is free of all third-order aberrations and four fifth-order aberrations. The object plane is on the left and the image plane is on the right. . . . .	2894

X.8.2	Less schematic layout of imaging doublet system that is free of all third-order aberrations and four fifth-order aberrations. The object plane is on the far left and the image plane is on the far right (so that both are not visible), and only the shapes of the various lens surfaces and the lens thicknesses and spacings are illustrated. The <i>reference plane</i> $RP_1$ is at the beginning of the convex lens, and $RP_2$ is at the end of the concave lens. In the thin-lens approximation the convex and concave lenses have powers of $1/f = 10 \times 10^{-2}$ and $1/f = -10 \times 10^{-2}$ , respectively. . . . .	2896
X.10.1	Lie Algebraically Designed Magnetic Optical System for Fast Dynamic (Nanosecond) Imaging of Dense Objects Using High-Energy Proton Beams.	2912
X.10.2	Ray Trace of Soft-Edge Lie Algebraically Designed Super Lens for 50 GeV protons. . . . .	2913
Y.5.1	The gravestone of Max and Hedwig Born. . . . .	2924

# List of Tables

2.3.1	Minimum Number of Stages $s$ Required for Explicit Runge Kutta to Achieve Order $m$ . . . . .	185
2.4.1	Expansion Coefficients for $F$ and $G$ . . . . .	212
2.4.2	The Adams' Corrector Coefficients $\tilde{a}_l^N$ . . . . .	216
2.4.3	The Adams' Predictor Coefficients $\tilde{b}_k^N$ . . . . .	216
3.7.1	Dimension of $sp(2n)$ . . . . .	341
3.7.2	Cartan Catalog of the Classical and Exceptional Lie Groups/Algebras. . . . .	347
4.1.1	$N = 6$ ; scaling $n$ values chosen to make $  z/(2^n)   < (1/10)$ . . . . .	441
4.1.2	$N = 9$ ; scaling $n$ values chosen to make $  z/(2^n)   < (1/10)$ . . . . .	443
5.8.1	Structure Constants of $su(3)$ . . . . .	559
5.8.2	Symmetric Coupling Coefficients of $su(3)$ . . . . .	559
5.8.3	Dimensions of Representations of $su(3)$ . . . . .	565
5.8.4	Some Structure Constants of $sp(6)$ . . . . .	577
5.8.5	Remaining Structure Constants of $sp(6)$ . . . . .	578
6.7.1	Darboux Matrices $\alpha$ for the Generating Function types $F_1$ through $F_4$ and $F_+$ . . . . .	747
7.3.1	Number of monomials of degree $m$ in various numbers of variables. . . . .	837
7.10.1	Number of monomials of degree 1 through $m$ in various numbers of variables. . . . .	868
7.10.2	Storage Requirements for Taylor and Lie Maps. . . . .	869
8.9.1	Values of $\dim(L_2/L_D)$ . . . . .	928
8.9.2	Values of $\dim({}^\epsilon L^0/{}^\epsilon L^\ell)$ . . . . .	936
9.4.1	Order in which the $\tilde{h}_\ell^m$ are to be extracted for the case $L^0/L^3$ . . . . .	978
9.4.2	Order in which the $\tilde{h}_\ell^m$ are to be extracted for the case $L^0/L^7$ . . . . .	979
10.12.1	A labeling scheme for monomials through degree three in two variables. . . . .	1045
10.12.2	Nonzero values of $C_{br'r''}^r$ for $r \in [1, 5]$ in the two-variable case. . . . .	1052
10.12.3	A labeling scheme for monomials through degree three in three variables. . . . .	1055
10.12.4	Nonzero values of $C_{br'r''}^r$ for $r \in [1, 9]$ in the three-variable case. . . . .	1059

16.2.1	Numerical behavior of $f(84)$ for small values of $a$ . . . . .	1417
16.2.2	Numerical behavior of $M_{21}^{\text{LFF}}$ for small values of $a$ . . . . .	1426
16.2.3	Numerical behavior of $f^{\text{LFF}}(84)$ for small values of $a$ . . . . .	1430
16.2.4	Numerical behavior of $c_1^{\text{LFF}}(a)$ for small values of $a$ . . . . .	1444
17.4.1	The quantity $q_{\text{cr}}(n)$ for various values of $n$ . . . . .	1560
19.1.1	The exact and discrete (with $N = 49$ ) Fourier coefficients of $f(\phi)$ . . . .	1675
19.2.1	The coefficients $B_m^7(q)$ . . . . .	1712
21.3.1	Relative difference between the surface-data-based map and the exact map.	1782
21.3.2	Relative error of the noisy surface data based map compared to the exact map. . . . .	1784
27.5.1	Dimensions of Representations of $sp(4)$ . . . . .	1895
27.8.1	Dimensions of Representations of $sp(6)$ . . . . .	1915
40.2.1	Modified glex sequencing, a possible glex related indexing scheme for monomials in 6 variables. . . . .	2485
40.2.2	A possible grevlex related indexing scheme for monomials in 6 variables.	2486
40.2.3	Lowest and highest indices for monomials of degree $ideg$ in 6 variables.	2487
40.2.4	Modified glex sequence for $j$ in 3 variables. . . . .	2494
40.5.1	Modified glex sequence when $m = 4$ and $d = 2$ . . . . .	2501
40.5.2	Multiplication table (when $m = 4$ and $d = 2$ ) giving values of $ih$ . . . .	2502
40.5.3	Multiplication look-up table size for polynomials of degree 1 through $m$ in various numbers of variables. . . . .	2503
40.5.4	Multiplication look-up table size for polynomials of degree 1 through $m$ in various numbers of variables when symmetry is not exploited. . . .	2504
40.6.1	Contents of the arrays $iftbl$ , $igtbl$ , and $ihl$ in the case $m = 4$ and $d = 2$ .	2510
40.6.2	Contents of the array $icmin$ in the case $m = 4$ and $d = 2$ . . . . .	2511
40.7.1	The result of rearranging Table 6.1 in order of increasing $ih$ . . . . .	2515
40.7.2	The arrays $icbot$ and $ictop$ in the case $m = 4$ and $d = 2$ . . . . .	2516
40.7.3	The arrays $i1(i)$ and $i2(i)$ in the case $m = 3$ and $d = 6$ . . . . .	2521
40.8.1	Array sizes $maxic1$ and $maxic2$ (in the case of 6 phase-space variables) for various values of $maxdeg$ . . . . .	2527
S.2.1	A labeling scheme for monomials in three variables. . . . .	2720
S.2.2	The vectors in $B_{28} = \{\mathbf{j}   \mathbf{j} \leq (1, 2, 1)\}$ . . . . .	2727
S.2.3	The vectors $\mathbf{j}$ and $\mathbf{i} = (\mathbf{k} - \mathbf{j})$ for $\mathbf{j} \in B_{28}$ and $k_a = \Gamma_{28,a}$ . . . . .	2728
S.2.4	A labeling scheme for monomials in two variables. . . . .	2734
S.2.5	A labeling scheme for monomials in one variable. . . . .	2737
T.1.1	Maximum Order $\ell_{\text{max}}$ for $k$ Newton-Cotes Sampling Points. . . . .	2762
T.2.1	$S_0(2, d)$ as a Function of $d$ . . . . .	2772
U.2.1	$N(n, 3)$ , $S_0(n, 3)$ , $3N(n, 3)$ , $3S_0(n, 3)$ , and $S_B(n)$ as functions of $n$ . . . .	2784
U.3.1	Allowed values of $n\ell J$ . . . . .	2788

---

X.3.1	Some Values of $N(n, j)$ . . . . .	2874
X.4.1	Some values of $C(221; m, m', m + m')$ and $C(223; m, m', m + m')$ . . . .	2882
X.4.2	Remaining values of $C(221; m, m', m + m')$ and $C(223; m, m', m + m')$ .	2883



# Preface

John Wallis (1616-1703), Savilian Professor of Geometry at Oxford, was a mathematician and predecessor of Isaac Newton. His most important book, published in 1656, was *Arithmetica Infinitorum*. It introduced, among others, the concepts of negative and fractional exponents, and considered the problem of finding the areas under curves described by functions involving such exponents. He also introduced the symbol  $\infty$ . In 1685 he published *Algebra*.

His contemporary Thomas Hobbes (1588-1679), a philosopher and political theorist, read (or perhaps only paged through) this 1656 book, and described it as a “a scab of symbols as if a hen had been scraping there.” Apparently taken by this simile, on another occasion he wrote of Wallis: “And for (your book) on *Conic Sections*, it is covered over with a scab of symbols that I had not the patience to examine whether it be well or ill demonstrated.” He goes on to say: “Symbols, though they shorten the writing, yet do not make the reader understand it sooner than if it were written in words. . . . (with the use of symbols) there is a double labour of the mind, one to reduce your symbols to words, which are also symbols, another to attend to the ideas which they signify.”

But, according to Leibniz (1646-1716), “In symbols one observes an advantage in discovery which is greatest when they express the exact nature of a thing briefly and, as it were, picture it; then indeed the labor of thought is wonderfully diminished.”<sup>1</sup> Laplace (1749-1827) was even more enthusiastic when he wrote “Such is the advantage of a well-constructed language that its simplified notation often becomes the source of profound theories.” And, according to Whitehead (1861-1947), “Civilization advances by extending the number of

---

<sup>1</sup>Leibniz invented much of modern calculus notation. He also introduced the term *dynamick* for what Newton (1642-1727) had previously called *rational mechanics*. But Newton objected to this name, not because of its “inadequacy to describe the subject matter”, but rather because Leibniz had “set his mark upon the whole science of forces calling it Dynamick, as if he had invented it himself & is frequently setting his mark upon things by new names & new Notations”. Leibniz was kinder to Newton when he wrote “Taking mathematics from the beginning of the world to the time of Newton, what he has done is much the better half.” For a history of how Leibnizian notation came to be used in Great Britain, see the Web site [https://en.wikipedia.org/wiki/Analytical\\_Society](https://en.wikipedia.org/wiki/Analytical_Society).

To Descartes (1596-1650) we owe the use of the symbols  $a, b, c \dots$  as constants, the symbols  $x, y, z \dots$  as variables, writing  $xx$  as  $x^2$  etc., and, of course, honor for forging the connection between algebra and geometry (to create analytic geometry) by the use of Cartesian coordinates including making graphs of functions. To add to the list: Robert Recorde in 1540 introduced the  $+$  and  $-$  symbols for addition and subtraction and in 1557 introduced the equal sign  $=$ , William Oughtred in 1631 introduced the multiplication sign  $\times$  and the trigonometric function symbols  $\sin$  and  $\cos$ , Johann Rahn in 1659 introduced the division sign  $\div$  and the therefore sign  $\therefore$ , and William Jones in 1706 introduced use of the Greek letter  $\pi$  to denote the value that is the ratio of the circumference to the diameter for any circle and use of a dot above a letter to denote differentiation with respect to time.



important operations which we can perform without thinking of them.”

The purpose of this book is to explore and illustrate how Lie-algebraic/map methods and Lie-algebraic concepts/symbols are broadly applicable to many areas of Nonlinear Dynamics including Accelerator Physics.

## Reference

J. Mazur, *Enlightening symbols: a short history of mathematical notation and its hidden power*, Princeton University Press (2014).

# Acknowledgments

Institutions: U.S. Department of Energy, University of California (Berkeley), Institute for Advanced Study, University of Maryland, Institut des Hautes Études Scientifiques (IHÉS, France), Institute for Theoretical Physics Santa Barbara, Los Alamos National Laboratory, SSC Central (Berkeley) Design Group, Lawrence Berkeley National Laboratory, Stanford Linear Accelerator Center.

Minds: New ideas often emerge through close interaction between minds. Accordingly, these ideas do not solely belong to any of these individual minds, but rather are the fruit of their mutual interaction - an emergent property of exchange and interaction. Many of these minds are from the past and are known only through their writings or influences passed down through our ancestors. They are too numerous to mention here, but some will be acknowledged in the text, and more will be referenced in the Bibliography. Others are those of our contemporaries or near contemporaries. They include John Horvath, Richard K. Cooper, Robert Gluckstern, David Sutter, Eyvind Wichmann, David Judd, Robert Karplus, Alex Dessler, J. David Jackson, V. Bargmann, Louis Michel, Maury Tigner, Karl L. Brown, Alex Chao, John Irwin, Miguel Furman, Leo Michelotti, Martin Berz, Klaus Halbach, K. B. Wolf, Desmond Barber, Dobrin Kaltchev, Sateesh Mane, Peter Walstrom, Paul Channell, C. Thomas Mottershead, Filippo Neri, John Finn, David Douglas, Étienne Forest, Liam Healy, Robert Ryne, Govindan Rangarajan, Dan Abell, Marco Venturini, Chad Mitchell.

I was like a boy playing on the sea-shore, and diverting myself now and then finding a smoother pebble or a prettier shell than ordinary, whilst the great ocean of truth lay all undiscovered before me.

Isaac Newton

For in Him we live and move and have our being.

Acts 17:28

Assertion made by Saint Paul about the “unknown god” and attributed by Paul to an unnamed Greek poet, now thought to be Epimenides of Knossos because this line appears

in his poem *Cretica*.

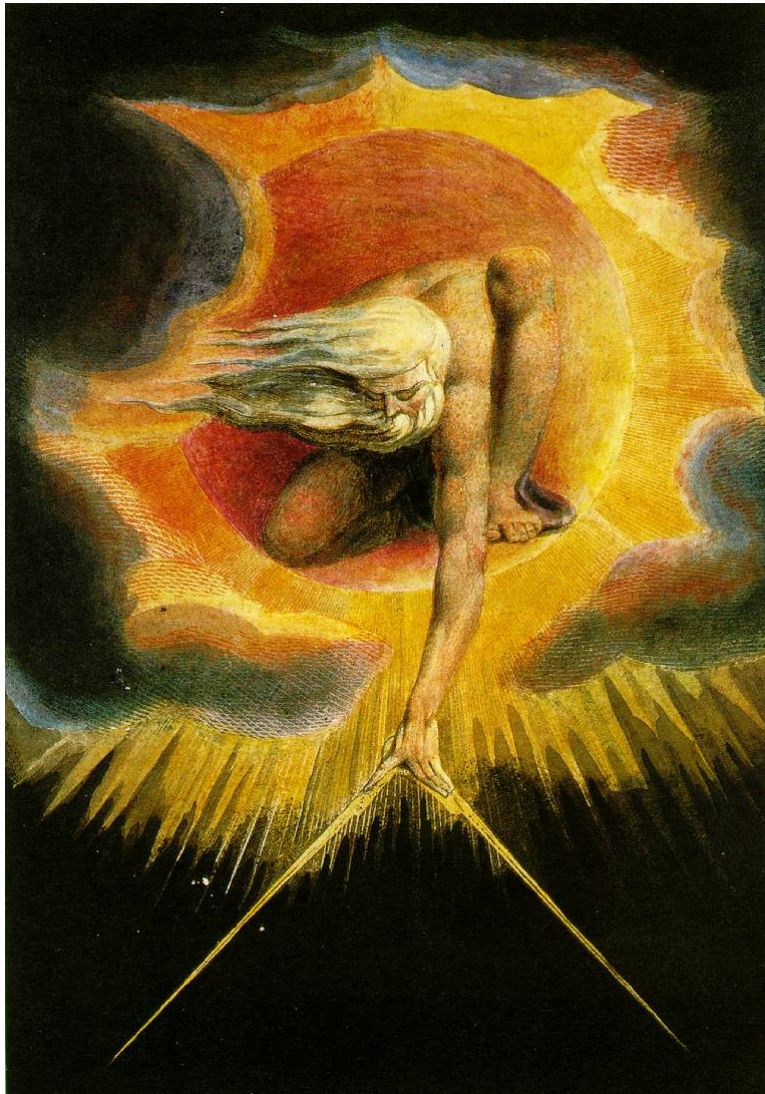


Figure 0.0.1: The Ancient of Days. “If the doors of perception were cleansed, everything would appear to man as it is: Infinite.” William Blake (1757-1827)